Development of Nanostructured Anode Materials for High-Performance Sodium Ion Batteries

高性能ナトリウムイオン電池のためのナノ構造を有するアノード材料の開発

Graduate School of Life Science

and System Engineering

Kyushu Institute of Technology

Dissertation for the Degree of Doctor of Engineering

Author: HUAN LI

Supervisor: Professor Tingli Ma

Aug. 2018

Abstract

Sodium ion battery has been regarded as a promising alternative for commercial lithium ion battery due to the abundance of sodium resource and its safety. In order to achieve a power density as high as lithium ion batteries, it is crucial to develop appropriate electrode materials for sodium ion batteries. In this thesis, we synthesized four different kinds of nanostructured anode materials with low cost and relatively high specific capacity via facile methods. Furthermore, these four materials were applied as anode for sodium ion batteries. Moreover, the intrinsic connection between the material characteristic and their electrochemical properties were also studied.

In Chapter 1, the background and research status of sodium ion batteries was introduced. In addition, the issues for the current research of sodium ion batteries and the objectives of this work have been clarified. In general, hard carbon material is the most widely studied anode material in sodium ion batteries with a relatively high theoretical specific capacity. However, the undesirable electrode stability, as well as the poor safety, restricted its application. Therefore, it is of great importance to developing novel anode materials with high power density, low cost and high safety. In a comparison of conventional anode materials, nanostructured materials have already been proved to possess better electrochemical properties due to their good electrochemical reactivity and shorter charge transmission paths.

In Chapter 2, the reagents and apparatus used in this work have been listed. Furthermore, the preparation and assembling process of devices were displayed in this chapter. In addition, the physical characterization and electrochemical measurements for the as-prepared materials have been introduced, including SEM measurement, XRD measurement, cycling performance measurement, cyclic voltammetry and so on.

In Chapter 3, porous TiO_2 nanopills were prepared by using Ti-based metal-organic framework as a precursor and template via a simple two-step method. Furthermore, the porous TiO_2 nanopills were employed as anode materials for sodium ion batteries and delivered relatively high specific capacity as well as excellent electrode stability. The excellent electrochemical performance of the TiO_2 nanopills electrode may benefit from the porous structure, which could

promote the diffusion of sodium ions and electrolyte, as well as shorten transmission distance attributed to the nanostructured particles.

In Chapter 4, feather-like MnO_2 nanostructure was in-situ grown on carbon paper by a facile hydrothermal method. Furthermore, the growth mechanism of the unique feather-like nanostructure was analyzed and proposed by studying the intermediate during the hydrothermal process. When applied as a binder-free anode for sodium ion batteries, excellent electrochemical performance could be achieved. The obtained high capacity, as well as excellent cycling stability, could be attributed to the open tunnel structure of MnO_2 as well as the feather-like nanostructure, which contributed to the reversible insertion and storage of sodium ions.

In Chapter 5, to improve the electrochemical performance of Ti_3C_2 (MXene), we composited black phosphorous nanoparticles with exfoliated Ti_3C_2 via a multi-step method. When used as anode materials for sodium ion batteries, the black phosphorous/Ti_3C_2 nanocomposites exhibited higher specific capacity and better electrode stability than black phosphorous electrode and the Ti_3C_2 electrode. The improved performance for this composite could be due to the high theoretical specific capacity and 2D structure of black phosphorous, which promoted the insertion of sodium ions. The black phosphate（BP）nanoparticles also contributed to the increased active sites and specific surface area, and further promoted the storage capability of electrolyte and electrons.

In Chapter 6, based on the research of the as-prepared MXene material in Chapter 5, we attempted to prepare a novel Nb, Mo-based double transition metal carbide by a low-temperature method. The relationship between the reaction time, molar ratio of raw materials and the phase and morphology of obtained products was investigated and analyzed in detail. Finally, the optimal synthesis condition was summarized, and a $MoNb_2SnC_2$ MAX material was obtained. Furthermore, this material was initially investigated as anode material for sodium ion batteries and exhibited good reversibility and cycling stability.

In this work, the as-prepared four kinds of materials exhibited good electrochemical performance, attributing to the open tunnel crystal structure and high specific surface area. In addition, these investigations are also useful for the development of novel electrode materials for practical sodium ion batteries.

Table of Contents

Chapter 1 Introduction

1.1 Background

With the rapid development of human society and ecology, the demand for energy keeps growing as well. The currently used energy are mainly coal, petroleum, natural gas and other traditional non-renewable fossil fuels, which are almost exhausted. What's worse, using fossil fuels would produce large amounts of greenhouse gases and waste gas emissions such as carbon dioxide, sulfur dioxide, and nitrogen oxide, leading to the greenhouse effect and serious environmental pollution. Thus, developing and utilizing clean and renewable energy resources have become one of the most urgent issues of the modern society.

The commonly called renewable energy mainly contains solar energy, wind power, geothermal power, tidal energy, bio-energy, etc. However, the low power density and immature conversion technical conditions severely limited the development and utilization of these green energy sources. On this basis, energy storage systems (ESSs), a kind of clean recycled energy source, have become more and more imperative. To date, various ESSs have been researched and developed, such as lead-acid batteries, rechargeable batteries, etc. Among them, lithium ion batteries have been considered to be ideal energy storage systems and have been widely applied to electronic products, medical devices, aerospace, military and other fields due to its relatively high power density. However, the continually increasing demand for lithium source leads to a sharp decrease of lithium storage in the crust, resulting in the increase in cost. [1] To meet this bottleneck, it is of great importance to developing a chemical power system with lower cost, safety and long cycle life.

Sodium, as the 6^{th} abundant element, is widely distributed in the crust. Meanwhile, since sodium belongs to the same group as the lithium element in the periodic table and possesses similar physicochemical properties, it has great potential to develop a sodium ion battery using sodium source. Compared with the lithium ion battery system, the sodium ion battery has two advantages as follows: Firstly, the raw materials are more abundant and easier to acquire, thus

the production costs are greatly reduced; Secondly, the redox balance potential of sodium is 0.3V, higher than lithium, thus an electrolyte solution with lower decomposition potential can be applied in the sodium ion battery, leading to relatively higher security of the sodium ion battery system. [2,3] Attributed to such advantages, more and more companies have already begun to study the practical applications of the sodium ion batteries. It was reported that in 2012 Toyota developed a kind of low-price sodium ion battery using sodium-based compounds as cathodes, which achieved a voltage 30% higher than the commercial lithium ion batteries, and further improved the recharge mileage to maximum 1000 mileages (620 miles).

Nevertheless, compared to the lithium ion (0.76 Å), the larger radius of the sodium ion (1.02 Å) hinders the insertion/desertion process of the sodium ions, and leads to a poor charge/discharge reversibility and a low specific capacity, thus it restricts the further practical applications of the sodium ion batteries. [4,5] In order to solve these problems, researchers have carried out a great many explorations and already gain some achievements. Early in the the 1970s, Whittingham's group [6] and Hagenmuller's group [7] investigated the sodium ion battery system and found layer structure compounds such as MoS_2, TiS_2, TaS_2 and Na_xMO_2 (M = Mn, Co, etc.) could permit the insertion and desertion of the sodium ions.

1.2 Structure of a sodium ion battery

A sodium ion battery consists of the cathode, the anode, the filter, the electrolyte and the electrode shell, which is the same as the structure of a lithium ion battery. Meanwhile, the electrode is composed of the active material, the conducting materials, the binder and the collector. The collector of the cathode is generally aluminum foil, while the collector of the anode is usually cobalt or aluminum foil. In common, the electrolyte solution of the sodium ion battery is sodium hexafluorophosphate ($NaPF_6$) or sodium perchlorate ($NaClO_4$) dissolved in organic solvents such as propylene carbonate (PC), ethylene carbonate (EC), diethyl carbonate (DEC) or their mixture. Different from the lithium ion battery, a glass fiber membrane is used as the filter for the sodium ion battery.

1.3 Working principle of a sodium ion battery

Similar to the working principle of a lithium ion battery, the charge/discharge process is actually an insertion/desertion process of the sodium ions. In addition, during the charging and

discharging process, the sodium ions insert and desert back and forth between the positive and negative electrode, thus this kind of battery is vividly called the “rocking chair battery”.

For example, when employing the layer structure $NaMnO_2$ as the cathode and Na_xC_6 as the anode to assemble a rechargeable sodium ion battery, the working principle could be explained as depicted in Figure 1-1. During the charging process, sodium ions deserted from the lattice of the cathode material and then inserted into the lattice of the anode material through the electrolyte solution. At this moment, the cathode is in the state of sodium ion depletion, while the anode is in the state of sodium ion enrichment. Meanwhile, the same number of electrons with sodium ions are transferred to the anode electrode to maintain the charge balance. The discharging process is exactly the opposite of the charging process. During the discharging process, sodium ions deserted from the lattice of the anode material and then inserted into the lattice of the cathode material through the electrolyte solution. At this time, the cathode is in the state of sodium ion enrichment.

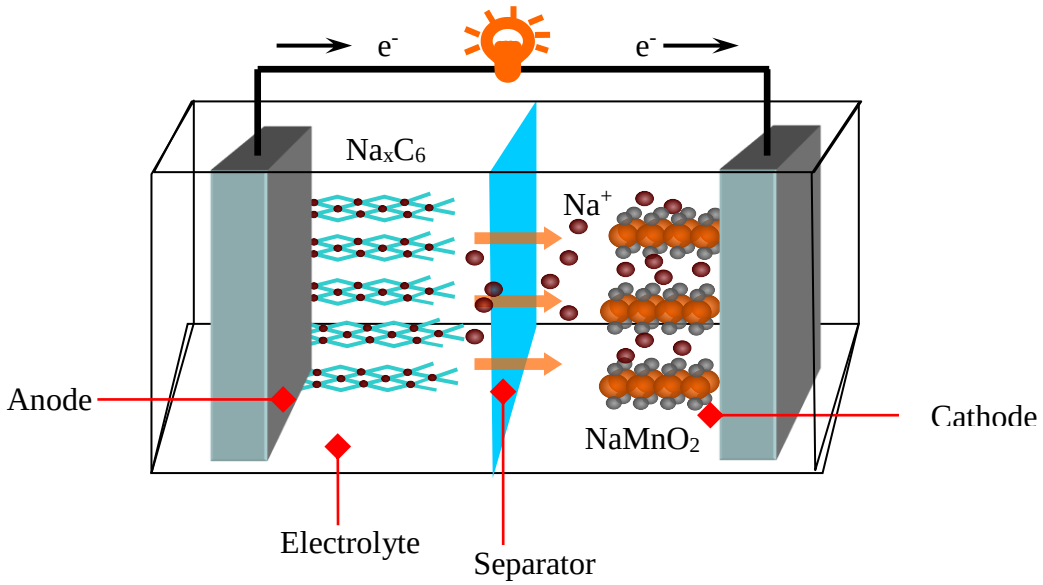

Figure 1-1 Schematic illustration of a typical rechargeable sodium battery.

1.4 Electrode materials of sodium ion batteries

1.4.1 Cathode materials of sodium ion batteries

1.4.1.1 Layered Na_xMO_2 compound

Layered Na_xMO_2 (M = Cr, Fe, Co, Ni, Mn, V, etc.) compound with relatively high insertion potential and power density is a kind of widely used cathode material for sodium ion batteries. In the 1980s, the sodium storage behavior of four Na_xCoO_2 with different crystal phases (O3, O'3, P3 and P2 phases) were studied by Delmas et al. [8] It was found that the sodium ion insertion/desertion in these four phases were all reversible while the P2 phase could achieve longer cycling life and better Columbic efficiency. Therefore, deeply investigations about P2 type Na_xCoO_2 have been carried out by different researchers. For instance, $Na_{0.74}CoO_2$ prepared by solid state method could deliver a specific capacity of 107 mAh g^{-1} with a Columbic efficiency of ~89% under a current rate of 0.1C at a voltage range of 2.0-3.8 V. [9] However, despite of the good electrochemical properties of Na_xCoO_2, the high price of the cobalt salts leads to an increased cost of batteries, which limited the further commercial development. Thus, other replaceable layer structure materials have been investigated about their insertion/desertion properties of the sodium ions. In recent years, Na_xMnO_2 ($x\leq1$) has been regarded as a promising cathode material for sodium ion batteries because of the abundance of the manganese and its low cost. α-$NaMnO_2$ (space group: C2/m) and β-$NaMnO_2$ (space group: Pmnm) are two common phases with high sodium contents. The earliest research about the Na^+ insertion/desertion capabilities of the O'3-type α-$NaMnO_2$ can be traced back to the 1980s. [7] As reported by Ma et al., the O'3-type $NaMnO_2$ could deliver a specific capacity of 197 mAh g^{-1} under a rate of C/30 at a voltage range of 2-3.8 V. [10] However, the specific capacity decayed quickly with the increasing cycling times, making it an unsuitable cathode material for sodium ion batteries. Billaud et al. firstly reported β-$NaMnO_2$ as a cathode material for sodium ion batteries, which possessed a different zigzag layer structure and exhibited a discharge capacity of 190 and 142 mAh g^{-1} at a current rate of C/20 and 2C, respectively. [11] Among various Na_xMnO_2 materials, $Na_{0.44}MnO_2$ owns a tunnel structure that permits the easy insertion of the sodium ions. $Na_{0.44}MnO_2$ obtained by heating Na_2CO_3 and Mn_2O_3 at 750 ^oC was firstly employed in sodium ion batteries and delivered a reversible capacity of 120 mAh g^{-1}. [12] In addition, $Na_{0.44}MnO_2$ nanowires synthesized by hydrothermal method also exhibited good cycling stability and rate

capability. [13] Although $Na_{0.44}MnO_2$ possess good electrochemical stability, the relatively low specific capacity and working potential limit its application in the non-aqueous sodium ion batteries.

In addition, the sodium-rich material Na_xTMO_2 (M =Ni, Mn, Fe and Co) is also a popular candidate as a cathode for sodium ion batteries because of their high specific capacity, high voltage and safety. [14,15] It is believed that the various composite structure of Na_xTMO_2 would be a new avenue for the development of high-performance layer structure cathode materials in the sodium ion batteries.

1.4.1.2 $NaMPO_4$ cathode materials with an olivine structure

$LiMPO_4$ (M=Fe, Co, Mn and Ni) is a common cathode material for lithium ion batteries. Among the M site metals, the most widely investigated is the $LiFePO_4$, which can deliver high specific capacity, good safety and long cycling life as the cathode material for lithium ion batteries. [16-18] Similarly, $NaFePO_4$ can be applied as the cathode material for sodium ion batteries. The $NaFePO_4$ mainly include olivine structure and maricite structure, while the maricite structure possesses a more thermodynamically stable structure. $NaFePO_4$ with the maricite structure has no migration channel for sodium ions, and thus cannot be directly used as a cathode material for sodium ion batteries. [19] Meanwhile, the $NaFePO_4$ with olivine structure has one-dimensional migration channel for the sodium ions, which leads to the reversibility of the insertion/desertion for sodium ions, thus is more suitable to be applied to sodium ion batteries.

To date, since it is difficult to be prepared by direct synthesis, most $NaFePO_4$ materials with olivine structure were prepared by inserting sodium ions into a $FePO_4$ precursor obtained via chemical or electrochemical methods. [20] By comparing the electrochemical performance of the $NaFePO_4$ in sodium ion batteries and the $LiFePO_4$ in lithium ion batteries, it is concluded that the reason for the limited electrochemical performance of the $NaFePO_4$ in sodium ion batteries is the low diffusion coefficient of the sodium ions and the high charge transfer resistance. [21] Moreau et al. prepared olivine $NaFePO_4$ by using $LiFePO_4$ as raw material, which is benefit beneficial for the sodium ion insertion in the olivine $FePO_4$. [22] With an average working potential of 3 V, the discharge specific capacity could reach about 139 mAh g^{-1}. In addition, the insertion/desertion mechanism for $NaFePO_4$ cathode material was investigated in detail. [23] In the charging process,

an intermediate phase of $Na_{0.7}FePO_4$ was firstly formed at 2.9 V through the solid solution process, and then an olivine $FePO_4$ phase was formed by a two-phase reaction. Thus, two voltage plateaus could be observed in the charge profile. Later in 2015, maricite $NaFePO_4$ cathode was studied again by Kim's group and achieved an initial specific capacity of 142 mAh g^{-1}, which is close to the theoretical specific capacity. [24] The capacity retention remained 95% after cycling for 200 times, and thus break the statement that maricite $NaFePO_4$ was not appropriate as a cathode material for sodium ion batteries. In addition, this investigation also provides a new direction for the research about $NaMPO_4$ cathode materials.

1.4.1.3 Pyrophosphates $Na_2MP_2O_7$ cathode materials

$Na_2MP_2O_7$ (M= Co, Fe and Mn) can be divided into various structures, such as monoclinic structure ($P4_2/mnm$), triclinic structure (P1) and tetragonal structure ($P2_1/c$). In a typical triclinic structure $Na_2MP_2O_7$, two MO_6 octahedral and PO_4 tetrahedron are connected by corner-sharing and edge-sharing, respectively, and then linked by interlaced connection with corner-sharing. Monoclinic structure $Na_2MP_2O_7$ belongs to a layer structure, in which MO_6 octahedral layer and P_2O_7 layer alternately arrange to form a monoclinic structure. Different from the above two structures, tetragonal structure $Na_2MP_2O_7$ belongs to a symmetrical structure that is composed by connecting each MO_4 tetrahedron with four P_2O_7 by corner-sharing. However, despite of the different crystal structure, all these three $Na_2MP_2O_7$ materials own a transport channel for sodium ions, and are able to permit the reversible insertion/desertion process of the sodium ions.

Among various pyrophosphates cathode materials, $Na_2FeP_2O_7$ materials possess the best electrochemical performance and thus have been relatively widely studied. Barpanda et al firstly investigated the Na^+ storage capability of the $Na_2FeP_2O_7$ by a solid state method and achieved a reversible specific capacity of 82 mAh g^{-1} with an average voltage of 3 V. [25] While investigating the thermal stability of this material after the sodium ion desertion process, it was found that the crystal phase changed from P1 to P21/C phase with no decomposition, illustrating the high thermal stability of $(P_2O_7)^{4-}$.[26] In the voltage range of 2.0-4.5 V, $Na_2FeP_2O_7$ cathode materials performed two kinds of reaction, including the single-phase reaction at ~2.5 V and a series two-phase reaction at 3.0-3.25 V. [27] In addition, the triclinic structure $Na_2MnP_2O_7$ can exhibit a discharge capacity of 90 mAh g^{-1} with an average voltage of 3.6 V, corresponding to the oxidation/reduction process of Mn^{3+}/Mn^{2+}. [28] For the $Na_2CoP_2O_7$ cathode material, an

average voltage of 3 V and a discharge capacity of 80 mAh g^{-1}, as well as an inclined charge-discharge profile, could be achieved. [29] Afterwards, they also prepared $Na_2(VO)P_2O_7$ with a tetragonal structure by a low-temperature solid-state method and further studied its sodium ion storage capability. This material delivered a reversible capacity of 80 mAh g^{-1}, and a voltage plateau at 3.8 V could be observed. [30]

From the investigations about the structure and electrochemical properties of the pyrophosphates, it can be concluded that the pyrophosphates prepared directly by high-temperature calcination own good electrochemical activity, especially for the Fe-based pyrophosphates. However, the large $(P_2O_7)^{4-}$ leads to a large molecular mass of the pyrophosphates, which results in a relatively low theoretical specific capacity. Thus, further research may focus on enhancing the capacity and the average potential of the pyrophosphates cathode materials.

1.4.1.4 NASICON-type $A_3M_2(PO_4)_3$ cathode materials

Na-superionic conductor (NASICON) possesses a three-dimensional (3D) framework structure. In a typical NASICON crystal structure, XO_4 tetrahedrons form frameworks with the MO_6 octahedron, while sodium ions are in the interspace of the framework, thus leading to a fast sodium ion mobility. NASICON-type $A_3M_2(PO_4)_3$ (A=Li, Na; M=V, Fe, Ti, Nb, etc.) with a 3D open transport tunnel and a high ion diffusion rate is a very fast ion conductor material. In fact, $Na_3Ti_2(PO_4)_3$ was initially employed as a solid electrolyte for sodium ion batteries by Hong's group early in the 1980s, which was considered to be unsuitable for practical applications due to its low conductivity. [31] In the lattice of $Na_3V_2(PO_4)_3$, sodium atoms exist both in the M1 site of the hexacoordinate and the M2 site of the octal-coordinate, while only the sodium in the M2 site can insert and desert reversibly and deliver a theoretical specific capacity of 117 mAh g^{-1}. By compositing $Na_3V_2(PO_4)_3$ with C and optimize the electrolyte, a higher average sodium ion storage potential than most reported cathode materials as well as a specific capacity of over 100 mAh g^{-1} could be obtained. [32] However, due to the toxicity of vanadium which may be harmful to the environment and human beings, future research about NASICON-type may be carried out towards the developing direction of other non-toxic and abundance transition metal NASICON structure cathode materials.

1.4.1.5 SO_4-based cathode materials

SO_4-based insertion materials have also been investigated as cathode materials for sodium ion batteries, while Fe-based sulfate exhibits the best electrochemical performance. Alluaudite-type $Na_2Fe_2(SO_4)_3$ reported by Barpanda delivered a reversible capacity of 102 mAh g^{-1} with an insertion potential of 3.8 V. [33] Even at a high current rate of 20C, the specific capacity could retain 55 mAh g^{-1}. They also investigated the sodium storage capability of Krohnkite-type $Na_2Fe_2(SO_4)_3 \cdot 2H_2O$, which exhibited a discharge capacity of about 75 mAh g^{-1} at C/20 rate as well as an average potential of 3.25 V. [34] In addition, from several reports about $Na_{2+2x}Fe_{2-x}(SO_4)_3$ it can be concluded that the $Na_{2.4}Fe_{1.8}(SO_4)_3$ (x=0.25) contains less impurity phase and exhibited excellent rate capability and electrochemical stability. [35,36] On this basis, similar cathode materials such as $Na_{2+2x}Mn_{2-x}(SO_4)_3$ and $Na_2Mg(SO_4)_3 \cdot 2H_2O$ were also studied. However, the obtained results were not ideal. [37,38]

To date, for the SO_4-based cathode materials, $Na_{2.4}Fe_{1.8}(SO_4)_3$ is considered to be the most promising one for applications, due to its high work potential, high capacity, low cost as well as its good environmental adaptability. Thus, further research may focus on how to prepare this material in large scale and to achieve better electrochemical performances.

1.4.1.6 Prussian blue $A_xMFe(CN)_6$ cathode materials

In a typical crystal structure of Prussian blue $A_xMFe(CN)_6$ (A= K, Na; M= Ni, Cu, Fe, Mn, Co, Zn, etc.), the alkali metal ions exist in the three-dimensional tunnel structure and coordination pores. This three-dimensional open tunnel structure can be beneficial for the transformation of storage of the sodium ions in the Prussian blue materials. In addition, according to the different M metal ions, various structures and Na^+ storage capabilities can be achieved. Therefore, a great many investigations about the Prussian blue $A_xMFe(CN)_6$ cathode material have been carried out in re/cent years.

Fe-based materials possess many advantages such as the sufficient reserves, the low cost and the structural stability. Thus, Fe^{2+} is employed as the M site element and the electrochemical performances of the $A_xFeFe(CN)_6$ have been investigated by many groups. For instance, $NaFeFe(CN)_6$ prepared via a rapid precipitation method was reported by Qian's group, which delivered an initial charge and discharge capacity of 95 and 113 mAh g^{-1}, respectively. [39]

Goodenough et al reported that $KFeFe(CN)_6$ cathode material could retain a reversible specific capacity of 100 mAh g^{-1} for 30 cycles. Afterward, they prepared $Na_{1.92}FeFe(CN)_6$ by hydrothermal method and obtained a high reversible discharge capacity of 155 mAh g^{-1}. [40] Even after cycling for 750 times, the capacity retention remained at 80%. Furthermore, when assembling full cells with hard carbon as anode materials, the full cells also exhibited good electrochemical performance.

Goodenough's group also investigated the sodium ion storage capabilities of a series $Na_xMnFe(CN)_6$ compounds. $Na_{1.72}MnFe(CN)_6$ displayed an average potential of 3.3 V and a rate capability at a high current rate of 40C. [41] In addition, they prepared $Na_2MnFe(CN)_6$ with a distorted crystal structure by removing the crystal water molecular in the crystal lattice. The as-prepared $Na_2MnFe(CN)_6$ exhibited a long voltage plateau at about 3.5 V and remained a capacity retention of 75% after 500 cycles. Yang et al prepared $Na_2MnFe(CN)_6$ with high crystallinity and low defect by controlling the crystallization process, which delivered a discharge capacity of 150 mAh g^{-1} with a capacity retention of 90% for 200 cycles. [42] Through doping Ni or PPy coating, the conductivity and electrochemical stability of Mn-based Prussian blue cathode materials could be further improved. [43,44]

Co-based Prussian blue cathode materials own relative high redox couple and reaction of two electrons. The $Na_{1.6}Co[Fe(CN)_6]_{0.9}\cdot 2.9H_2O$ film prepared by electrodeposition method exhibited two discharge voltage plateaus at 3.4 V and 3.8 V which could be assigned to the oxidation/reduction process of Co^{2+}/Co^{3+} and Fe^{2+}/Fe^{3+}, respectively. [45] This film could deliver a reversible capacity of 135 mAh g^{-1} and a rate capability at a high current rate of 60C.

In addition, Cu-based and Ni-based Prussian blue cathode materials can permit the insertion of only one sodium ion, but can display a better cycling stability. [46,47] The high voltage and reversibility of Prussian blue make it a promising cathode material for the practical application. However, issues such as easily formation of defects and thermal decomposition need to be solved firstly.

1.4.1.7 $NaMPO_4F$ (M=Fe, Co, Ni, Mn, V, etc.) cathode materials

$NaMPO_4F$ (M=Fe, Co, Ni, Mn, V, etc.) materials have also been studied as cathode materials for sodium ion batteries because of its high redox potential of a transition metal. Among various

reported $NaMPO_4F$ cathode materials, V-based materials have attracted great attention, including $NaVPO_4F$, $Na_3V_2(PO_4)_2F_3$, $Na_{1.5}VOPO_4F_{0.5}$, $Na_3V_2O_{2x}(PO_4)_2F_{3-2x}$, etc.. $Na_3V_2(PO_4)_2F_3$ possesses a better dynamic performance, since in the crystal structure of this material, tunnels along (001) and (100) directions provide space for the reversible insertion/desertion of sodium ions. [48]

Kang et al firstly proved the sodium storage process in the $Na_3V_2(PO_4)_2F_3$ to be a single-phase reaction. [49] With the substitution of F, the voltage plateau could increase to 3.7 V and 4.2 V with a specific capacity of 108 mAh g^{-1} after 30 cycles. On this basis, some researchers partially replaced F by O and developed the $Na_3V_2O_{2x}(PO_4)_2F_{3-2x}$ with a novel structure. When applied as the cathode material for sodium ion batteries, two voltage plateaus appeared at 3.6 V and 4.0 V, and a specific capacity of 87 mAh g^{-1} was delivered. [50] Furthermore, it turns out that the electrochemical performance of the $Na_3V_2O_{2x}(PO_4)_2F_{3-2x}$ cathode material can be improved by carbon coating or coating other conductive metal oxides. [51,52]

Na_2FePO_4F is another widely studied $NaMPO_4F$ (M=Fe, Co, Ni, Mn, V, etc.) cathode material in sodium ion batteries. Tarascon's group compared the electrochemical performance of the Na_2FePO_4F synthesized by the solid-state method and the ionothermal synthesis method, and found that the Na_2FePO_4F prepared by the ionothermal synthesis method with smaller particle size could deliver better electrochemical performance. [53] It was reported that this material could permit the reversible insertion/desertion of one sodium ion with nearly no volume expansion. [54]

According to these previous reports, it was found that the average voltages for the $NaMPO_4F$ cathode material are higher than that of the cathode materials without F substitution. Therefore, an electrode material with a higher working voltage can be obtained by F substitution, which provides an important methodology to develop new electrode materials.

1.4.1.8 Other cathode materials

Organic compounds are also considered as promising electrode materials attributed to the high theoretical specific capacity, abundant resource, low cost and flexible design. To date, organic small molecules such as hydrazine, anhydrides, amides, and phenols as well as polymers have all been employed as cathode materials for sodium ion batteries. [55-57] However, the solubility of organic electrode materials in electrolyte solution remains to be an issue before further

applications can be realized. In addition, fluoride and metal oxides have also been investigated as cathode materials for sodium ion batteries. [58,59]

1.4.2 Anode materials of sodium ion batteries

Anode materials play an important role in the component of sodium ion batteries and thus are widely investigated as another research hotspot. In fact, sodium metal was directly used as an anode material for sodium ion batteries in previous articles. However, in the cycling process, sodium would deposit inhomogeneously on the surface of the electrode and lead to the growth of the dendrite, which may penetrate the diaphragm and result in safety issues. Therefore, most researchers choose to develop alloys or materials that can permit the insertion/desertion of sodium ions as the anode material for sodium ion batteries.

An effective anode material should satisfy the demands as follows:

(1) A low sodium ion insertion potential; when matched with cathode materials, a low insertion potential can be beneficial to achieve a high average working voltage and to improve the power density of full cells.

(2) Low polarization for sodium ion insertion to ensure a high energy storage efficiency;

(3) Good structural stability during cycling process;

(4) Abundant resource and low cost.

1.4.2.1 Carbon materials

Graphite exhibits excellent electrochemical properties as an anode for the lithium ion batteries and has been employed as the anode material for the commercial lithium ion batteries. During the charging process, lithium ion could easily insert into the layer structure of the graphite to form a LiC_6 structure compound. [60,61] However, when it is applied to the sodium ion batteries, it was proved that sodium ions are difficult to insert into the layer structure of the graphite due to the large radius, which leads to low specific capacity and poor reversibility. [62]

Soft carbon is a kind of disordered carbon obtained by heat treating the carbon to the graphitization temperature and thus has a relatively higher graphitization degree. Early in the 1990s, Doeff et al studied the sodium ion storage in graphite, petroleum and coke. The battery

was tested at 86ºC and only achieved a discharge capacity of 85 mAh g^{-1}.[63] The study about the sodium ion insertion properties in the asphalt carbon fiber was not ideal as well.[64] Thereafter, there was not a lot of research on soft carbon as an anode for sodium ion battery.

On the contrary, hard carbon is a kind of disordered carbon that is difficult to be graphitization such as carbon black, resin carbon and so on. Hard carbon can achieve high specific capacity in lithium ion battery and has already be used in practical applications.[65] To date, hard carbon is also the earliest and the most widely studied anode material in the sodium ion batteries attributing to its high sodium ion insertion potential. Stevens and his group firstly proved the reversibility of Na^+ insertion into hard carbon and delivered a reversible specific capacity of 300 mAh g^{-1}. [66] Komaba et al assembled a full sodium ion battery using $NaNi_{0.5}Mn_{0.5}O_2$ as the cathode and hard carbon as the anode and then improve the electrochemical performance by optimizing the electrolyte and the microstructure of the hard carbon. [67] The Columbic efficiency for the first cycle was increased to 90% and a discharge capacity of 220 mAh g^{-1} could be obtained after 100 cycles. Meanwhile, it was reported by Tirado's group that carbon black owns a reversible specific capacity of ~200 mAh g^{-1} while the Columbic efficiency was only 82.2%.[68] According to these investigations, hard carbon materials showed high specific capacity as the anode materials for the sodium ion batteries. However, the poor rate properties and cycling stability, as well as the high cost, have limited the further application of the hard carbon.

Graphene, due to its large surface area and excellent conductivity, has also been applied in sodium ion batteries. However, unlike lithium ion batteries, the specific capacity for directly-used graphene as the anode material in sodium ion batteries is limited which may be attributed to the larger radius of the sodium ions. Therefore, more studies are focus on the synthesis and the application of the graphene composites as the anode material for sodium ion batteries, such as Sb/reduced graphene oxide (rGO) composite, phosphorous/graphene composite, metal oxide-graphene, etc. [69-71] Despite of the increased discharge capacity, the cycling stability of the graphene composite in sodium ion batteries still needs to be improved for further practical applications.

1.4.2.2 Alloying anode materials

Alloys possess very high energy densities and low redox potentials. However, the research on the sodium alloy materials as an anode for the sodium ion batteries are much less than in the lithium ion batteries. Similar to the lithium, sodium can also form sodium alloy with In, Sn, Sb, Ge and other metals. The alloy formation process can be expressed as the reaction equation below:

$$M + xNa^+ + xe^- \rightarrow Na_xM \text{ (M=Si, Ge, Sn, Pb, Ga, Sb, In, Zn, etc.)} \qquad (1\text{-}1)$$

It was reported that in lithium ion batteries lithium could form an alloy with Si—$Li_{4.4}Si$ with a high theoretical specific capacity of 4200 mAh g^{-1}. [72] However, although sodium can also form an alloy with Si, to date there is no related report about NaSi employed directly as the anode material for sodium ion batteries, which may be due to the significant and irreversible volume expansion of Si in sodium ion batteries. It is worth noting that the alloy anode materials can combine with a large number of sodium ions and achieve a much higher specific capacity than the hard carbon. Tin and Sb are the most investigated alloy anode materials in sodium ion batteries. Tin could form a Na_4Sn alloy with Na with a theoretical specific capacity of 847 mAh g^{-1}. The practical Na^+ insertion process into Tin can be expressed as following: Sn-$Na_{0.6}$Sn-$Na_{1.2}$Sn-Na_5Sn_2-$Na_{15}Sn_4$.[73] For the electrochemical reaction mechanism of the Sb in sodium ion batteries, during the insertion process sodium ions firstly insert into the Sb to form an amorphous Na_xSb and further transform to the hexagonal/cubic Na_3Sb, and then finally completely transform to the hexagonal Na_3Sb.

However, the large volume expansion during the cycling process is twice as high as the same process in lithium ion batteries, resulting in a poor cycling stability. Since the volume expansion increases with the increasing inserted Na^+ numbers, the discharge capacity would fade quickly following the cycling times. To solve this problem, researchers have carried out various attempts, such as replacing binders, adding electrolyte additives and preparing nanostructured materials. Employing sodium polyacrylate (PAANa) as the binder instead of PVDF was proved to be effective to improve the electrochemical stability of the Na-Sn alloy. The discharge capacity was improved to 880 mAh g^{-1} by this method while the capacity retention was enhanced as well.[74] Zhou et al composited Sb nanoparticles by a wet grinding method with multiwall carbon

nanotubes, and further improved the discharge capacity as well as electrode stability through adding FEC in the electrolyte solution. [75]

Sn-Sb alloys were also investigated as the anode material for sodium ion batteries. For instance, the SnSb/C composite crafted by a high-energy ball milling method could deliver a capacity retention of 80% for 50 cycles and a high specific capacity of 544 mAh g^{-1}, which was nearly twice as much as the capacity of carbon-based composites. [76]

1.4.2.3 Ti-based materials

Ti-based materials, including titanium dioxide with different phases and titanate compound, have been widely applied in supercapacitors, [77] lithium ion batteries, [78] solar cells and other energy storage systems. [79] In recent years, many researchers are dedicated to the application of the Ti-based materials in the sodium ion batteries, due to the low toxicity, abundance, excellent cycling stability and safety. [80,81]

The crystal phases of TiO_2 in nature mainly include the anatase, the rutile and the brookite. Both the anatase and the rutile TiO_2 belong to the tetragonal system and are composed of interconnected octahedrons. In a typical anatase TiO_2 phase, each octahedron is connected with the adjacent octahedrons by four edge-sharing and four vertex-sharing, while the octahedrons in the rutile TiO_2 are connected by two edge-sharing and eight vertex-sharing. Apart from these two phases, the brookite TiO_2 is classified as the orthorhombic system, in which a unit cell is composed of six TiO_2 molecules. According to the different crystal structures, TiO_2 with different phases possess different sodium storage mechanisms. As an anode material for the lithium ion batteries, TiO_2 can achieve a high reversible capacity of more than 200 mAh g^{-1} as well as a long cycling life. Thus, the sodium storage properties of TiO_2 have also been investigated a lot in latest years.

The amorphous TiO_2 is the earliest studied TiO_2 material as the anode in the sodium ion batteries. Xiong et. al firstly employed the amorphous TiO_2 directly grown on Ti substrate as the anode for sodium ion batteries. Interestingly, it was found that the specific capacity of the amorphous TiO_2 gradually increased with the cycling times.[82] However, the amorphous TiO_2 lead to a mismatch between the charging-discharging profiles and the cycles, thus the anatase was early considered to be inactive in sodium ion batteries. Soon afterward, Kim's group

investigated the electrochemical activities of the anatase TiO_2 in sodium ion batteries and improved the conductivity by carbon coating.[83] As a result, an initial specific capacity close to the theoretical capacity was obtained.

As a widely applied titanate in lithium ion batteries, the lithium ion insertion/desertion into the $Li_4Ti_5O_{12}$ belongs to a two-phase mechanism with a lithium insertion potential of 1.5 V. It is worth noting that the volume of the $Li_4Ti_5O_{12}$ does not change during the electrochemical reaction process that guaranteed a good cycling stability. [84,85] Different from this, the sodium ion insertion/desertion into the $Li_4Ti_5O_{12}$ belongs to a three-phase mechanism with a sodium insertion potential of ~ 1 V. Moreover, the sodium ion insertion process into the $Li_4Ti_5O_{12}$ is no longer a zero-strain process, leading to a decreased reversibility. [86] In addition, the electrochemical properties of the $Li_2Ti_3O_7$ in sodium ion batteries have also been investigated.

Due to the excellent electrochemical performance of the lithium titanate in lithium ion batteries, sodium titanates are also considered to be promising anode materials for sodium ion batteries for their similar tunnel crystal structure and high specific surface area. The general chemical formula for the sodium titanate is $Na_2Ti_nO_{2n+1}$ or $Na_4Ti_nO_{2n+2}$, while among them some sodium titanates are unstable or possess a more complicated structure than general ternary compounds. The crystal structure of the sodium titanate can divide into two categories, namely the layer structure and the tunnel structure. A typical representative for the layer structure sodium titanate is $Na_2Ti_3O_7$. It was reported that monoclinic structure $Na_2Ti_3O_7$ could permit the insertion of two sodium ions at ~0.3 V and deliver a specific capacity of 200 mAh g^{-1}.[87] Rudola et al. studied the relationships between the sintering temperature, the sintering time, the grinding method and the electrochemical performance of bulk $Na_2Ti_3O_7$ materials. [88] The results indicated that $Na_2Ti_3O_7$ with smaller particle size by sintering at 750ºC for 20 h achieved the highest capacity of 177 mAh g^{-1} at a current rate of 0.1 C due to the shorter diffusion distance of the sodium ions. In addition, $Na_2Ti_3O_7$ nanotubes directly grown on Ti substrate exhibited high reversible specific capacity of 221 mAh g^{-1} with excellent cycling stability. [89] In addition, other sodium titanates such as $Na_2Ti_6O_{13}$, $Na_2Ti_7O_{15}$ and $Na_2Ti_9O_{19}$ were also researched as anodes for sodium ion batteries. [90-92]

1.4.2.4 Two-dimensional (2D) nanostructure anode materials

The 2D material is a kind of crystalline material which consists of a single layer of atoms. Generally, the layers of 2D materials are combined by Van del Waals forces. Graphene, as the first studied 2D material, has been widely applied in commercial ESSs, to date over 700 kinds of 2D materials have been found and developed. In addition, the large surface area and controllable morphology make the 2D material to be a promising candidate for the rechargeable batteries.

Phosphorous owns three allotropes, which are white phosphorous, red phosphorous and black phosphorous. Among them, black phosphorous is the most stable one with a layer network structure like graphite, which was suitable for the insertion of the alkaline ions. Moreover, black phosphorous possesses a low band gap of 0.34 eV and a high electronic conductivity of ca. 100 S m^{-1}. Therefore, in recent years the alkaline metal ion storage capabilities of black phosphorous have attracted a great many attention. It had been already calculated that phosphorous possesses an extremely high theoretical specific capacity of 2596 mAh g^{-1} as the electrode material for the rechargeable batteries. The sodium ion storage mechanism of the black phosphorus was firstly proposed by Hembram et al. through the first principle calculation. [93] They thought the P-P bond would break during the sodium insertion process and then an amorphous phosphorus was formed. Afterward, it was reported that in fact, the P atoms of black phosphorus alloyed with sodium and finally formed a Na_3P compound. [94] Furthermore, by compositing with carbon to form a stable phosphorous-carbon bond, the structural stability of the black phosphorus could be enhanced. [95, 96] However, the preparation method, as well as the stability, still need to be improved for further application.

In recent years, metal sulfides have also been popular electrode materials for the rechargeable batteries because of the high theoretical specific capacity and their controllable morphology. Early in the 1970s, metal sulfides were introduced to lithium ion batteries and delivered high specific capacity and excellent cycling stability. [97] To date, there are also a great many reports about the applications of the metal sulfides in sodium ion batteries, especially about MoS_2 and related composites. For instance, the MoS_2 nanosheet prepared by liquid-phase exfoliation was reported by Bang's group, which exhibited a specific capacity of 161 mAh g^{-1} after 50 cycles at a current rate of 0.02C. [98] Choi et al. reported a super stable MoS_2/graphene microsphere composite that maintained a high discharge capacity of 322 mAh g^{-1} even after cycling for 600

times at 1.5C. [99] In addition, WS_2 nanowires could retain a high specific capacity of 330 mAh g^{-1} at a current rate of 1C with excellent cycling stability, as reported by Liu et al. [100] Wolter et al prepared FeS_2 nanocrystals via liquid reaction, and a specific capacity of 500 mAh g^{-1} was delivered at a current rate of 1C. [101] However, there are still some challenges for the application of the metal sulfides, such as the side reactions occur in the initial cycle, the large volume expansion during cycling as well as the low conductivity.

MXene, as a new member of the 2D layer materials, has also been one of the current research hotspots. MXene is actually transition metal carbides or nitrides with graphene-like layer structure. Generally, the chemical formula for MXene is $M_{n+1}X_n$ (n=1, 2, 3; M is transition metal element, while X is carbon or nitrogen element). To date, dozens of MXene materials have been predicted to exist, while among them 19 kinds of MXene have already been synthesized successfully. Such a diversified structural composition can provide a broad developing prospect for the regulation of properties as well as derivative materials. Moreover, compared with other traditional 2D materials, the abundant –F, -OH and other functional groups on the surface of the MXene are also beneficial to for an excellent chemical reactivity and hydrophilicity. Among various MXene materials, Ti_3C_2 have already been widely studied and applied in the rechargeable batteries. Kajiyama et al. firstly reported that Ti_3C_2 powder exhibited a specific capacity of 100 mAh g^{-1} at a current density of 20 mA g^{-1}. [102] Afterwards, a MoS_2/Ti_3C_2 composite was prepared by Wu et al, which delivered a discharge capacity of 251 mAh g^{-1} at a current density of 100 mA g^{-1}. [103] In addition, Gogotasi's group investigated three different MXene materials, which are Mo_2C, Ti_3C_2, V_2C. [104] At a same current rate of 0.2C, these three materials achieved discharge capacity of 370, 330 and 340 mAh g^{-1}, respectively. Even at a high current rate of 25C, the discharge capacity of 125, 120 and 170 mAh g^{-1} could be obtained for the three MXene materials.

1.4.2.5 Other anode materials

Organic materials possess advantages such as abundant sources and low cost, thus are also studied as the anode materials for the rechargeable batteries. After the investigation about the application of the conjugated dicarboxylic acid-based organic compounds on lithium ion batteries, $Na_2C_8H_4O_4$ was also studied as anode materials for sodium ion batteries. It turned out that the $Na_2C_8H_4O_4$ could permit reversible insertion/desertion of two sodium ions. [105] Wang's

group prepared a sodium benzene-dicarboxylate and further used it as a precursor to obtaining another sodium 4, 4'-stilbene-dicarboxylate. The two materials exhibited discharge capacities of 180 and 112 mAh g^{-1} at a current rate of 50 mA g^{-1}, respectively. [106] Thus, organic electrode materials would also be a good choice for the high-performance sodium ion batteries in the future.

1.5 Issues

With the substantial industrialization of the lithium ion batteries, the demand for the lithium has been greatly increased, which results to the higher prices of the raw materials and limits the further promotion and application. Thus, the research and the development of the sodium ion batteries can be of no doubt to alleviate the limited battery development issues caused by the shortage of the lithium resources. However, there have been still some issues, which restrict the further application of sodium ion batteries, such as the low power density and the limited electrode materials. Since the radius of sodium ion is larger than lithium ion, some available electrode materials in lithium ions may not be able to permit the reversible insertion/desertion of sodium ions. Thus, it is urgent to develop more available novel electrode materials for sodium ion batteries. Nowadays, the anode materials for the sodium ion batteries are mostly hard carbon, which owns relatively high specific capacity but not high safety or long cycling life. It is necessary to investigate and develop some replaceable anode materials with both high capacity and cycling stability.

1.6. Objectives of this work and the organization

Nanostructured electrode materials have been regarded as a new direction for the rechargeable batteries since these materials possess high specific surface areas that are beneficial to increase the specific capacity and the stability. Therefore, different kinds of nanostructured materials were prepared and employed as the anode materials for the sodium ion batteries. In Chapter 3, we prepared TiO_2 nanopills derived from the metal-organic framework with a high specific surface area to improve the discharge capacity and the cycling stability. In Chapter 4, we prepared and investigated the electrochemical performance of a feather-like MnO_2 on carbon paper, which possesses a higher theoretical specific capacity than TiO_2. In Chapter 5, black phosphorous with high conductivity and theoretical specific capacity was used to composite with the Ti_3C_2 to achieve a better specific capacity. In Chapter 6, we attempted to synthesize new layer structure

double transition metal carbides as the electrode materials for the sodium storage application according to the preliminary understanding of MXene materials from Chapter 5. The relationship between morphology, structure, crystal phase and reaction conditions (such as reacting time, temperature, the molar ratios of raw materials, etc.) were discussed. In addition, the electrochemical reaction process and the mechanism of the sodium ion insertion/desertion process in these electrode materials were investigated as well, which can offer a theoretical basis for the design and the preparation of new anode materials in the practical sodium ion batteries.

References

[1] Slater M., Kim D., Lee E., et al. Sodium-ion batteries. ***Adv. Funct. Mater.,*** 2013, 23(8): 947-958.

[2] Palomares V., Serras P., Villaluenga I., et al. Na-Ion batteries, recent advances and present challenges to become low cost energy storage systems. ***Energy Environ. Sci,*** 2012, 5(3): 5884-5901.

[3] Huilin Pan, Yongsheng Hu, Hong Li, et al. Recent progress in structure study of electrode materials for room-temperature sodium-ion stationary batteries. ***Scientia Sinica Chimica***, 2014, 44(8): 1269-1279.

[4] Ellis B., Nazar L. Sodium and sodium-ion energy storage batteries. ***Curr. Opin. Solid St. M.***, 2012, 16(4): 168-177.

[5] Thomas P., Billaud D. Effect of mechanical grinding of pitch-based carbon fibers and graphite on their electrochemical sodium insertion properties. ***Electrochim. Acta,*** 2000, 46(1): 39-47.

[6] Whittingham M. Chemistry of intercalation compounds: metal guests in chalcogenide hosts. ***Prog. Solid State Chem.***, 1978, 12(1): 41-99.

[7] Mendiboure A., Delmas C., Hagenmuller P. Electrochemical intercalation and deintercalation of Na_xMnO_2 bronzes. ***J. Solid State Chem.***, 1985, 57(3): 323-331.

[8] Delmas C., Braconnier J., Fouassier C., et al. Electrochemical intercalation of sodium in Na_xCoO_2 bronzes. ***Solid State Ionics***, 1981, 3-4: 165-169.

[9] Ding J., Zhou Y., Sun Q., et al. Cycle performance improvement of $NaCrO_2$ cathode by carbon coating for sodium ion batteries. ***Electrochem Commun***, 2012, 22: 85-88.

[10] Ma X, Chen H, Ceder G. Electrochemical properties of monoclinic $NaMnO_2$. ***J. Electrochem. Soc.***, 2011, 158(12): A1307-A1312.

[11] Doeff M., Peng M., Ma Y., et al. Orthorhombic Na_xMnO_2 as a cathode material for secondary sodium and lithium polymer batteries. ***J. Electrochem. Soc.***, 1994, 141(11): 145-147.

[12] Hosono E., Saito T., Hoshino J., et al. High power Na-ion rechargeable battery with single-crystalline $Na_{0.44}MnO_2$ nanowire electrode. ***J. Power Sources***, 2012, 217: 43-46.

[13] Billaud J, Clément R., Armstrong R., et al. β-$NaMnO_2$: A high-performance cathode for sodium-ion batteries. ***J. Am. Chem. Soc.***, 2014, 136(49): 17243-17248.

[14] Yabuuchi N., Kajiyama M., Iwatate J., et al. P2-type $Na_x[Fe_{1/2}Mn_{1/2}]O_2$ made from earth-abundant elements for rechargeable Na batteries. ***Nat.Mater***.2012, 11: 512-517.

[15] Mortemard B, Carlier D., Guignard M., et al. P2-$Na_xMn_{1/2}Fe_{1/2}O_2$ phase used as positive electrode in Na batteries: structural changes induced by the electrochemical (De) intercalation process. ***Inorg. Chem.***, 2014, 53(20): 11197-11205.

[16] Yamada A., Chung S., Hinokuma K. Optimized $LiFePO_4$ for lithium battery cathodes. ***J. Electrochem. Soc.***, 2001, 148(3): 224-229.

[17] Huang Y., Goodenough J. High-rate $LiFePO_4$ lithium rechargeable battery promoted by electrochemically active polymers. ***Chem. Mater.***, 2008, 20(23): 7237-7241.

[18] Delmas C., Maccario M., Croguennec L., et al. Lithium deintercalation in $LiFePO_4$ nanoparticles via a domino-cascade model. ***Nat. Mater.***, 2008, 7(8): 665-671.

[19] Zaghib K., Trottier J., Hovington P., et al. Characterization of Na-based phosphate as electrode materials for electrochemical cells. ***J. Power Sources***, 2011, 196: 9612-9617.

[20] Oh S., Myung S., Hassoun J., et al. Reversible $NaFePO_4$ electrode for sodium secondary batteries. ***Electrochem. Commun.***, 2012, 22: 149-152.

[21] Zhu Y, Xu Y, Liu Y, et al. Comparison of electrochemical performances of olivine $NaFePO_4$ in sodium-ion batteries and olivine $LiFePO_4$ in lithium-ion batteries. ***Nanoscale***, 2013, 5(2): 780-787.

[22] Moreau P., Guyomard D., Gaubicher J., et al. Structure and stability of sodium intercalated phases in olivine $FePO_4$. ***Chem. Mater.***, 2010, 22(14): 4126-4128.

[23] Galceran M, Saurel D, Acebedo B, et al. The mechanism of NaFePO 4 (de) sodiation determined by in situ X-ray diffraction. ***Phys. Chem. Chem. Phys.***, 2014, 16(19): 8837-8842.

[24] Kim J., Seo D., Kim H., et al. Unexpected discovery of low-cost maricite $NaFePO_4$ as a high-performance electrode for Na-ion batteries, ***Energy Environ. Sci.***, 2015, 8: 540-545.

[25] Barpanda P, Ye T, Nishimura S, et al. Sodium iron pyrophosphate: A novel 3.0 V iron-based cathode for sodium-ion batteries. ***Electrochem. Commun.***, 2012, 24: 116-119.

[26] Barpanda P, Liu G, Ling C D, et al. $Na_2FeP_2O_7$: a safe cathode for rechargeable sodium-ion batteries. ***Chem. Mater.***, 2013, 25(17): 3480-3487.

[27] Kim H, Shakoor R A, Park C, et al. $Na_2FeP_2O_7$ as a promising iron-based pyrophosphate cathode for sodium rechargeable batteries: a combined experimental and theoretical study. ***Adv. Funct. Mater.***, 2013, 23(9): 1147-1155.

[28] Barpanda P, Ye T, Avdeev M, et al. A new polymorph of $Na_2MnP_2O_7$ as a 3.6 V cathode material for sodium-ion batteries. ***J. Mater. Chem. A***, 2013, 1(13): 4194-4197.

[29] Barpanda P, Avdeev M, Ling C D, et al. magnetic structure and properties of the $Na_2CoP_2O_7$ pyrophosphate cathode for sodium-ion batteries: a supersuperexchange-driven non-collinear antiferromagnet. ***Inorg. Chem.***, 2012, 52(1): 395-401.

[30] Barpanda P., Liu G., Avdeev M., et al. *t*-$Na_2(VO)P_2O_7$: a 3.8 V pyrophosphate insertion material for sodium-ion batteries, ***ChemElectroChem***, 2014, 1(9): 1488-1491.

[31] Hong H. Crystal-structures and crystal-chemistry in system $Na_{1+x}Zr_2Si_xP_{3-x}O_{12}$. ***Mater. Res. Bull.***, 1976, 11(2): 173-182.

[32] Jian Z., Zhao L., Pan H., et al. Carbon coated $Na_3V_2(PO_4)_3$ as novel electrode material for sodium ion batteries. ***Electrochem. Commun.***, 2012, 14(1): 86-89.

[33] Barpanda P, Oyama G, Nishimura SI, Chung SC, Yamada A. A 3.8 V earth-abundant sodium battery electrode. ***Nat. Commun.***, 2014, 5: 4358.

[34] Barpanda P, Oyama G, Ling C D, et al. Kröhnkite-Type $Na_2Fe(SO_4)_2{\cdot}2H_2O$ as a Novel 3.25 V Insertion Compound for Na-Ion Batteries. ***Chem. Mater.***, 2014, 26(3): 1297-1299.

[35] Oyama G, Nishimura S, Suzuki Y, et al. Off-Stoichiometry in Alluaudite-Type Sodium Iron Sulfate $Na_{2+2x}Fe_{2-x}(SO_4)_3$ as an Advanced Sodium Battery Cathode Material. ***ChemElectroChem***, 2015, 2(7): 1019-1023.

[36] Meng Y, Yu T, Zhang S, et al. Top-down synthesis of muscle-inspired alluaudite $Na_{2+2x}Fe_{2-x}(SO_4)_3$/SWNT spindle as a high-rate and high-potential cathode for sodium-ion batteries. ***J. Mater. Chem. A***, 2016, 4(5): 1624-1631.

[37] Araujo R B, Islam M S, Chakraborty S, et al. Predicting electrochemical properties and ionic diffusion in $Na_{2+2x}Mn_{2-x}$ $(SO_4)_3$: crafting a promising high voltage cathode material. ***J. Mater. Chem. A***, 2016, 4(2): 451-457.

[38] Reynaud M, Rousse G, Abakumov A M, et al. Design of new electrode materials for Li-ion and Na-ion batteries from the bloedite mineral $Na_2Mg(SO_4)2{\cdot}4H_2O$. ***J. Mater. Chem. A***, 2014, 2(8): 2671-2680.

[39] Qian J F, Zhou M, Cao Y. $Na_xM_yFe(CN)_6$ (M= Fe, Co, Ni): A new class of cathode materials for sodium ion batteries. ***J. Electrochem.***, 2012, 18(2): 108-112.

[40] Lu Y, Wang L, Cheng J, et al. Prussian blue: a new framework of electrode materials for sodium batteries. ***Chem. Commun.***, 2012, 48(52): 6544-6546.

[41] Wang L, Lu Y, Liu J, et al. A superior low-cost cathode for a Na-ion battery. ***Angew. Chem. Int. Ed.***, 2013, 52(7): 1964-1967.

[42] Yang D, Xu J, Liao X Z, et al. Structure optimization of Prussian blue analogue cathode materials for advanced sodium ion batteries. ***Chem. Commun.***, 2014, 50(87): 13377-13380.

[43] Yang D, Xu J, Liao X Z, et al. Structure optimization of Prussian blue analogue cathode materials for advanced sodium ion batteries. ***Chem. Commun.***, 2014, 50(87): 13377-13380.

[44] Li W J, Chou S L, Wang J Z, et al. Multifunctional conducing polymer coated $Na_{1+x}MnFe(CN)_6$ cathode for sodium-ion batteries with superior performance via a facile and one-step chemistry approach. ***Nano Energy***, 2015, 13: 200-207.

[45] Takachi M, Matsuda T, Moritomo Y. Cobalt hexacyanoferrate as cathode material for Na^+ secondary battery. ***Appl. Phys. Express***, 2013, 6(2): 025802.

[46] Wessells C., Huggins R., Cui Y. Copper hexacyanoferrate battery electrodes with long cycle life and high power. ***Nat. Commun.***, 2011, 2: 550.

[47] Wessells C., Peddada S., Huggins R., et al. Nickel hexacyanoferrate nanoparticle electrodes for aqueous sodium and potassium ion batteries. ***Nano Lett.***, 2011, 11(12): 5421-5425.

[48] Shakoor R., Seo D., Kim H., et al. A combined first principles and experimental study on $Na_3V_2(PO_4)_2F_3$ for rechargeable Na batteries. ***J. Mater. Chem.***, 2012, 22(38): 20535-20541.

[49] Shakoor R A, Seo D H, Kim H, et al. A combined first principles and experimental study on $Na_3V_2(PO_4)_2F_3$ for rechargeable Na batteries. ***J. Mater. Chem.***, 2012, 22(38): 20535-20541.

[50] Sauvage F, Quarez E, Tarascon J M, et al. Crystal structure and electrochemical properties *vs.* Na^+ of the sodium fluorophosphate $Na_{1.5}VOPO_4F_{0.5}$. ***Solid State Sciences***, 2006, 8(10): 1215-1221.

[51] Serras P, Palomares V, Goñi A, et al. High voltage cathode materials for Na-ion batteries of general formula $Na_3V_2O_{2x}(PO_4)_2F_{3-2x}$. ***J. Mater. Chem.***, 2012, 22(41): 22301-22308.

[52] Peng M, Li B, Yan H, et al. Ruthenium-oxide-coated sodium vanadium fluorophosphate nanowires as high-power cathode materials for sodium-ion batteries. ***Angew. Chem. Int. Ed.***, 2015, 54(22): 6452-6456.

[53] Recham N, Chotard J N, Dupont L, et al. Ionothermal synthesis of sodium-based fluorophosphate cathode materials. ***J. Electrochem. Soc.***, 2009, 156(12): A993-A999.

[54] Ellis B L, Makahnouk W R M, Makimura Y, et al. A multifunctional 3.5 V iron-based phosphate cathode for rechargeable batteries. ***Nat. Mater.***, 2007, 6(10): 749.

[55] Guo C, Zhang K, Zhao Q, et al. High-performance sodium batteries with the 9, 10-anthraquinone/CMK-3 cathode and an ether-based electrolyte. ***Chem. Commun.***, 2015, 51(50): 10244-10247.

[56] Luo W, Allen M, Raju V, et al. An organic pigment as a high-performance cathode for sodium-ion batteries. ***Adv. Energy Mater.***, 2014, 4(15).

[57] Deng W, Shen Y, Qian J, et al. A perylene diimide crystal with high capacity and stable cyclability for Na-ion batteries. ***ACS Appl. Mater. Interfaces***, 2015, 7(38): 21095-21099.

[58] Uchaker E, Zheng Y Z, Li S, et al. Better than crystalline: amorphous vanadium oxide for sodium-ion batteries. ***J. Mater. Chem. A***, 2014, 2(43): 18208-18214.

[59] Fu S Y, Li Y Z, Chu W, et al. Mesoporous amorphous FeOF nanococoons for high-rate and long-life rechargeable sodium-ion batteries. ***J. Mater. Chem. A***, 2015, 3(32): 16716-16727.

[60] Aurbach D., Markovsky B., Weissman I., et al. On the correlation between surface chemistry and performance of graphite negative electrodes for Li ion batteries. ***Electrochim. Acta***, 1999, 45(1): 67-86.

[61] Yata S., Kinoshita H., Komori M., et al. Structure and properties of deeply Li-doped polyacenic semiconductor materials beyond C_6Li. ***Synth. Met.***, 1994, 62(2): 153-158.

[62] Stevens D., Dahn J. The mechanisms of lithium and sodium insertion in carbon materials. ***J. Electrochem. Soc.***, 2001, 148(8): 803-811.

[63] Doeff M., Ma Y., Visco S., et al, Electrochemical Insertion of Sodium into Carbon**.** ***J. Electrochem. Soc.***, 1993, 140: 169-170.

[64] Thomas P., Ghanbaja J., Billaud D. Electrochemical insertion of sodium in pitch-based carbon fibres in comparison with graphite in $NaClO_4$–ethylene carbonate electrolyte. ***Electrochim. Acta***, 1999, 45(3): 423-430.

[65] Letellier M., Chevallier F., Clinard C., et al. The first in situ 7Li nuclear magnetic resonance study of lithium insertion in hard-carbon anode materials for Li-ion batteries. ***J. Chem. Phy.***, 2003, 118(13): 6038-6045.

[66]Stevens D., Dahn J. High capacity anode materials for rechargeable sodium-ion batteries. ***J. Electrochem. Soc.***, 2000, 147: 1271-1273.

[67] Komaba S.,Murata W., Ishikawa T., et al. Electrochemical Na insertion and solid electrolyte interphase for hard-carbon electrodes and application to Na-ion batteries. ***Adv. Funct. Mater.***, 2011, 21(20): 3859-3867.

[68]Alcantara R., Jimenez-Mateos J., Lavela P., et al. Carbon black: a promising electrode material for sodium-ion batteries. ***J. Electrochem. Commun.***, 2001, 3(11): 639-642.

[69] Nithya C, Gopukumar S. rGO/nano Sb composite: a high performance anode material for Na+ ion batteries and evidence for the formation of nanoribbons from the nano rGO sheet during galvanostatic cycling. ***J. Mater. Chem. A***, 2014, 2(27): 10516-10525.

[70] Sun J, Lee H W, Pasta M, et al. A phosphorene–graphene hybrid material as a high-capacity anode for sodium-ion batteries. ***Nat. Nanotechnol.***, 2015, 10(11): 980.

[71] Cha H A, Jeong H M, Kang J K. Nitrogen-doped open pore channeled graphene facilitating electrochemical performance of TiO_2 nanoparticles as an anode material for sodium ion batteries. ***J. Mater. Chem. A***, 2014, 2(15): 5182-5186.

[72] Morito H., Yamada T., Ikeda T., et al. Na–Si binary phase diagram and solution growth of silicon crystals. ***J. Alloys Compd.***, 2009, 480(2): 723-726.

[73] Chevrier V., Ceder G. Challenges for Na-ion negative electrodes. ***J. Electrochem. Soc.***, 2011, 158(9): 1011-1014.

[74] Komaba S, Matsuura Y, Ishikawa T, et al. Redox reaction of Sn-polyacrylate electrodes in aprotic Na cell. ***Electrochem. Commun.***, 2012, 21: 65-68.

[75] Wang J., Liu X., Mao S., et al. Microstructural evolution of tin nanoparticles during in situ sodium insertion and extraction. ***Nano lett.***, 2012, 12(11): 5897-5902.

[76] Xiao L, Cao Y, Xiao J, et al. High capacity, reversible alloying reactions in SnSb/C nanocomposites for Na-ion battery applications. ***Chem. Commun.***, 2012, 48(27): 3321-3323.

[77] Wang Y., Hong Z., Wei M., et al. Layered $H_2Ti_6O_{13}$-nanowires: a new promising pseudocapacitive material in non-aqueous electrolyte. ***Adv. Funct. Mater.***, 2012, 22(24): 5185-5193.

[78] Li J., Tang Z., Zhang Z. Layered hydrogen titanate nanowires with novel lithium intercalation properties. ***Chem. Mater.***, 2005, 17(23): 5848-5855.

[79] Pang A., Xia L., Luo H., et al. Highly efficient indoline dyes co-sensitized solar cells composed of titania nanorods. ***Electrochim. Acta***, 2013, 94: 92-97.

[80] Zhu G., Wang Y., Xia Y. Ti-based compounds as anode materials for Li-ion batteries. ***Energy Environ. Sci.***, 2012, 5(5): 6652-6667.

[81] Zhengsheng Hong, Mingdeng Wei. Research progress of anode materials for non-carbon lithium ion batteries. ***Advanced Materials Industry***, 2011, (4): 58-61.

[82] Xiong H., Slater D., Balasubramanian M., et al. Amorphous TiO_2 nanotube anode for rechargeable sodium ion batteries. ***J. Phys. Chem. Lett.***, 2011, 2(20): 2560-2565.

[83] Kim K., Ali G., Chung K., et al. Anatase titania nanorods as an intercalation anode material for rechargeable sodium batteries. ***Nano Lett.***, 2014, 14(2): 416-422.

[84] Hong Z., Lan T., Xiao F., et al. Ultrathin $Li_4Ti_5O_{12}$ nanosheets as a high performance anode for Li-ion battery. ***Funct. Mater. Lett.***, 2011, 4(4): 389-393.

[85] Chou S., Wang J., Liu H., et al. Rapid synthesis of $Li_4Ti_5O_{12}$ microspheres as anode materials and its binder effect for lithium-Ion battery. ***J. Phys. Chem. C***, 2011, 115(32): 16220-16227.

[86] Zhao L., Pan H., Hu Y., et al. Spinel lithium titanate ($Li_4Ti_5O_{12}$) as novel anode material for room-temperature sodium-ion battery. ***Chin. Phys. B***, 2012, 21(2): 028201.

[87] Senguttuvan P., Rousse G., Seznec V., et al. $Na_2Ti_3O_7$: lowest voltage ever reported oxide insertion electrode for sodium ion batteries. ***Chem. Mater.***, 2011, 23: 4109-4111.

[88] Rudola A., Saravanan K., Mason C., et al. $Na_2Ti_3O_7$: an intercalation based anode for sodium-ion battery applications. ***J. Mater. Chem. A***, 2013, 1(7): 2653-2662.

[89] Ni J, Fu S, Wu C, et al. Superior sodium storage in $Na_2Ti_3O_7$ nanotube arrays through surface engineering. ***Adv. Energy Mater.***, 2016, 6(11).

[90] Rudola A., Saravanan K., Devaraj S., et al. $Na_2Ti_6O_{13}$: a potential anode for grid-storage sodium-ion batteries. ***Chem. Commun.***, 2013, 49(67): 7451-7453.

[91] Li H, Fei H, Liu X, et al. In situ synthesis of $Na_2Ti_7O_{15}$ nanotubes on a Ti net substrate as a high performance anode for Na-ion batteries. ***Chem. Commun.***, 2015, 51(45): 9298-9300.

[92] Bhat S S M, Babu B, Feygenson M, et al. Nanostructured $Na_2Ti_9O_{19}$ for hybrid sodium-ion capacitors with excellent rate capability. ***ACS Appl. Mater. Interfaces***, 2017.

[93] Hembram KPSS, Jung H, Yeo BC, *et al*. Unraveling the atomistic sodiation mechanism of black phosphorus for sodium ion batteries by first-principles calculations. ***J Phys Chem C***, 2015, 119: 15041-15046.

[94] Dahbi M, Yabuuchi N, Fukunishi M, et al. Black phosphorus as a high-capacity, high-capability negative electrode for sodium-ion batteries: investigation of the electrode/electrolyte interface. ***Chem. Mater.***, 2016, 28(6): 1625-1635.

[95] Xu G L, Chen Z, Zhong G M, et al. Nanostructured black phosphorus/Ketjenblack–multiwalled carbon nanotubes composite as high performance anode material for sodium-ion batteries. ***Nano Lett.***, 2016, 16(6): 3955-3965.

[96] Song J, Yu Z, Gordin M L, et al. Chemically bonded phosphorus/graphene hybrid as a high performance anode for sodium-ion batteries. ***Nano Lett.***, 2014, 14(11): 6329-6335.

[97] Whittingham M S. Electrical energy storage and intercalation chemistry. ***Science***, 1976, 192(4244): 1126-1127.

[98] Bang G S, Nam K W, Kim J Y, et al. Effective liquid-phase exfoliation and sodium ion battery application of MoS_2 nanosheets. ***ACS Appl. Mater. Interfaces***, 2014, 6(10): 7084-7089.

[99] Choi S H, Ko Y N, Lee J K, et al. 3D MoS_2–graphene microspheres consisting of multiple nanospheres with superior sodium ion storage properties. ***Adv. Funct. Mater.***, 2015, 25(12): 1780-1788.

[100] Liu Y, Zhang N, Kang H, et al. WS_2 Nanowires as a High-Performance Anode for Sodium-Ion Batteries. ***Chem. Eur. J.***, 2015, 21(33): 11878-11884.

[101] Walter M, Zünd T, Kovalenko M V. Pyrite (FeS_2) nanocrystals as inexpensive high-performance lithium-ion cathode and sodium-ion anode materials. ***Nanoscale***, 2015, 7(20): 9158-9163.

[102] Kajiyama S, Szabova L, Sodeyama K, et al. Sodium-ion intercalation mechanism in MXene nanosheets. ***ACS nano***, 2016, 10(3): 3334-3341.

[103] Wu Y, Nie P, Jiang J, et al. MoS2-Nanosheet-Decorated 2D Titanium Carbide (MXene) as High-Performance Anodes for Sodium-Ion Batteries. ***ChemElectroChem***, 2017, 4(6): 1560-1565.

[104] Er D, Li J, Naguib M, et al. Ti_3C_2 MXene as a high capacity electrode material for metal (Li, Na, K, Ca) ion batteries. ***ACS Appl. Mater. Interfaces***, 2014, 6(14): 11173-11179.

[105] Park Y., Shin D., Woo S., et al. Sodium terephthalate as an organic anode material for sodium ion batteries. ***Adv. Mater.***, 2012, 24(26): 3562-3567.

[106] Wang C, Xu Y, Fang Y, et al. Extended π-conjugated system for fast-charge and-discharge sodium-ion batteries. ***J. Am. Chem. Soc.***, 2015, 137(8): 3124-3130.

Chapter 2 Experimental methods

In this chapter, the reagents and instruments used for the synthesis of materials, fabrication of coin cells and characterizations are listed as following. In addition, the measurement methods of physical characterizations and electrochemical properties are also introduced.

2.1 Reagents and apparatus

2.1.1 Reagents

Table 1 The list of laboratory reagent.

	Reagent	Purity	Company
1	Titanium isoproproxide($Ti(OiPr)_4$)	95%	Sigma-aldrich
2	1,4-Benzenedicarboxylic acid	99%	Sigma-aldrich
3	N,N-Dimethylmethanamide	99.9%	Wako Pure Chemical Industries
4	Methanol	99.7%	Wako Pure Chemical Industries
5	Potassium permanganate		Wako Pure Chemical Industries
6	Ethanol	Super Dehydrated	Wako Pure Chemical Industries
7	Carbon paper	98%	Tokyo Chemical Industry Co., LTD.
8	Ti_3AlC_2	99.8%	Forsman Scientific(Beijing) Co., LTD.

9	Red phosphorous	97.0%	Sigma-aldrich
10	Hydrofluoric acid	48%	Wako Pure Chemical Industries
11	Dimethyl sulfoxide	99.8%	Wako Pure Chemical Industries
12	Lithium chloride	99.0%	Wako Pure Chemical Industries
13	Graphite	99%	Sigma-aldrich
14	Mo powder	99.9%	Sigma-aldrich
15	Nb powder	99.85%	Sigma-aldrich
16	Tin powder	99.5%	Sigma-aldrich
17	Hydrochloric	36.0%	Wako Pure Chemical Industries
18	Potassium hydroxide	99.99%	Wako Pure Chemical Industries
19	Acetylene black	A.R.	Strem chemicals, LTD.
20	Sodium metal	99.8%	Sigma-aldrich
21	Acetone	99%	Wako Pure Chemical Industries
22	Polyvinylidene fluoride	A.R.	Apolle scientific, LTD.
23	Sodium perchlorate	98.0%	Fosai, China, Co., LTD.
24	Propylene carbonate	99.7%	Fosai, China, Co., LTD.
25	Ethylene carbonate	95.0%	Fosai, China, Co., LTD.
26	Fluorinated ethylene carbonate		Fosai, China, Co., LTD.
27	N-methyl pyrrolidone	99.0%	Wako Pure Chemical Industries
28	Copper foam	99.999%	Poxon, China, Co., LTD.

2.1.2 Apparatus

Table 2. The list of used laboratory apparatus.

Series	Apparatus	MODEL	Company
1	Electronic Balance	XFR-205DR	Shinko Denshi Co., LTD.
2	Muffle Furnace	FO300	Yamato Scientific Co., Ltd., Japan
3	Oven	SDN/W-27	Sansyo Co., Ltd., Japan
4	Hot plate	C-MAG HS7	IKA Co., Ltd., Germany
5	Vacuum oven	SVD-30	Sansyo Co., Ltd., Japan
6	ASU cleaner	ASU-6	As one Co., Ltd., Japan
7	Tabletop centrifuge	EX0800-A000	Kubota Co., Ltd., Japan
8	Hispeed mixing shaker machine	RM-05	Bunkou Keiki Co., Ltd., Japan
9	Hydraulic crimping machine	MSK-110	KJ Group Co., Ltd., China
10	Precision disc cutting machine	MSK-T10	KJ Group Co., Ltd., China
11	Glove box	Super(1220/750/900)	MIKROUNA Co., Ltd., Chian
12	Energy dispersive X-ray spectrometry	Genesis XM2	EDAX Co., Ltd., Japan
13	X-ray diffractometer	Rigaku	Rigaku Co., Ltd, Japan

14	Scanning electron microscope	JCM-6000	JEOL Co., Ltd, Japan
15	Tube Furnace	ARF-30KC	ASAHI RIKA Co., Ltd., Japan
16	Field emission-scanning electron microscope	S5200	Hitachi Co., Ltd., Japan
17	Battery measurement system	LAND-2001A	Wuhan LAND electronics Co., Ltd., China
18	Electrochemical workstation	CHI760E	CH Instruments Ins., China

2.2 Characterization methods

2.2.1 X-ray diffraction crystallography (XRD)

The X-ray diffraction (XRD) crystallography is a non-destructive analytical technique that can obtain information on the unit cell dimension. During the XRD test, an incident X-ray beam is diffracted by the crystal lattice thus generating a collection of diffracted beams into different specific directions. Based on the Bragg's law, these diffracted beams can be described as followed:

$$2dsin\theta = n\lambda \quad (2\text{-}1)$$

Where d is the spacing between the crystal planes, θ is the incident angle, n is an integer, and λ is the wavelength of the beam. The intensities and angles of these diffracted beams reveal the electron density map of the target sample, from which the in-depth information of the target including the mean atom positions, chemical bond details and lattice disorder, etc. By employing the XRD crystallography, researchers can identify the phases and analyze the molecular structures of crystalline samples.

The XRD patterns for the sample powders were obtained with an X-ray diffractometer (PANalytical X'Pert spectrometer) with Cu Kα irradiation (λ = 1.54056 Å). The sample was

prepared by depositing the powder to a clean and dry glass testing substrate before loading to the X-ray diffractometer. The XRD patterns were recorded by X'pert highscore. The scan range is from 5° to 80°, and the scan rate is 5°/min.

2.2.2 Field Emission Scanning Electron Microscopy (FE-SEM)

Field emission scanning electron microscopy (FE-SEM) is a type of electron microscopy technique that produces images of samples by scanning the surfaces with a focused beam of electrons. The electron beam interacts with atoms of different depth, generating various signals providing topographical and compositional information. The FE-SEM can reach a magnification up to 300,000 times, with the virtually unlimited depth of field. Comparing to ordinary scanning electron microscopy (SEM), FE-SEM yield images with higher resolution and less distortion.

The FE-SEM images for the samples were taken by JEOL JSM-6701F, with a working voltage of 7 kV and a working current of 15 μA. The sample powder was first deposited to the conductive adhesive tape attached to the sample holder, and then inserted to the vacuum chamber for observation.

2.2.3 Transmission electron microscopy (TEM)

Transmission electron microscopy (TEM) is a type of electron microscopy technique that acquires images by generating a beam of the focused electron beam to interact with the sample deposited on a copper grid or a carbon grid. The image is formed when the electron beam transmitted through the sample, then magnified and focused onto an imaging screen, a photographic film or a sensor. Owing to the smaller de Broglie wavelength of the electron, TEM can reach a significantly higher resolution and magnification than other microscopy techniques, enabling the capture of fine details. This is especially important with respect to the observation of the nanometer scale morphology of the nanoparticles.

In this thesis, the TEM images were taken by JEOL JEM-2100F with the acceleration voltage of 300 kV. The sample powder was dispersed into ethanol by the ultrasonic dispersion. The dispersion was then deposited on the copper grid and dried naturally in the ambient environment before loaded to the device.

2.2.4 X-ray photoelectron spectroscopy (XPS)

X-ray photoelectron spectroscopy (XPS) is a surface sensitive spectroscopic technique that can provide not only qualitative analysis but also quantitative analysis revealing various information of the target material including the elemental composition, empirical formula, chemical state, electronic state, etc. XPS equips a beam of X-ray to irradiate the target material, and record the number and the kinetic energy of the electrons escaping the surface of the target material. Since the energy of an X-ray with a particular wavelength, the kinetic energy of an emitted electron can be measured, the electron binding energy of each of the emitted electrons can be determined with the equation below:

$$E_{binding} = E_{photon} - (E_{kinetic} + \phi) \qquad (2\text{-}2)$$

Where $E_{binding}$ stands for the binding energy of a specific emitted electron, E_{photon} stands for the energy of the indicating X-ray photon, $E_{kinetic}$ stands for the kinetic energy of the electron measured, and ϕ stands for the work function dependent on the spectrometer and the material. It is to be noted that XPS can provide high detective limit up to the parts per thousand range.

Since XPS would only detect the surface of the target material in a range of ~10 nm, it usually required the testing specimen to be treated in order to expose the bulk chemistry. In this thesis, the testing specimen were grounded with an aluminum oxide mortar and dried to obtain a fine powder. The powder was sequentially deposited to the sample holder with carbon conductive tape before loaded to the Shimadzu AXIS-His instrument.

2.2.5 BET Surface Area Analysis (BET)

BET surface area analysis provides a quantitative evaluation of the precise specific surface area by measuring nitrogen multilayer adsorption as a function of the relative pressure. This fully automated analysis method reveals external and porous surface area as well as the pore size and its distribution, yielding critical information with respect to studying the impact of the surface porosity and the particle size in the specific research area.

The concept of the BET theory is an extension of the Langmuir monolayer molecular adsorption theory, described as the equation below:

$$\frac{1}{v[p_0/p]} = \frac{c-1}{v_m c}\left(\frac{p}{p_0}\right) + \frac{1}{v_m c} \quad (2\text{-}3)$$

where p and p_0 represent the equilibrium and the saturation pressure of the adsorbates at the specified temperature, v represent the adsorbed gas quantity in volumetric units, v_m represent the monolayer adsorbed gas quantity in volumetric units, and c represent the BET constant.

In practical scenarios, the volume of the adsorbate gas is measured at the boiling point of nitrogen, e.g. -196°C, and the amount of the adsorbed gas is correlated to the total surface area (including both external and pore surfaces) of the testing sample. The specific surface area and other information were obtained with subsequent calculations.

In this thesis, the surface area of the target sample was tested with standard BET test methods described above and the corresponding information was calculated.

2.3 Electrochemical measurements

2.3.1 Assembling of coin cells of sodium ion batteries

The samples need to be assembled as coin cells for electrochemical measurements. The fabrication of coin cells can be divided into two steps, which are the preparation of electrode and assembling process of batteries. In this thesis, the as-prepared materials are all used as anode electrode materials for sodium ion batteries. The preparation process of the anode electrode is listed as follows:

(1) Coating process

a. For the electrode preparation of powder materials, the as-prepared material (active material), acetylene black (conductive additive) and polyvinylidene fluoride (binder) are firstly dried at 110 ^{o}C for 12 h in the vacuum oven.

b. Then the dried materials are fully mixed by a certain mass ratio by grind milling and further mixed with NMP solvent to form a slurry.

c. The mixed slurry is uniformly coated on a current collector with a certain loading mass. For the preparation of anode electrode, copper foil is used as the current collector.

d. The obtained electrode pieces are dried at 110^{o}C for 12 h in the vacuum oven.

e. After the drying process, the electrode pieces are pressed with a compressor to enhance the tap density with a pressure value of about 4 MPa.

f. Weigh the mass of electrode pieces coated with materials. The weight of active materials are obtained by the following equation:

$$M_A = (M_E - M_S) * P_A \quad (2\text{-}4)$$

-

M_A : Mass of active materials;

M_E : Mass of electrode pieces coated with materials;

M_S : Mass of electrode pieces before coating;

P_A : Mass ratio of active materials.

(2) Assembling process

The sodium-ion half cells were assembled in a glove box filled with Ar atmosphere. The assembling process is shown in Figure 2-1. Na metal is directly used as a counter electrode, and glass fiber membrane (Whatman GF/F1825-047) was employed as a separator. The electrolyte is composed of 1M $NaClO_4$ dissolved in a mixed solution of propylene carbonate (PC) and ethylene carbonate (EC) (1:1 in volume) with fluorinated ethylene carbonate (FEC) as an electrolyte additive.

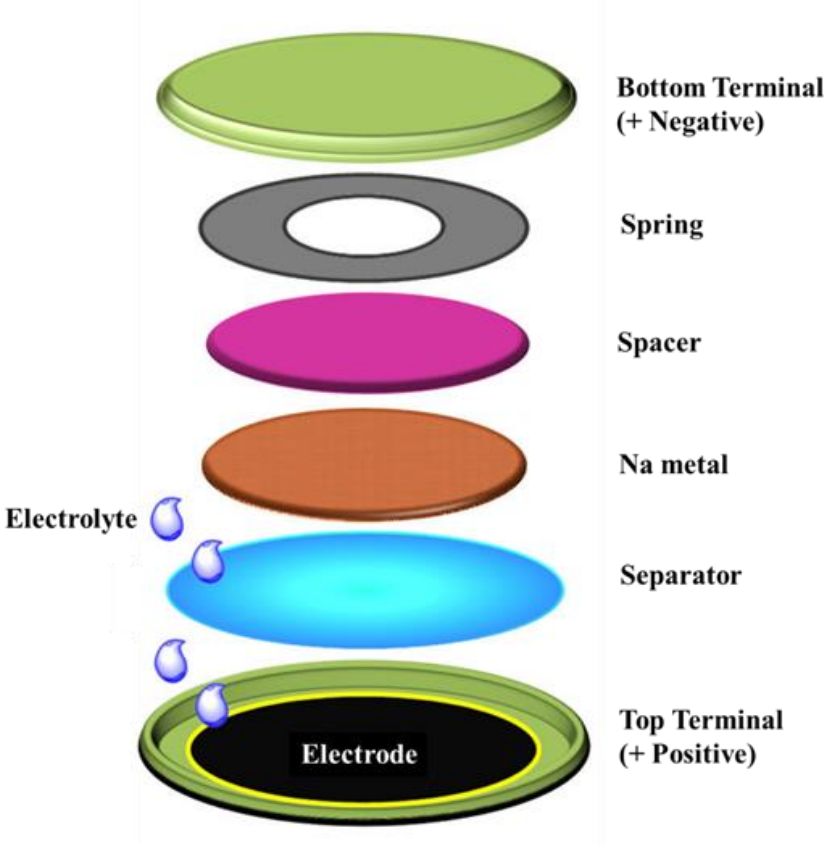

Figure 2-1 Schematic for the structure of a sodium-ion half-cell.

2.3.2 Electrochemical measurements

2.3.2.1 Calculation of theoretical specific capacity of electrode materials

The theoretical specific capacity of electrode materials can be calculated as the following equations:

$$\mathbf{C} = \frac{nF}{3600M} \tag{2-5}$$

n : Number of the transferred electronics;

F : Faraday constant;

M : Molar mass of the electrode material.

According to the theoretical specific capacity of electrode materials, some researchers measure the electrochemical performance of the electrode materials under different current rates, which is calculated as several times of the theoretical specific capacity (nC. C: theoretical specific capacity). However, in this thesis, we did not use this measurement method to test the electrochemical performance.

2.3.2.2 Cyclic Voltammetry (CV)

Cyclic voltammetry is a kind of potential dynamic electrochemical measurement. By applying an isosceles triangular pulse voltage to the working electrode, the working electrode potential is scanned repeatedly for once or more times at different rates. By choosing a potential range, various reduction and oxidation reactions can alternately occur on the electrode, and the current-potential curves will be recorded. This measurement can be used to measure the electrode reaction parameters, investigate the reaction mechanism, and observe the reactions occurred within the entire potential scan range etc.

In sodium ion batteries, by observing the oxidation peaks and reduction peaks in cyclic voltammetry curves we can confirm the electrochemical reaction mechanism of electrode materials including the products after the electrochemical reaction, the electrochemical-chemical coupling reaction, as well as electron transfer kinetics and so on. Furthermore, the reversibility of electrochemical reaction for the electrode materials can also be judged from the cyclic voltammetry measurement by the curves of different scan rates and scan times. In this thesis, the cyclic voltammetry measurements were all carried out from high potential to low potential with different scan rates and cycling times in an electrochemical workstation (CHI760E).

2.3.2.3 Electrochemical impedance spectroscopy (EIS)

Electrochemical impedance spectroscopy is used to study the change of electrochemical alternating current impedance with frequency while the electrochemical battery is in a balanced state (open state) or under some stable direct-current polarization conditions. Since EIS can record the impedance at different corresponding frequencies, various electrochemical process with different reaction time constant is able to be analyzed under a wide frequency range (μHz-MHz).

The commonly used display method of EIS in sodium ion batteries is called a complex impedance plot or Nyquist plot, which is drawn by using the real part of impedance as x-axis and the imaginary part as y-axis. A Nyquist EIS plot is composed of a semicircle at high frequency and inclined straight line at low frequency. The semicircle in high frequency is related to the contact resistance and charge transfer resistance of the battery, while the line in low frequency is related to the diffusion rate of sodium ions. In this thesis, we used an equivalent circuit diagram to calculate the resistance changes during the electrochemical process. As depicted in Figure 2-2, the equivalent circuit diagram is composed of the electrolyte resistance R_s, solid electrolyte interface resistance R_f, charge transfer resistance R_{ct} and so on. In addition, the constant element CPE1 and CPE2 in the equivalent circuit diagram correspond to the charge transfer resistance and interface resistance, respectively. The Warburg resistance is related to the diffusion rate of sodium ions.

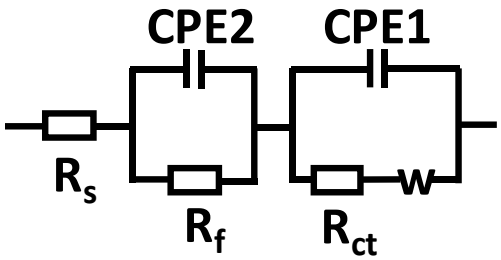

Figure 2-2 Equivalent circuit diagram for sodium ion batteries.

In this thesis, the EIS measurements were all carried out in an electrochemical working station (CHI760E) with different frequency ranges.

2.3.2.3 Galvanostatic intermittent titration technique

Galvanostatic intermittent titration technique was firstly put forward by W Weppner. The basic principle is to apply a constant current to the battery measurement system in a certain environment for a period of time, and then cut off the current to observe the change of the potential at the applied current segment system over time and the equilibrium voltage after relaxation. The relaxation information of electrode potential during the electrochemical process can be obtained by analyzing the change of electrode potential over time, and further can be used to speculate and calculate the reaction kinetics information.

Charge-discharge measurement is such a galvanostatic technique to study the electrochemical performance of materials. The measurement is used to investigate the charge-discharge properties of the electrode and practical specific capacity of active materials by carrying out the charge-discharge measurement under constant current conditions and recording the change of potential with time. In this thesis, all the charge-discharge measurements were carried out in a battery measurement system (Land-2001A). For the charge-discharge measurements of anode materials, the sodium-ion half cells were set to be discharged firstly with following charge process and cycled for different times under different current densities. The voltage range of half cells was from 0.01 V to 3 V.

The charge-discharge profiles, long-term cycling measurement and rate performance are all obtained by charge-discharge measurement. The charge-discharge profiles are drawn by using specific capacity as the x-axis and the voltage as y-axis to investigate the electrode status. From the charge-discharge profiles, the maximum discharge and charge specific capacity for a certain cycle can be obtained. The Columbic efficiency is calculated by discharge capacity divided by charge capacity in the same cycle, which confirms the electrode stability and reversibility of electrode materials.

Long-term cycling performance is to carry out the galvanostatic charge-discharge process for multiple cycles, which is drawn by using cycling times as x-axis and the specific capacity as y-axis. Obviously, longer cycling life is beneficial for the practical application of sodium ion batteries. The electrode stability could be judged by the capacity retention through comparing the specific capacity of different cycles.

Rate performance is to measure the discharge-discharge process of the same sodium ion batteries for multiple cycles under different current densities, which is drawn by using cycling times as x-axis and the specific capacity as y-axis. For an ideal electrode material, the lower decrease of capacity under different current densities illustrate the good electrode reversibility.

Chapter 3 Synthesis and application of TiO_2 nanopills derived from metal-organic framework for Na-ion battery

3.1. Introduction

In recent years, titanium dioxide has been widely applied in solar cells, lithium ion batteries, sodium ion batteries and other energy applications, due to its low toxicity, stability and abundance. [1, 2] When employed as the anode for the sodium ion batteries, TiO_2 possesses good reversibility and cycling stability. To date, TiO_2 with various morphologies have been prepared and applied as the anode for the sodium ion batteries. For instance, amorphous TiO_2 nanotubes can deliver a reversible specific capacity of 150 mAh g^{-1}. [3] In addition, anatase TiO_2 nanocrystals can retain a capacity of ~150 mAh g^{-1} after cycling 100 times.[4] These previous reports indicated that a high specific surface area would be beneficial to achieving a higher specific capacity and stability for the TiO_2 electrode materials. [5, 6]

On the other hand, researches about metal-organic frameworks (MOFs), as a new kind of controllable porous materials, have been developed quickly due to the large specific surface area and the functional characteristics of the MOFs. To date, over 20000 kinds of MOFs have been reported, as well as their applications in various fields such as gas storage, [7] catalysis, [8] adsorptive separation, [9] luminescent materials, [10] etc. Attributed to the unique porous structure, uncoordinated sites and functional organic linkers, MOFs have also been investigated as electrode materials for energy storage systems. [11-13] However, it has been reported that MOFs may not be a suitable electrode material for secondary batteries because of the possible occurrence of partial decomposition in the charge-discharge process. [14,15] In addition, it is found that the metal oxides prepared by using MOFs as versatile templates and precursors also possess high specific surface areas and porous structures, and were regarded as promising high-performance electrode materials for the secondary batteries. [16-19]

On the basis of these previous investigations, in the present work, we prepared MIL-125(Ti) (a kind of Ti-MOFs, metarial sofistitute Lavoisierframeworks) and further used it as a versatile template to prepare TiO_2 nanopills with a porous structure. Furthermore, the electrochemical

properties of the as-prepared porous TiO_2 as anode materials for sodium ion batteries were investigated for the first time. In addition, the relationship between intrinsic characteristics of this material and the storage capability of sodium ions was also discussed in this work.

3.2. Experimental section

3.2.1 Preparation of the MIL-125(Ti)

The MIL-125(Ti) precursor was prepared by a facile hydrothermal method. [20] 15 mL of N,N-dimethylmethanamide (DMF, Sinopharm, 99%) and 1.7 mL methanol (Sinopharm, 99%) were mixed in a beaker. Then 0.78 mL of titanium isoproproxide ($Ti(OiPr)_4$, Aldrich, 95%) and 1.3 g of 1,4-benzenedicarboxylic acid (Aldrich, 99%) were added into the mixed solution under magnetic stirring. After stirring for 1 h at room temperature, the mixed solution was transferred into a 50 mL Teflon stainless autoclave and heated at 150^{o}C for 24 h. After cooling down to room temperature, the obtained product was taken out and washed by DMF and methanol for several times. Then the obtained sample was dried at 60^{o}C overnight in an oven.

3.2.2 Preparation of the porous TiO_2 nanopills

The obtained MIL-125(Ti) precursor was sintered at 380 ^{o}C for 4 h with a heating rate of 5 ^{o}C/min. to obtain the porous TiO_2 in the form of white powder.

3.2.3 Characterization and electrochemical measurements

The testing conditions for physical characterization were shown in Chapter 2.

The obtained TiO_2 nanopills, acetylene black and PVDF were mixed in a mass ratio of 7:2:1. By using NMP as a solvent, the mixed slurry was coated onto the Cu foil and dried at 110^{o}C for 12 h. The mass loading to each disc was about 2 mg cm^{-2}. The obtained TiO_2 electrode was employed as the negative electrode. The half-cells were assembled in a glove box using sodium metal as the counter electrode and 1M $NaClO_4$ in the PC and EC mixed solvent as the electrolyte. The MIL-125(Ti) precursor electrode was also prepared by the same method.

The Cyclic Voltammetry was carried out in a voltage range of 0.01-3 V. Electrochemical impedance spectroscopy was measured from 0.01 mHz to 100 kHz. The cycling performance and charge-discharge profiles were carried out in a Land CT2001A battery tester device from 0.01 to 3 V.

3.3 Results and discussion

3.3.1 XRD analysis

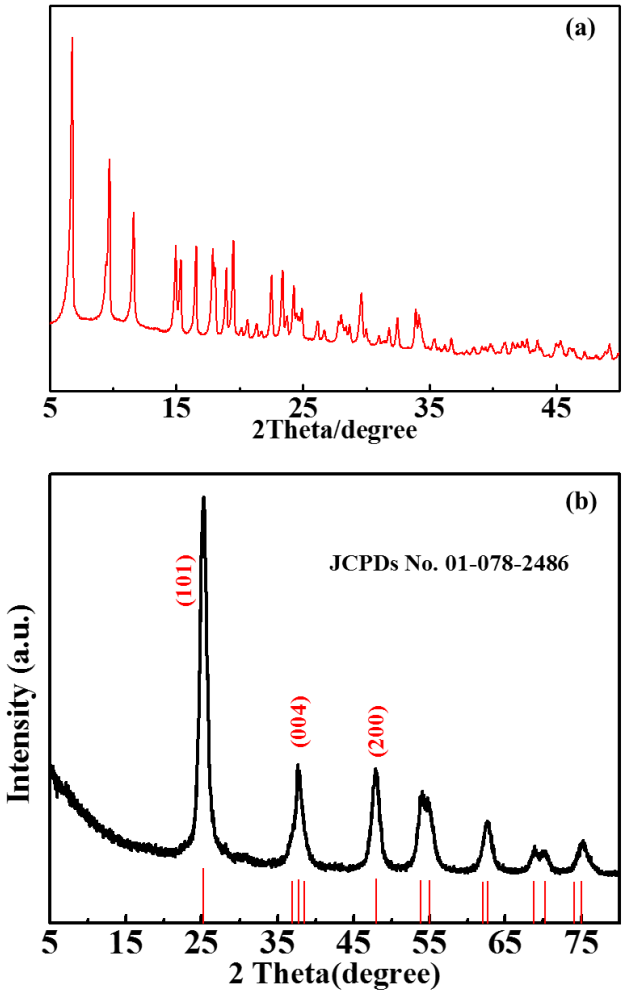

Figure 3-1 XRD patterns for as-prepared (a) MIL-125(Ti) and (b) hierarchically porous TiO_2.

The XRD patterns for as-prepared precursor and final product were shown in Figure 3-1. The XRD pattern for the precursor was in good agreement with the previous reports about MIL-125(Ti). [20] However, the sharp and strong peaks in Figure 3-1a indicated the large size of the as-prepared precursor. The peaks of the obtained TiO_2 in Figure 3-2a could all be indexed to the standard card of the anatase TiO_2 (JCPDs No. 01-078-2486) with no peak from MIL-125(Ti),

indicating all final product had been converted to the anatase TiO_2 after calcined. In addition, The major diffraction peaks at 8.781°, 24.166°, 28.467° and 48.357° could be indexed to (002), (400), (403) and (020) planes of the TiO_2, respectively.

3.3.2 SEM and TEM analysis

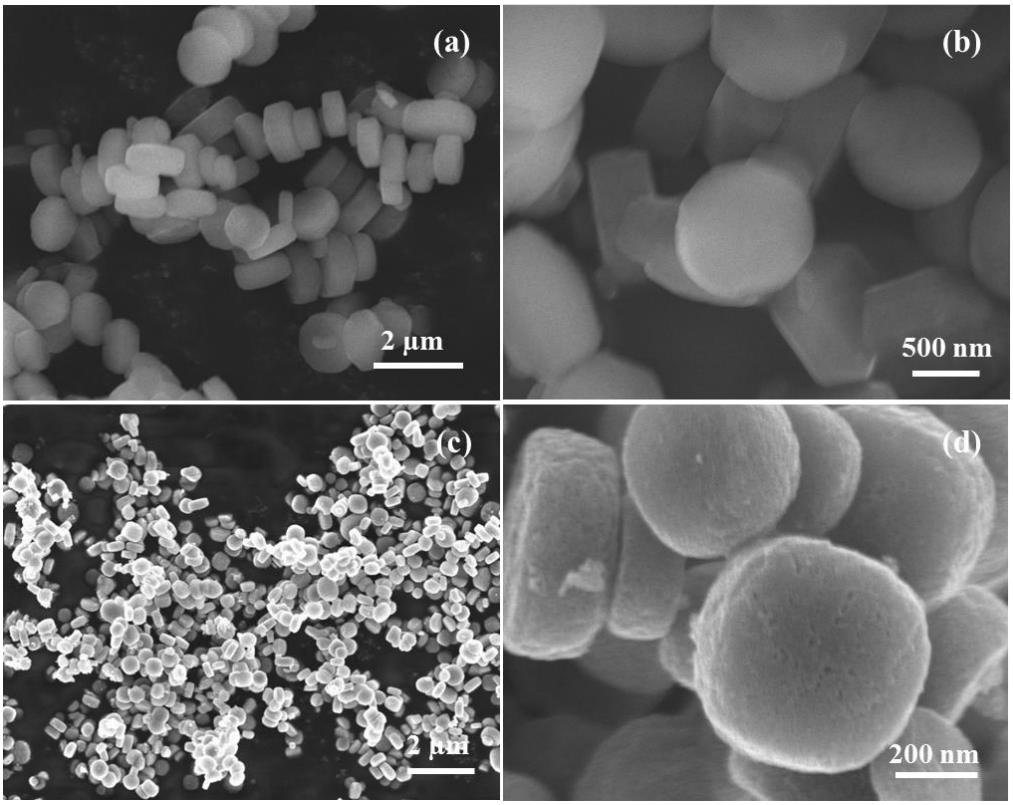

Figure 3-2 SEM images of MIL-125(Ti) precursor (a-b) and the hierarchically porous TiO_2 (c-d) derived from MIL-125(Ti).

Figure 3-2 shows the SEM images of the MIL-125(Ti) precursor and the as-prepared TiO_2. As displayed in Figure 3-2a and 2b, the MIL-125(Ti) possess a uniform morphology of pills with a diameter of ~1 μm. It can be observed from Figure 3-2c and 2d that the obtained TiO_2 after calcined remained the structure of pills, while the pills turned to be porous and composed of nanoparticles. Meanwhile, the diameter of the obtained TiO_2 nanopills was decreased to ca. 0.5~0.7 μm which might be attributed to the loss of H and C atoms during the calcination process.

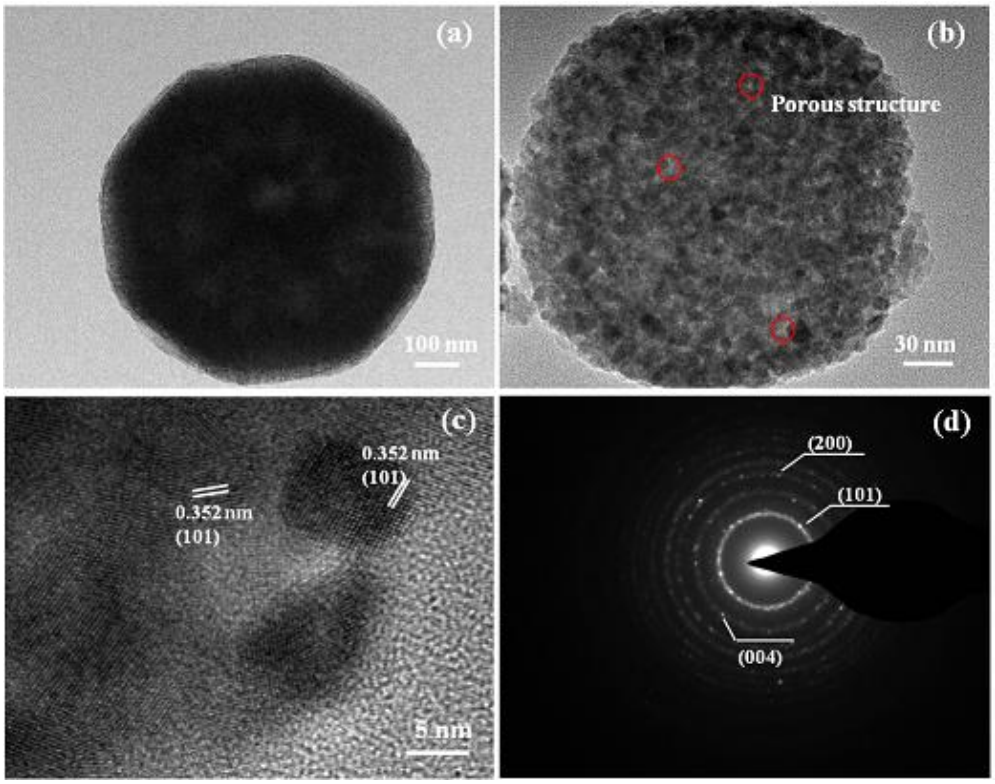

Figure 3-3 (a) TEM image of MIL-125(Ti) precursor, (b TEM image, (c) HRTEM image and (d) SAED pattern of the hierarchically porous TiO_2 derived from MIL-125(Ti).

In order to further investigate the microstructure of the MIL-125(Ti) precursor and the as-prepared TiO_2, TEM and SAED measurements were carried out. It can be seen in Figure 3-3a, the MIL-125(Ti) showed a bulk structure with a diameter of ~1 μm. As depicted in Figure 3-3a, the obtained TiO_2 derived from MIL-125(Ti) exhibited a hierarchical structure. The basic morphology of nanopills remained for the obtained TiO_2, while the nanopills displayed a porous structure and was composed of nanoparticles smaller than 10 nm. Figure 3-3c shows the HRTEM image of the hierarchical TiO_2 nanopills. Small nanoparticles with a particle size of ca. 7 nm could be observed. Moreover, a lattice fringe of 0.356 nm could also be observed from Figure 3-3c, corresponding to the (101) plane of the anatase TiO_2. In addition, the SAED pattern for the TiO_2 nanopills in Figure 3-3d displayed multiple diffraction rings which could be indexed

to some typical crystal planes of TiO_2, indicating the TiO_2 nanopill is multiple single crystals or polycrystalline.

3.3.3 Particle size distribution analysis

Figure 3-4 shows the particle size distribution of the MIL-125(Ti) and the TiO_2 nanopills. The particle size of the MIL-125(Ti) ranged from 0.88 μm to 1.52 μm, and delivered an average size of 1.18 μm. However, it is clear that the TiO_2 nanopills derived from the MIL-125(Ti) have decreased to an average particle size of 520 nm, as displayed in Figure 3-4b. In addition, the particle size of the TiO_2 nanopills ranged from 400 to 600 nm, in agreement with the obtained SEM results.

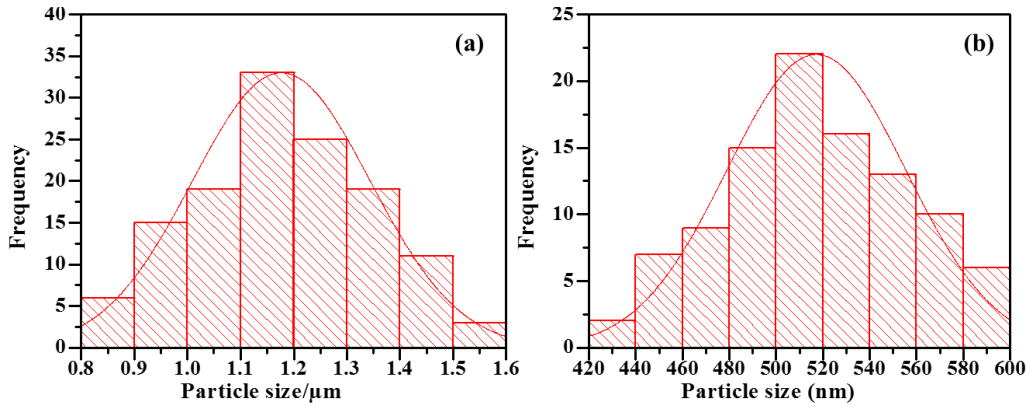

Figure 3-4 Size distributions of the as-prepared (a) MIL-125(Ti) and (b) hierarchically porous TiO_2.

3.3.4 BET analysis

In order to confirm the specific surface area and the pore size distribution of the MIL-125(Ti) and the porous TiO_2 nanopills, nitrogen adsorption-desorption isotherm characterization was carried out. As depicted in Figure 3-5a and Figure 3-6, the specific surface area of the MIL-125(Ti) precursor and the TiO_2 nanopills were proved to be 1167 and 102 m^2 g^{-1}, respectively. The high specific surface area of the TiO_2 nanopills could be attributed to the porous structure derived from the MIL-125(Ti) precursor, which is larger than most previous reported TiO_2. In addition, as displayed from the pore distribution results in Figure 3-5b, the porous TiO_2 nanopills possessed an average pore size of ~11 nm, which was consistent with the TEM results and

illustrating the existence of the mesopores. The large specific surface area and the mesoporous structure would be no doubt beneficial to the fast diffusion of the sodium ions and the electrolyte.

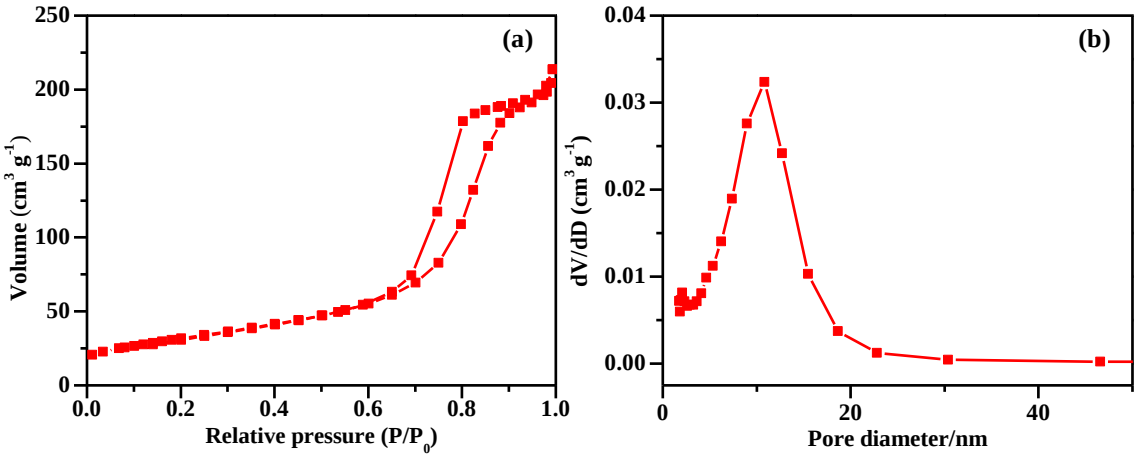

Figure 3-5 (a) N_2 adsorption-desorption isotherms and (b) pore size distributions from the adsorption branch through the BJH method of the hierarchically porous TiO_2 nanopills.

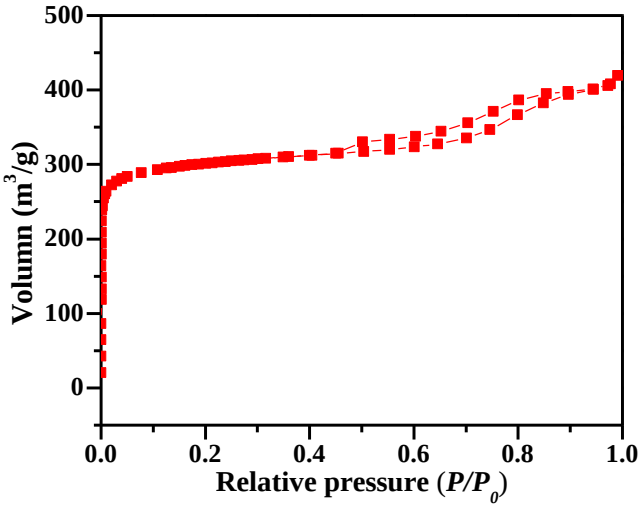

Figure 3-6 N_2 adsorption-desorption isotherms of MIL-125(Ti) precursors.

3.3.5 Electrochemical performance

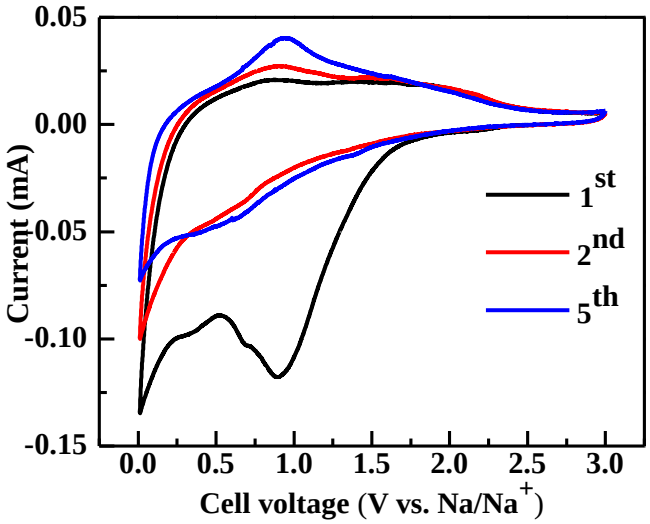

Figure 3-7 CV curves of the porous TiO_2 electrode for the 1st, 2nd and 5th cycles at a scan rate of 0.5mV s^{-1}.

The electrochemical performance of both the as-prepared MIL-125(Ti) and the porous TiO_2 nanopills were measured as the anode for the sodium-ion batteries. Figure 3-7 shows the CV curves of the porous TiO_2 nanopills for the 1st, 2nd and 5th cycles at a scan rate of 0.5 mV s^{-1}. In the 1st cycle, a reduction peak at 0.87 V could be clearly observed. However, the reduction peak disappeared in the following cycles, which might be attributed to the formation of a solid electrolyte interphase (SEI) layer and the decomposition of electrolyte in the initial cycle. [21-23] In the subsequent cycles, it could be observed that a pair of reduction peak and oxidation peak appeared at 0.5 V and 0.75 V, respectively, corresponding to the reversible reduction of Ti^{4+}/Ti^{3+}. Moreover, after 5 cycles both the reduction and oxidation peaks overlapped well with the 2nd cycle, illustrating the good reversibility of the insertion/desertion process of sodium ions into the TiO_2 electrode.

Figure 3-8 displays the charge-discharge profiles of the porous TiO_2 nanopills for the 1st, 2nd and 5th cycles at a current density of 0.1 A g^{-1}. For the 1st cycle, a high discharge capacity of 516.2 mAh g^{-1} could be achieved, while the charge capacity was only ~196 mAh g^{-1}. The low Columbic efficiency of the 1st cycle corresponded to the CV results, attributing to the formation

of the SEI film. In the 2nd and 50th cycle, a discharge capacity of 196.4 and 164.3 mAh g^{-1} could be obtained, respectively, indicating the excellent structural stability of the porous TiO_2 nanopills electrode.

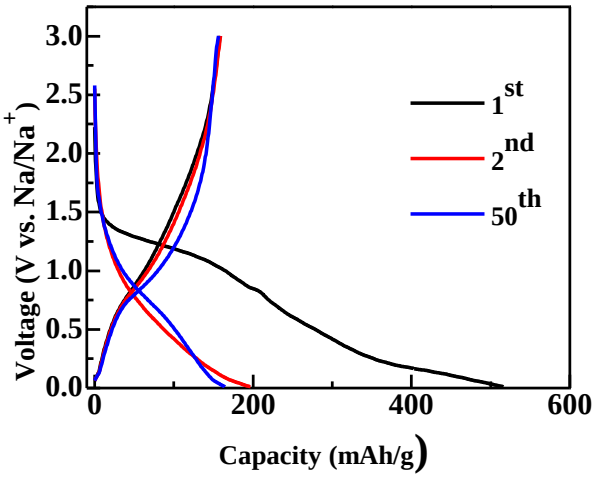

Figure 3-8 Charge-discharge profiles of the porous TiO_2 nanopills electrode for the 1st, 2nd and 50th cycles at a current density of 0.1 A g^{-1}.

Figure 3-9 shows the long cycling performance of the hierarchically porous TiO_2 electrode at a relatively low current density of 0.1 A g^{-1}. Even after 400 cycles, the hierarchically TiO_2 nanopills electrode exhibited a specific capacity of ~130 mAh g^{-1} and a capacity retention of 65% compared with the 2nd cycle, indicating the good stability under low current density.

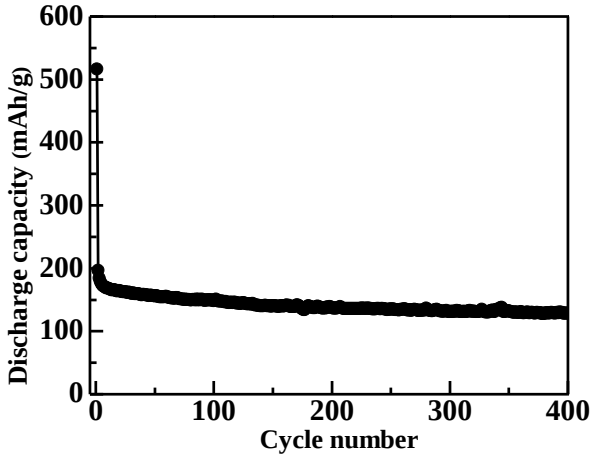

Figure 3-9 Cycling performance of the hierarchically porous TiO_2 electrode at a current density of 0.1 A g^{-1}.

The long cycling performance at a high current density of 0.5 A g^{-1} was shown in Figure 3-10. Before cycling in such a high current density, the half-cell was firstly cycled under a low current density of 0.05 A g^{-1} for 3 times for the purpose of electrode activation. After the activation process, a discharge capacity of 112 mAh g^{-1} could be achieved for the 1st cycle at the current rate of 0.5 A g^{-1}. Even after cycling for 3000 times, the porous TiO_2 nanopills electrode could still exhibit a high specific capacity of 100 mAh g^{-1}. Thus, a high capacity retention of 90% could be remained for 3000 cycles, which illustrated the excellent electrode stability and a long cycling life of the porous TiO_2 nanopills electrode. It is worth noting that the capacity retention is higher than most previous literature.

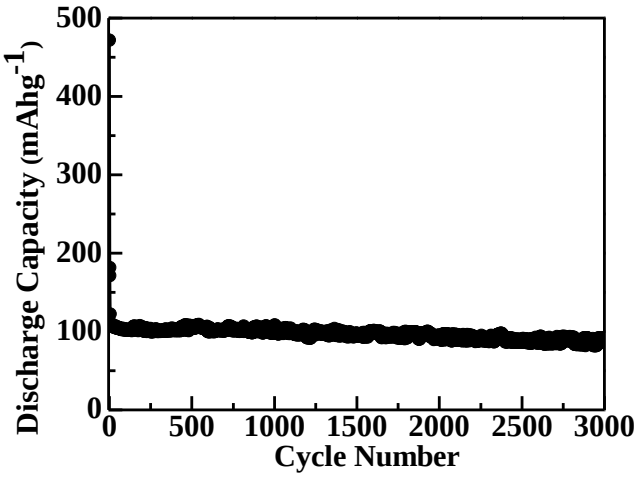

Figure 3-10 Cycling performance of the hierarchically porous TiO_2 electrode at a current density of 0.5 A g^{-1}.

Furthermore, the rate performance of the porous TiO_2 nanopills electrode was carried out from 0.05 to 0.5 A g^{-1}. As shown in Figure 3-11, the porous TiO_2 nanopills electrode exhibited good cycling stability in different current rates. After cycling for 10 times at 0.05 A g^{-1}, a high discharge capacity of 170 mAh g^{-1} could be obtained. When the current density was increased to 0.1, 0.2 and 0.5 A g^{-1}, the specific capacity remained at 160, 145, 110 mAh g^{-1}, respectively. After cycling under different current rates for 25 cycles, the porous TiO_2 nanopills electrode

could still exhibit a discharge capacity of ~145 mAh g^{-1} when the current density returned to 0.2 A g^{-1}. Furthermore, when the current rate returned to 0.1 A g^{-1}, a high discharge capacity of 160 mAh g^{-1} could still be obtained, which was the same as the 15-20 cycles at the same current rate. In addition, the porous TiO_2 nanopills electrode was measured continually under 0.1 A g^{-1} until 100 cycles, and the capacity retention as high as 94% could be kept, indicating the good reversibility of this material.

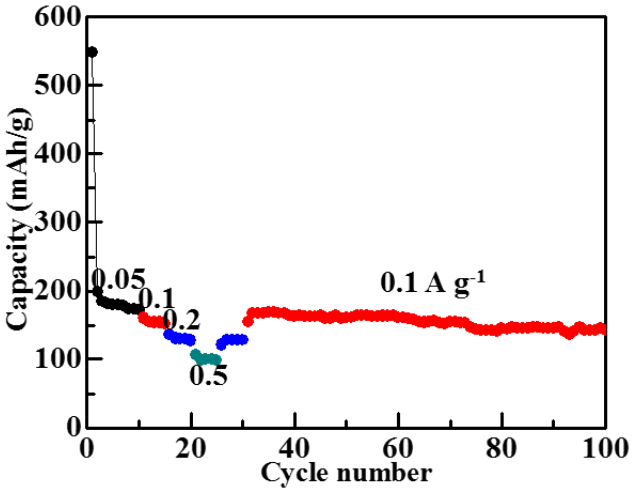

Figure 3-11 Rate performance of the hierarchically porous TiO_2 electrode from 0.05 to 0.5 A g^{-1}.

In order to investigate the structure of the electrochemical system and the property of the electrochemical process, the electrochemical impedance of the hierarchically porous TiO_2 electrode without cycling and with cycling for 2000 times was measured. It could be observed that the radius of the semicircle in the high-frequency area after cycling was a little smaller than the semicircle without cycling, illustrating the decreased charge-transfer resistance. As calculated from the equivalent circuit model, the electrolyte resistance R_s increased slightly from 3.22 Ω to 3.784 Ω, while the charge-transfer resistance R_{ct} decreased from 31.27 Ω to 16.54 Ω. The decrease of the charge-transfer resistance could be attributed to the occurrence of the reduction process for the nanocomposite into the corresponding metals during the irreversible reactions, which occurred as well in other similar metal oxide electrode materials. [24, 25]

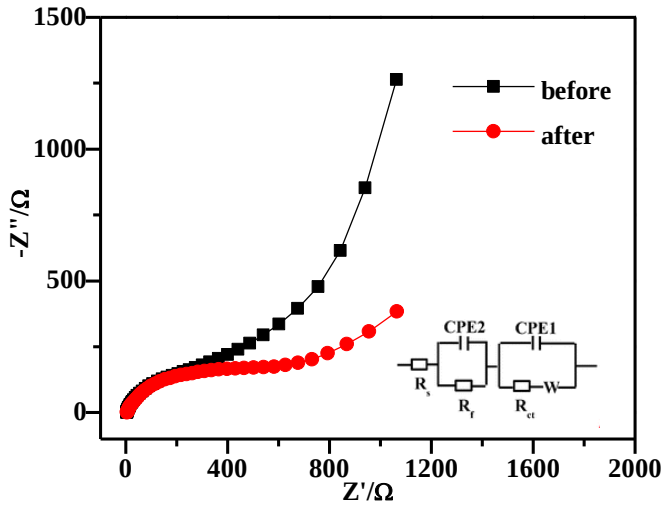

Figure 3-12 EIS plots of the hierarchically porous TiO_2 electrode without cycling and with cycling for 2000 times.

Table 1 Impedance parameters calculated from an equivalent circuit model.

Samples	$R_s(\Omega)$	$R_{ct}(\Omega)$
Before	3.22	31.27
After	3.784	16.54

According to the large specific surface area of MIL-125 (Ti), we also investigated the electrochemical performance of MIL-125 (Ti) in the sodium-ion batteries. Figure 3-13 displays the charge-discharge profiles of the MIL-125(Ti) electrode for the 1st, 2nd and 10th cycles at a current density of 0.05 A g^{-1}. Attributed to the large specific surface area of MIL-125(Ti), an initial discharge capacity of 775 mAh g^{-1}could be achieved. However, the discharge capacity faded to only 71.6 mA h g^{-1} after cycling for 10 times while in the 2nd cycle the discharge capacity was 115.9 mA h g^{-1}. The rapid decay of the specific capacity demonstrated the MIL-125(Ti) was not a suitable electrode material for the sodium-ion batteries, due to the possible occurrence of decomposition during the cycling process.

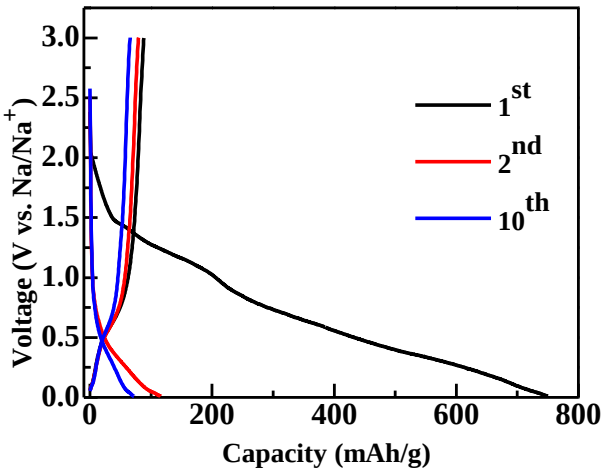

Figure 3-13 Charge-discharge profiles of MIL-125(Ti) electrode for the 1st, 2nd and 10th cycles at a current density of 0.05 A g^{-1}.

The porous TiO_2 nanopills electrode exhibited a good specific capacity and an excellent stability when used as the anode material for the sodium ion batteries, which could benefit from the intrinsic characteristics of the as-prepared TiO_2 nanopills. First of all, the porous TiO_2 nanopills derived from the MIL-125(Ti) possess the framework structure, which was beneficial to the full diffusion of the electrolyte. In addition, the mesopores in each nanopill can promote the wettability between the electrode and the electrolyte, and can increase the adsorption sites for the sodium ions by generating exreinsic defects. In addition, the large specific surface area can be advantageous for increasing the contact between the active materials and the electrolyte, and further enhance the storage capabilities of the sodium ions. Therefore, the as-prepared porous TiO_2 nanopills can achieve such an excellent electrochemical performance in the sodium-ion batteries.

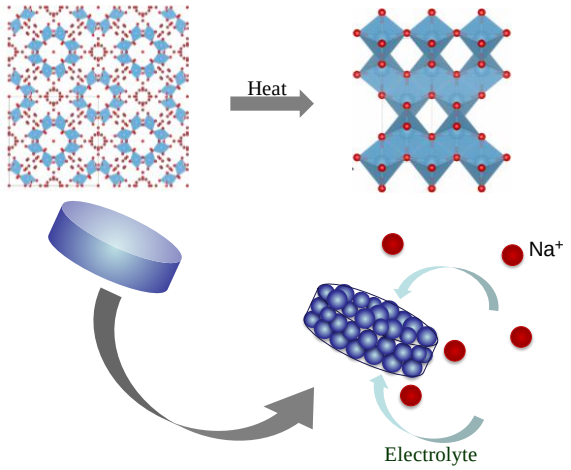

Figure 3-14 The diffusion and insertion/desertion process of sodium ions in the hierarchical porous TiO_2 nanopills.

3.4 Conclusions

In this work, the porous TiO_2 nanopills were prepared successfully by using the MIL-125(Ti) as precursor via a facile hydrothermal method. Furthermore, when employed as the anode for the sodium-ion batteries for the first time, the porous TiO_2 nanopills can achieve a relatively high and reversible specific capacity as well as an excellent electrochemical stability. High discharge capacities of 196.4 and 115.9 mAh g^{-1} can be obtained at 0.1 A g^{-1} and 0.5 A g^{-1}, respectively. In addition, even after 3000 cycles at a high current density of 0.5 A g^{-1}, a reversible capacity of 100 mAh g^{-1} can be remain with a high capacity retention of 90%. Thus, it was proved that the as-prepared porous TiO_2 nanopills can be a promising anode material for high performance sodium ion batteries. In addition, the preparation method of electrode materials using MOFs as templates and precursor also provide a developing study direction for preparing high performance secondary batteries.

References

[1] Hong Z, Wei M, Lan T, et al, Additive-free synthesis of unique TiO_2 mesocrystals with enhanced lithium-ion intercalation properties. ***Energy Environ. Sci.***, 2012, 5(1): 5408-5413.

[2] Hong Z, Wei M. Layered titanate nanostructures and their derivatives as negative electrode materials for lithium-ion batteries. ***J. Mater. Chem. A***, 2013, 1, 4403–4414.

[3] Xiong H, Slater M D, Balasubramanian M, et al. Amorphous TiO_2 nanotube anode for rechargeable sodium ion batteries. ***J. Phys. Chem. Lett.***, 2011, 2(20), 2560-2565.

[4] Xu Y, Lotfabad E M, Wang H, et al. Nanocrystalline anatase TiO_2: a new anode material for rechargeable sodium ion batteries. ***Chem. Commun.***, 2013, 49(79), 8973-8975.

[5] Kim K, Ali G, Chung K Y, et al. Anatase titania nanorods as an intercalation anode material for rechargeable sodium batteries. ***Nano Lett.*** 2014, **14,** 416-422.

[6] Huang J P, Yuan D D, Zhang H Z, et al. Electrochemical sodium storage of TiO_2 (B) nanotubes for sodium ion batteries. ***RSC Advances***, 2013, **3,** 12593.

[7] Makal T A, Li J -R, Lu W, et al. Methane storage in advanced porous materials. ***Chem. Soc. Rev.***, 2012, **41,** 7761–7779.

[8] Zou R Q, Sakurai H, Han S, et al. Probing the Lewis acid sites and CO catalytic oxidation activity of the porous metal− organic polymer [Cu (5-methylisophthalate)]. ***J. Am. Chem. Soc.***, 2007, **129,** 8402–8403.

[9] Dawson R, St¨ockel E, Holst J R, et al. Microporous organic polymers for carbon dioxide capture. ***Energy Environ. Sci.***, 2011, **4,** 4239–4245.

[10] Chen L, Tan K, Lan Y Q, et al. Unusual microporous polycatenane-like metal–organic frameworks for the luminescent sensing of Ln^{3+} cations and rapid adsorption of iodine. ***Chem. Commun.***, 2012, 4**8,** 5919–5921.

[11] Morozan A and Jaouen F. Metal organic frameworks for electrochemical applications. ***Energy Environ. Sci.***, 2012, **5,** 9269–9290.

[12] Cheng C Y, Fu S J, Yang C J, et al. NCHU-3: a crystalline inorganic-organic hybrid molecular sieve with extra-large cages. ***Angew. Chem. Int. Ed.***, 2003, **42,** 1937–1940.

[13] Huang L W, Yang C J, Lin K J. Toward the design and synthesis of lithium-ion intercalation into a coordination π -π framework host. ***Chem. Eur. J.***, 2002, **8,** 396–400.

[14] Li X, Cheng F, Zhang S et al. Shape-controlled synthesis and lithium-storage study of metal-organic frameworks Zn_4O(1, 3, 5-benzenetribenzoate)$_2$. ***J. Power Sources***, 2006, **160,** 542–547.

[15] F´erey G, Millange F, Morcrette M, et al. Greneche and J. M. Tarascon. Mixed-valence Li/Fe-based metal-organic frameworks with both reversible redox and sorption properties. ***Angew. Chem. Int. Ed.***, 2007, **46,** 3259–3263.

[16] Xu X, Cao R, Jeong S, et al. Spindle-like mesoporous α-Fe_2O_3 anode material prepared from MOF template for high-rate lithium batteries. ***Nano Lett.***, 2012, **12(9),** 4988-4991.

[17] Ge X, Li Z Q, C. W X et al. Metal–organic frameworks derived porous core/shell structured ZnO/$ZnCo_2O_4$/C hybrids as anodes for high-performance lithium-ion battery. ***ACS Appl. Mater. Interfaces***, 2015, **7 (48),** 26633–26642.

[18] Xiu Z, Alfaruqi M H, Gim J, et al. Hierarchical porous anatase TiO_2 derived from a titanium metal–organic framework as a superior anode material for lithium ion batteries. ***Chem. Commun.***, 2015, **51,** 12274-12277.

[19] Wang P, Lang J W, Liu D X, et al. TiO_2 embedded in carbon submicron-tablets: synthesis from a metal–organic framework precursor and application as a superior anode in lithium-ion batteries. ***Chem. Commun.***, 2015, **51,** 11370-11373.

[20] Fu Y, Sun D, Chen Y, et al. An amine-functionalized titanium metal-organic framework photocatalyst with visible-light-induced activity for CO_2 reduction. ***Angew. Chem.***, 2012, **51,** 3364-3367.

[21] Guo Y G, Hu J S, Wan L J. Nanostructured materials for electrochemical energy conversion and storage devices. ***Adv. Mater.***, 2008, **20,** 2878-2887.

[22] Yang X, Wang C, Yang Y, et al. Anatase TiO_2 nanocubes for fast and durable sodium ion battery anodes. ***J. Mater. Chem. A***, 2015, **3,** 8800-8807.

[23] Wu L, Bresser D, Buchholz D, et al. Unfolding the mechanism of sodium insertion in anatase TiO_2 nanoparticles. ***Adv. Energy Mater.***, 2015, **5,** 1401142.

[24] Luo J, Liu J, Zeng Z, et al. Three-dimensional graphene foam supported Fe_3O_4 lithium battery anodes with long cycle life and high rate capability. ***Nano Lett.***, 2013, **13(12),** 6136-6143.

[25] Lu F, Chen Q, Wang Y, et al. Flexible additive-free CC@ TiO_x N_y@SnS_2 nanocomposites with excellent stability and superior rate capability for lithium-ion batteries. ***RSC Advances***, 2016, **6(29),** 24366-24372.

Chapter 4 Synthesis and application of a feather-like MnO_2 on carbon paper for sodium-ion battery

4.1 Introduction

In recent years, transition metal oxides, such as Fe_3O_4, [1,2] CuO, [3,4]TiO_2, [5-8] and $NiCo_2O_4$ [9,10], have been widely investigated as the electrode materials for lithium ion batteries and sodium ion batteries. Among them, manganese dioxide has attracted a great attention due to low cost, the low toxicity, and the superior safety.[11-13] To date, manganese dioxides have been widely employed in various fields, such as lithium ion batteries, [14-16] metal-air batteries, [17] supercapacitors, [18] biosensors, [19] etc. As reported in the lithium ion batteries, manganese dioxides exhibited a high discharge capacity and a relatively low electrochemical motivation force compared with other transition metal oxides. [20,21] The theoretical specific capacity of the manganese dioxide was calculated to be as high as ~1230 mAh g^{-1} for the rechargeable batteries. However, the high specific capacity faded quickly during the cycling process, which may be due to the low electronic conductivity, the aggregation and the volume expansion after cycling. [20] As a solution, some researchers found that the cycling performance of the MnO_2 can be improved by compositing with other materials such as carbonaceous materials and other metal oxides. It was reported that by compositing with carbonaceous materials the electron transfer in the MnO_2 electrode could be enhanced. For instance, by compositing MnO_2 nanoflakes with carbon nanotubes (CNT) the initial capacity was enhanced from 168 to 254 mAh g^{-1} with a cycling stability of 200 cycles. [22] A reversible specific capacity of 890 mAh g^{-1} could be remained for the MnO_2/graphene nanoribbon composite after 180 cycles. [21]

In addition, the additional binders are mostly electrochemical inactive in the traditional slurry paste electrode, which leads to the decrease of the electrical conductivity. To remove the influence of the binders, various binder-free electrodes have been prepared and directly used in various ESSs like fuel cells, [23,24] supercapacitors, [25,26] lithium ion batteries and sodium ion batteries. [27-29] To date, many researchers have reported the preparation of the binder-free electrodes using different substrates in sodium ion batteries, such as graphene substrates, carbon

cloth, metal substrates, etc. Apart from these substrates, carbon paper, which is porous, hydrophilic, and conductive, has not been applied in sodium ion batteries yet.

In the present work, we prepared in-situ grown feather-like MnO_2 on the carbon paper via a simple hydrothermal method. The formation process of this unique structure was proposed by investigating the intermediate products during the reaction. Then the MnO_2/carbon paper was directly used as the anode for sodium ion batteries for the first time. Furthermore, the relationship between the structure and other intrinsic characteristics of the MnO_2/carbon paper and the Na^+ storage capability was investigated as well in this work.

4.2. Experimental section

4.2.1 Synthesis of the feather-like MnO_2 on carbon paper

The feather-like MnO_2 on carbon paper was prepared via a simple and facile hydrothermal method. Firstly, the carbon paper was cut into rectangular pieces with a size of 5×2 cm and then washed by sonicating in deionized water, ethanol and acetone for 30 min, respectively. Then 0.03 g $KMnO_4$ was dissolved into 40 mL deionized water in a flask under stirring at room temperature. After stirred for 30 min, the obtained solution and washed carbon paper were transferred into a 50 mL Teflon stainless autoclave and reacted for 24 h at 160 ^oC. The obtained carbon paper was taken out and washed with ethanol and deionized water for several times, respectively. Finally, the carbon paper was dried at 70 ^oC in an oven.

4.2.2 Characterization and electrochemical measurements

The testing condition for XRD, SEM, TEM and XPS measurements are shown in Chapter 2.

The obtained carbon paper after the reaction was cut into uniformly round sheets with an average loading mass of 2 mg cm^{-2} on each sheet. Using Na metal as the reference and the counter electrode, the carbon paper sheets were directly used as the anode for sodium ion batteries to assemble half-cells in a glove box filled with Argon atmosphere. After standing for 24 h, the batteries were tested in a Land CT2001A battery tester device at a voltage range of 0.01 to 3 V. The Cyclic Voltammetry was carried out in a voltage range of 0.01-3 V. Electrochemical impedance spectroscopy was measured from 0.01 mHz to 100 kHz.

4.3 Results and discussion

In a typical crystal structure of the α-MnO_2, MnO_6 octahedrons connect by corner-sharing and edge-sharing along the c-axis to form a tunnel structure of 2 × 2, and then these unit cells are further connected by edge-sharing, as depicted in Figure 4-1.

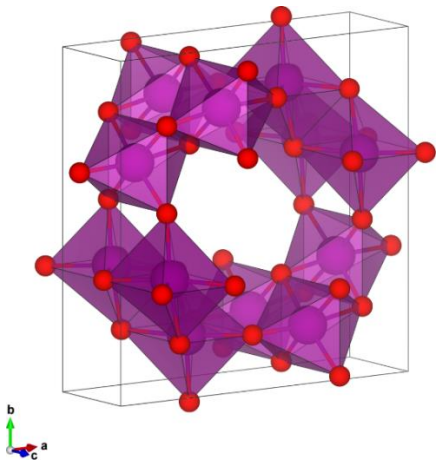

Figure 4-1 Crystal structure of α-MnO_2. Large (purple) octahedral represent approximate MnO_6 octahedral while Small (red) spheres represent oxygen.

The lattice parameters were optimized by the PBE+*U* method and listed in Table I. It is noted that the optimized variables are in good agreement with the experimental results. In order to study the electronic properties of the *α*-MnO_2, the partial density of states (PDOS) was calculated with respect to the optimized crystal structure showed in Figure 4-1. It is clear that the *α*-MnO_2 possesses a semiconductor characteristic. In the spin-up channel, the upper valence bands consist mainly of the O 2*p* and Mn t_{2g} states, while the lower conduction bands are composed of the hybridization of Mn 3*d* and O 2*p* states. In the spin-down channel, a much larger band gap was observed near the Fermi energy level. In this case, the upper valence bands predominantly consist of the occupied O 2*p* states, and the lower conduction bands are formed by the unoccupied Mn 3*d* states. In the *α*-MnO_2, the Mn usually shows the 4^+ valence with the electronic configuration of $3t_{2g}^3e_g^0$. However, the e_g state of Mn can also be found at the valence bands owing to the localization of the 3d electrons. When Na ions inserted into the *α*-MnO_2 lattice, the additional electrons would cause the increase of the Fermi energy level. Consequentially, the hybridization of Mn 3*d* and O 2*p* states would cross the Fermi energy level

in the spin-up channel of the α-$Na_{0.125}MnO_2$, resulting in the electronic conductivity. The charge redistribution caused by the Na ion intercalation can be precisely described by calculating the differential charge density, which is shown in Figure 4-2. We can see that the inserted Na ions donate charges simultaneously to the neighboring O anions and the Mn cations. The positions of the differential charges indicate that the additional electrons relocated to the O 2*p* and Mn 3*d* states, which agrees well with the PDOS results.

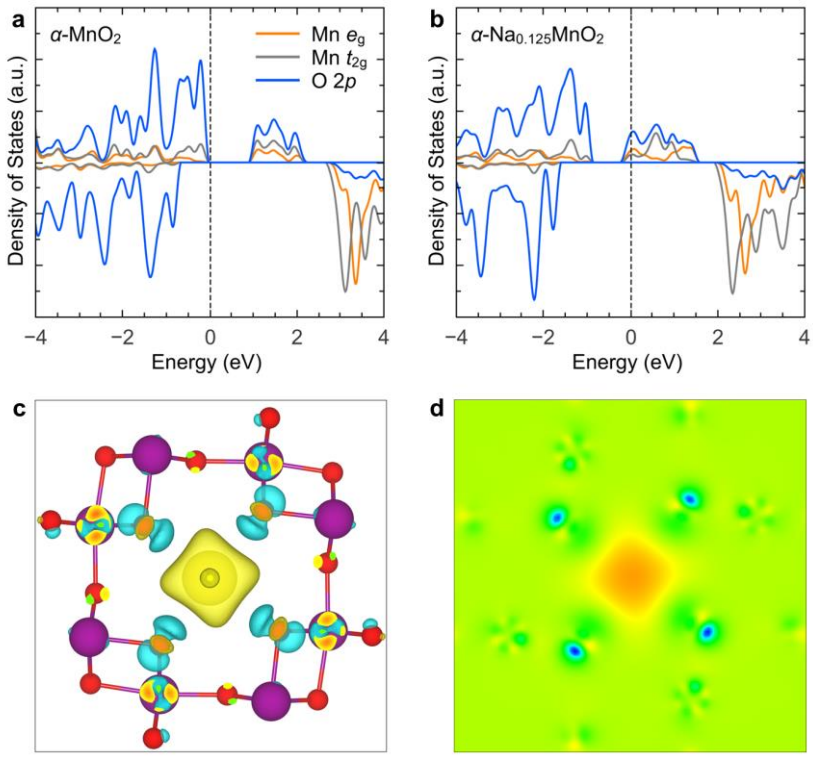

Figure 4-2 Calculated PDOS for the α-MnO_2 (a) and α-$Na_{0.125}MnO_2$ (b) by PBE+U method. The differential charge density of the Na intercalation in the α-MnO_2 (c) and a slice along the (001) plane (d).

Table 1. Optimized and experimental lattice parameters for α-MnO_2.

	a(Å)	b(Å)	c(Å)	α, β, γ (deg)
PBE+U	9.732	9.732	2.928	90
Expt.	9.750	9.750	2.861	90

4.3.1 XRD analysis

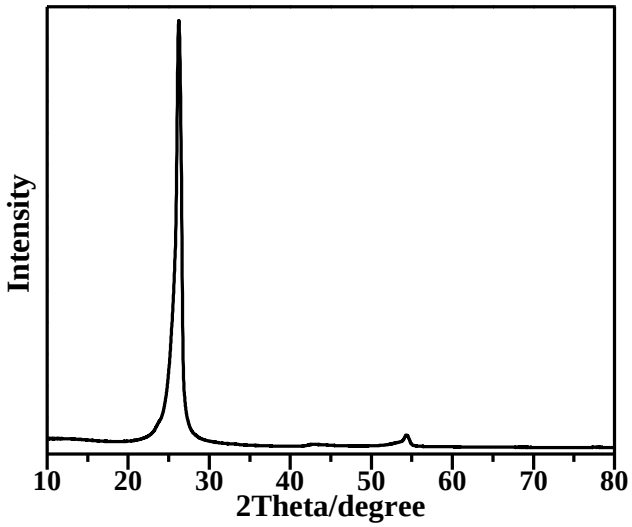

Figure 4-3 XRD pattern of the pure carbon paper.

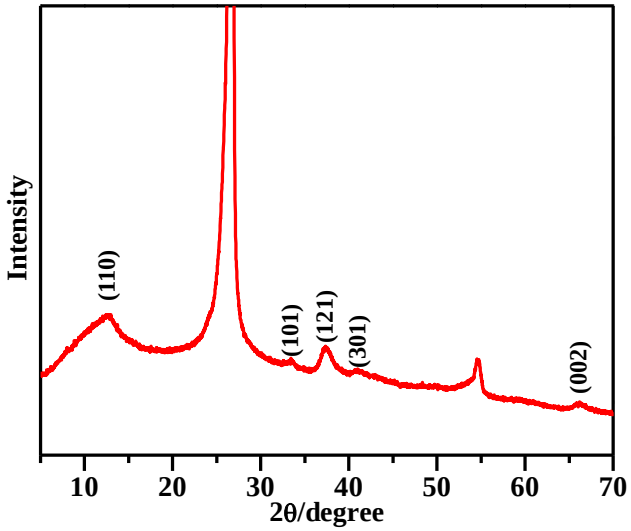

Figure 4-4 XRD pattern for the feather-like MnO_2 on carbon paper.

Figure 4-3 and 4-4 show the XRD patterns of the carbon paper and the as-prepared sample on carbon paper, respectively. All the diffraction peaks could be assigned to the standard PDF card of the α-MnO_2 (PDF card No. 01-072-1982) except for two peaks of the carbon paper. In

addition, the peaks at 12.745°, 32.726°, 37.628°, 42.036°, 65.521° can be assigned to the (110), (101), (121), (301), (002) crystal planes of the α-MnO_2.

4.3.2 XPS spectra analysis

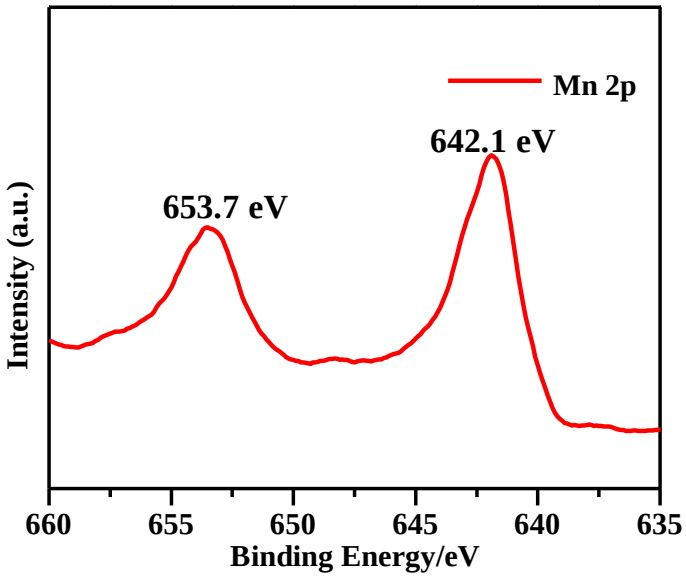

Figure 4-5 XPS spectra for Mn2p of the feather-like MnO_2 on CP.

XPS spectra were obtained to confirm the valance state of the Mn element for the MnO_2 on the carbon paper, as depicted in Figure 4-5. Two peaks which could be assigned to Mn 2p3/2 and Mn 2p1/2 appear at 642.1 and 653.7 eV, respectively. The binding energy of these peaks is consistent with other reports about the MnO_2, indicating the existence of Mn^{4+} in the as-prepared products. [30, 31] Therefore, it can further prove that MnO_2 was successfully grown on the surface of the carbon paper.

4.3.3 FE-SEM and TEM analysis

Figure 4-6a displays the SEM image of the unreacted carbon paper. As shown in Figure 4-6a, the carbon paper is composed of many carbon microfibers to form a three-dimensional porous structure. It can also be observed that the unreacted microfibers possess a relatively smooth surface. After the reaction process, the surface of the carbon microfibers changed obviously. As displayed in Figure 4-6b, the as-prepared feather-like MnO_2 distributed uniformly on the surface

of each carbon microfibers. Each feather was composed of an ultralong nanowire with a length of over 2 μm as the rachis and many ultrasmall nanowires grown around the rachis as barbs with an average diameter of ca. 10-15 nm.

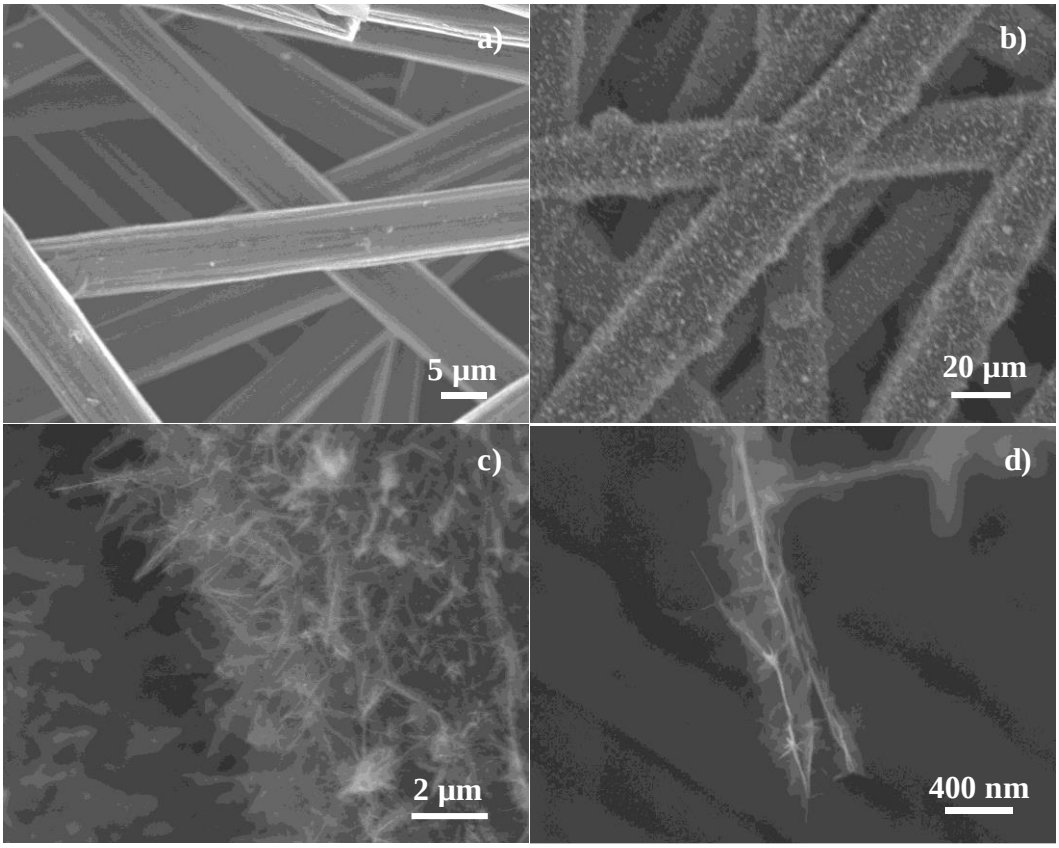

Figure 4-6 SEM images of carbon paper substrate (a) and the feather-like MnO_2 on CP (b-d).

The structure and the detailed morphology was further characterized by HRTEM and SAED, as shown in Figure 4-7. Several staggered long nanowires could be observed from the TEM image, which may be the rachis of the feather-like MnO_2. In addition, a lattice crystal fringe of 0.693 nm can be found from the HRTEM image in Figure 4-7b, assigned to the (110) crystal facet of the α-MnO_2. The SAED pattern in the inset of Figure 4-7b indicated that the polycrystalline characteristic of the as-prepared feather-like MnO_2.

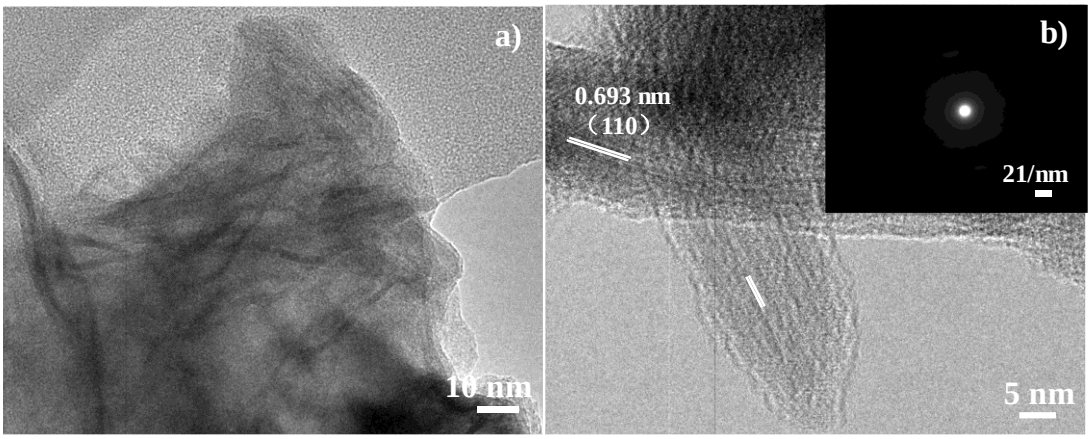

Figure 4-7 (a) TEM and (b) HRTEM images of the feather-like MnO_2 on CP.

4.3.4 Formation mechanism of the feather-like MnO_2 on carbon paper

To further investigate the formation mechanism for the unique feather-like nanostructure of the as-prepared MnO_2 on carbon paper, we prepared samples with different hydrothermal reaction time. By investigating the phase transition and the morphology change of the samples on carbon paper, the formation process was analyzed in detail.

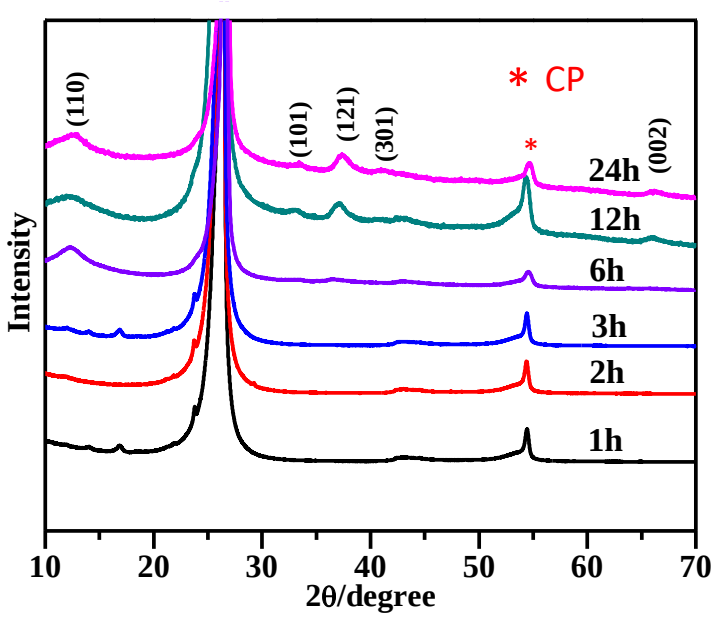

Figure 4-8 XRD patterns of the feather-like MnO_2 on CP with different reaction time.

Figure 4-8 shows the XRD patterns for the as-prepared samples on carbon paper with different reaction time. When the hydrothermal reaction time was less than 6 h, only two diffraction peaks of the carbon paper could be observed for the as-prepared samples. For the as-prepared sample after reacting for 6h, a diffraction peak appeared at 12.745^{o}, indicating that MnO_2 began to grow on the surface of the carbon paper. When the reaction time was increased to 12 h, several diffraction peaks of the MnO_2 could be found. With the further increasing reaction time, the diffraction peak intensities of the MnO_2 became stronger, illustrating the enhanced crystallinity.

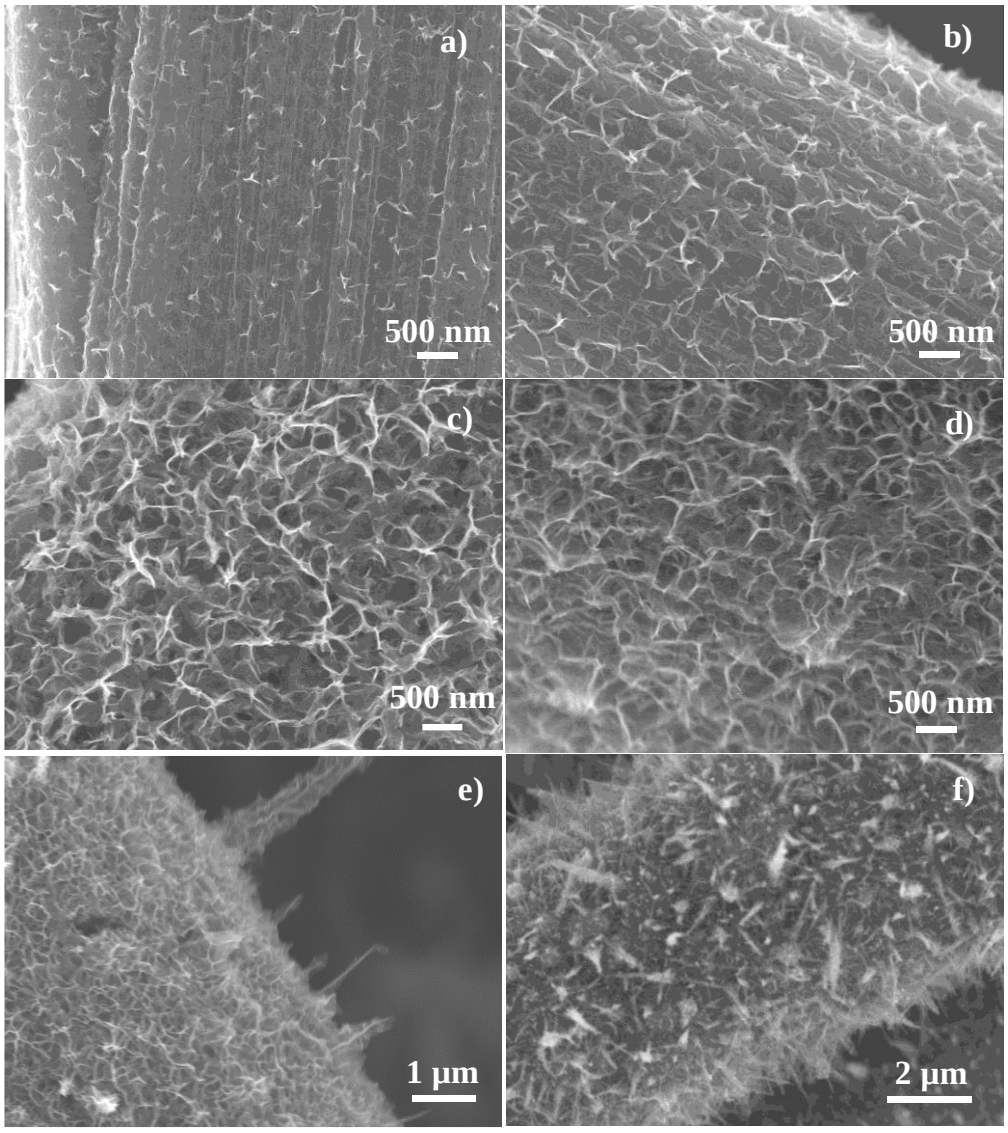

Figure 4-9 SEM images of feather-like MnO_2 on CP for different reaction time: (a) 1 h, (b) 2 h, (c) 3 h, (d) 6 h, (e) 8 h, and (f) 12 h.

The corresponding SEM images for the as-prepared samples on carbon paper with different reaction time was displayed in Figure 4-9. It could be found that the surface of the carbon microfibers was gradually changed to a network structure with the increased reaction time from 1 h to 6 h. When the reaction time prolonged to 8 h, nanowires could be found to directly grow on the network structure. After reacting for 12 h, small nanowires could be observed to further grow around the long nanowires to form a feather-like structure. Moreover, the network structure was covered by more feather-like MnO_2.

The chemical reaction equations for the growth process of the feather-like MnO_2 on carbon paper were inferred as follows: [30]

$$4MnO_4^- + 3C + H_2O \rightarrow 4MnO_2 + 2HCO_3^- + 3CO_2 \quad (1)$$

$$4MnO_4^- + 2H_2O \rightarrow 4MnO_2 + 4OH^- + 3O_2 \quad (2)$$

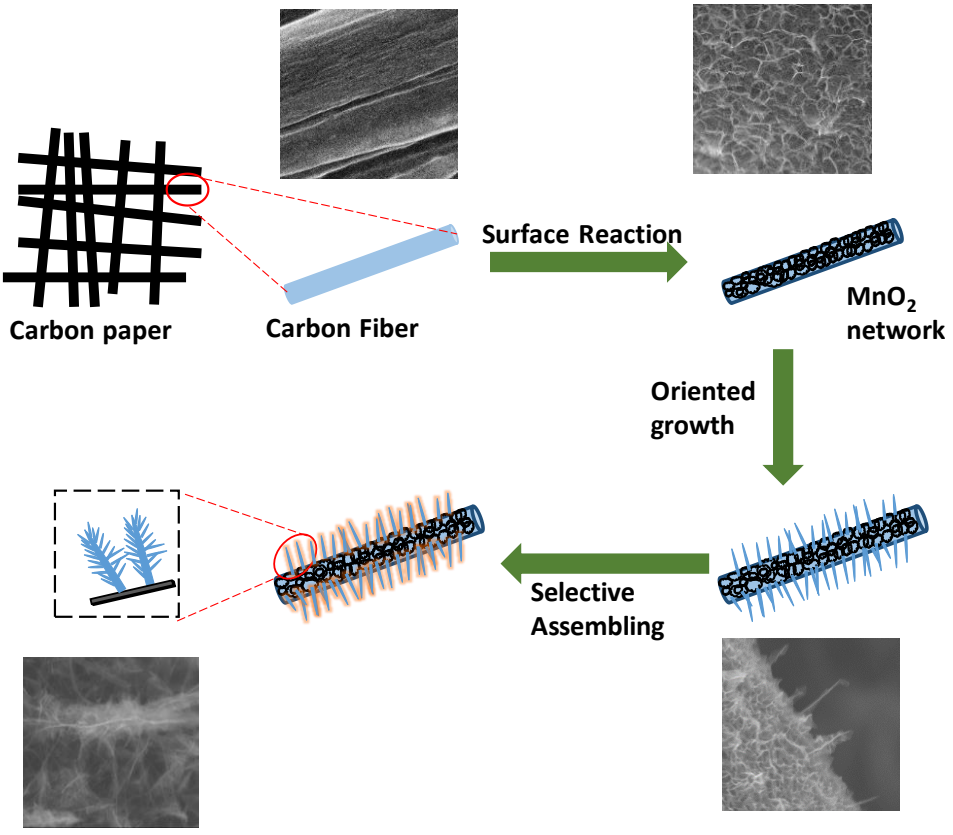

Figure 4-10 Schematic illustration of the preparation of the feather-like MnO_2 on the carbon paper.

Based on the above investigation about the obtained products with different reaction time and the equations, the formation process for the growth of feather-like MnO_2 on carbon paper was supposed as shown in Figure 4-10. When the carbon paper was heated with the $KMnO_4$, the carbon paper was firstly oxidized by $MnO4^-$, leading to the transformation to the network structure for the surface of the carbon microfiber. When the reaction time continued to be increased, eqn (2) occurred and the MnO_2 nanowires began to grow on the carbon network structure vertically. Furthermore, smaller nanowires continued to grow around the vertical nanowires to form the feather-like nanostructure.

4.3.5 Electrochemical performance

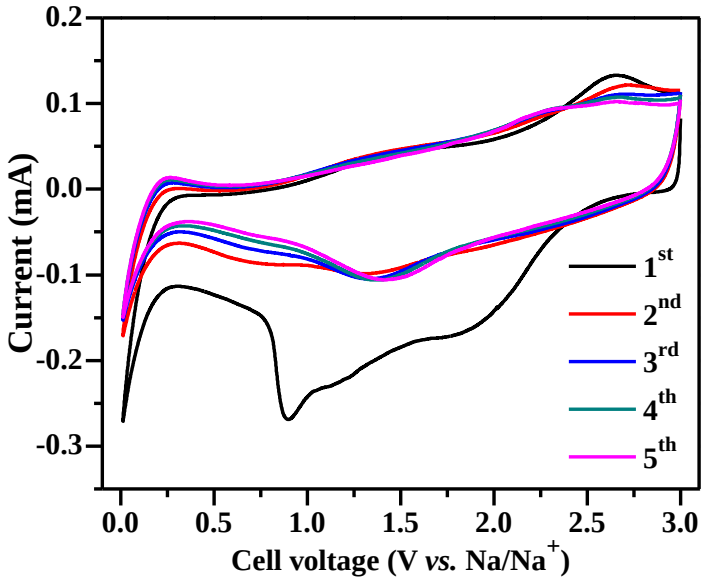

Figure 4-11 CV curves for the initial five cycles at a scan rate of 0.5 mV s^{-1} of the feather-like MnO_2/CP electrode.

The as-prepared feather-like MnO_2 possess a hierarchical nanostructure that may be beneficial for the insertion/desertion of the sodium ions, thus we investigated the electrochemical properties of the as-prepared material in detail. Figure 4-11 displayed the CV curves of the feather-like MnO_2/ carbon paper electrode from 0.01-3 V at a scan rate of 0.5 mV s^{-1}. In the initial cycle, a reduction peak appeared at 0.9 V but disappeared at the subsequent cycles. Compared with the CV curves of the pure carbon paper electrode, this peak corresponded to the activation process of

the carbon. In addition, the initial cycle showed an irreversible CV curve, possibly due to the formation of the solid electrolyte interface (SEI) film as well as some irreversible structure changes of the MnO_2/ carbon paper electrode during the initial cycling process. [4] In the following cycles, a reduction peak at ~1.5 V could be observed, corresponding to the insertion process of the sodium ions. However, no obvious oxidation peak could be found, which might be due to the pseudocapacitive behavior of the MnO_2/ carbon paper electrode. [32] In addition, the position of the peaks as well as the CV curves exhibited nearly no change, illustrating the reversibility for the insertion/desertion of the sodium ions into the MnO_2/ carbon paper electrode.

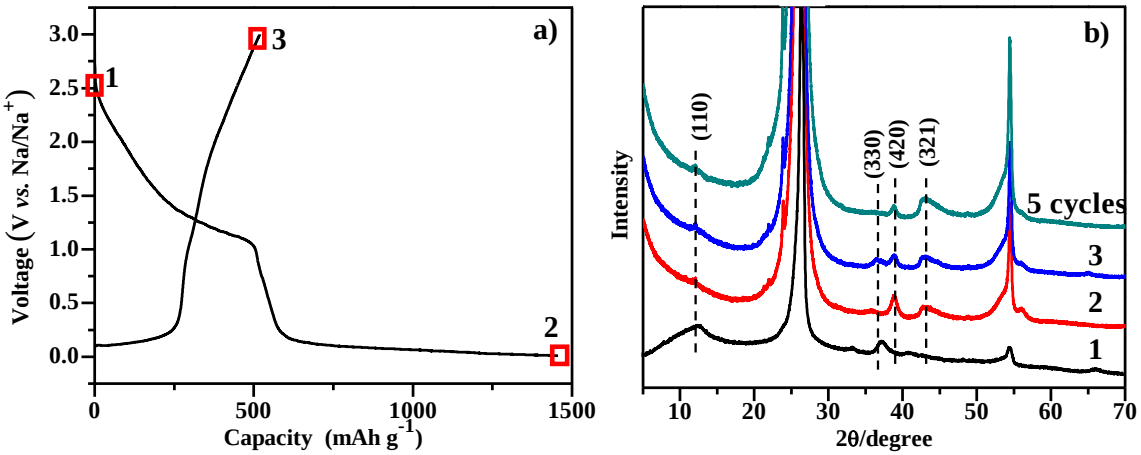

Figure 4-12 Charge-discharge profiles (a) and XRD patterns (b) for the 1st cycle of the feather-like MnO_2/carbon paper electrode.

The charge-discharge profiles of the initial cycle for the feather-like MnO_2/carbon paper electrode was shown in Figure 4-12a. In the first cycle, the feather-like MnO_2/carbon paper electrode could deliver a high discharge specific capacity of nearly 1500 mAh g^{-1}. However, this high discharge capacity was proved to be irreversible, since the following charge specific capacity was ~500 mAh g^{-1}, leading to a low Columbic efficiency of 33.3%. The irreversibility for the initial cycle was consistent with the result shown in CV curves, attributing to the formation of the SEI film and some side reactions. Since it was the first time for the MnO_2 to be employed as the anode for sodium ion batteries, the detailed sodium ion insertion/desertion mechanism was analyzed by investigating the phase transition during the initial charge-discharge

process. As displayed in Figure 4-12a, we marked the discharge voltages at the beginning and 0 V as point 1 and 2, respectively, while the charge voltage at 3.0 V was marked as point 3. The corresponding XRD patterns for the MnO_2/carbon paper electrode at these three points were measured and shown in Figure 4-12b. Interestingly, although the XRD patterns for point 2 and 3 could still be assigned to the α-MnO_2, the characteristic peaks obviously shifted. Four diffraction peaks at 12.114°, 37.010°, 39.046 and 44.833° were assigned to the (110), (330), (420) and (321) crystal planes of the α-MnO_2 (PDF card No. 00-053-0633), respectively. In addition, in the subsequent cycling process, the XRD pattern for the MnO_2/carbon paper electrode remained the same as in the initial cycle, indicating the structure transition is irreversible. The occurrence of the irreversible transition was probably due to the insertion of the sodium ions leading to the tiny distortion of the crystal structure, which is also called the in-situ topotactic transition reaction. [33]

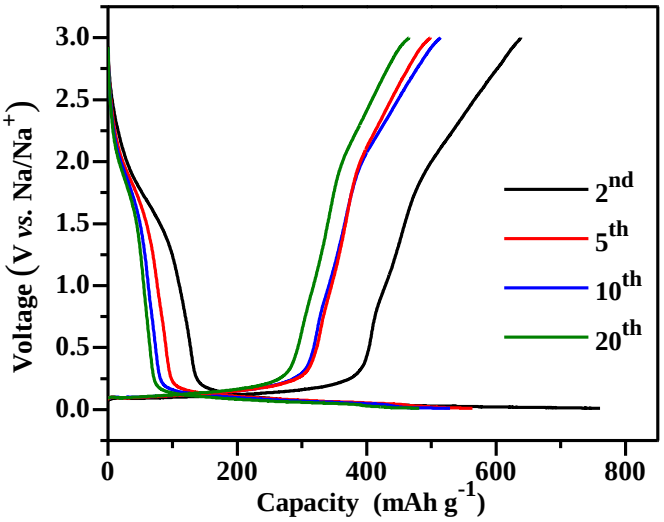

Figure 4-13 Charge-discharge profiles for the 2nd, 5th, 10th and 20th cycles of the feather-like MnO_2/carbon paper electrode at a current density of 0.05 A g^{-1}.

The charge-discharges profiles for the following 2nd, 5th, 10th and 20th cycles under the same current density of 0.05 A g^{-1} were displayed in Figure 4-13. For the 2nd cycle, the discharge and charge capacities were 760.8 and 638.4 mAh g^{-1}, respectively, indicating the increasing Columbic efficiency. Furthermore, the discharge capacity in the 5th, 10th and 20th cycles could

retain at 563.4, 532.2 and 487.1 mAh g^{-1}, respectively, illustrating the good charge/discharge reversibility of the feather-like MnO_2/carbon paper electrode.

Figure 4-14 shows the long cycling performance of the feather-like MnO_2/carbon paper electrode under a current density of 0.1 A g^{-1}. An initial discharge specific capacity of 1280 mAh g^{-1} could be obtained at this current density. Furthermore, it could be observed that even after cycling for 400 times, the discharge capacity could retain at ~300 mAh g^{-1}, and a capacity retention of 63% as calculated from the 2nd cycle was obtained, indicating the excellent electrode stability of the MnO_2/carbon paper electrode. It is worth noting that the long cycling life is better than the previous reports.

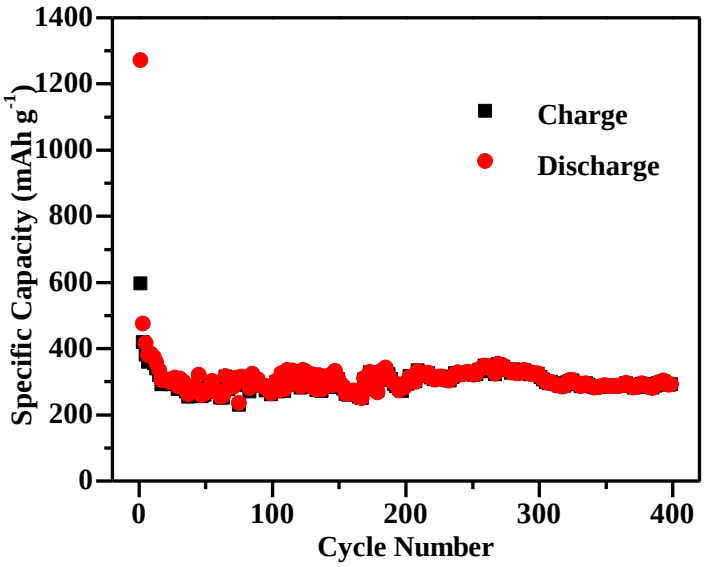

Figure 4-14 Long cycling performance of the feather-like MnO_2/carbon paper electrode at a current density of 0.1 A g^{-1}.

The rate performance of the feather-like MnO_2/carbon paper electrode at different current densities was investigated as well from 0.05 to 0.5 A g^{-1}. At each current densities, the MnO_2/carbon paper electrode was cycled for 10 times. As depicted in Figure 4-15, the feather-like MnO_2/carbon paper electrode exhibited good cycling stability in different current rates. After cycling for 10 times at 0.05 A g^{-1}, a high discharge capacity of 585.7 mAh g^{-1} could be obtained. When the current density increased to 0.1, 0.2 and 0.5 A g^{-1}, the specific capacity was retained at

379.5, 323.2, 305.6 mAh g^{-1}, respectively. After cycling under different current rates for 40 cycles, the feather-like MnO_2/carbon paper electrode could still exhibit a discharge capacity of 355.2 mAh g^{-1} when the current rate returned to 0.1 A g^{-1}, which was very close to the 10-20 cycles under the same current rates. Furthermore, the porous TiO_2 nanopills electrode was measured continually under 0.1 A g^{-1} and nearly no capacity fade was found, indicating the good reversibility of the MnO_2/carbon paper electrode.

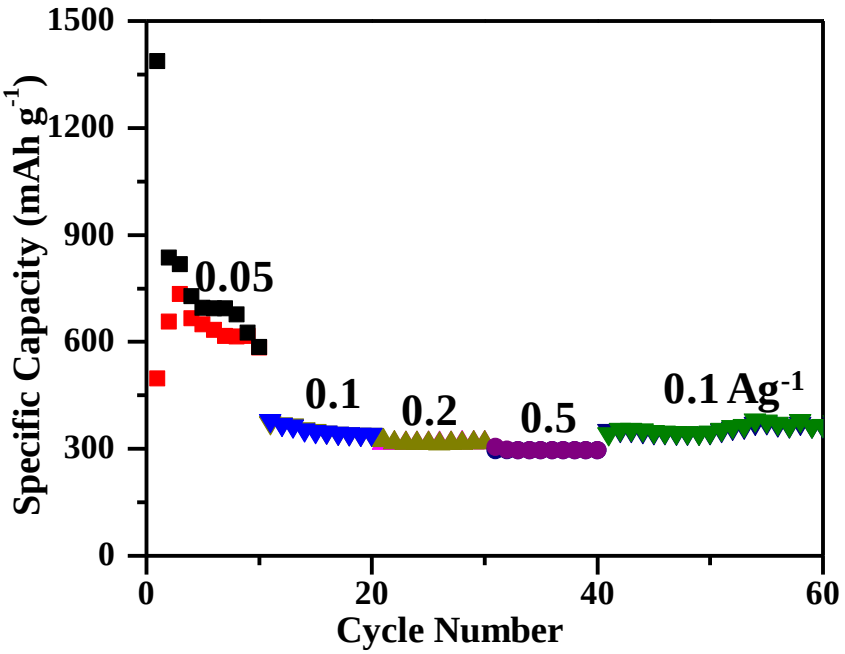

Figure 4-15 Rate performance of the feather-like MnO_2/carbon paper electrode at different current densities from 0.05 to 0.5 A g^{-1}.

To investigate the structure change of the electrochemical system and the property of the electrochemical process, the electrochemical impedance of the feather-like MnO_2/carbon paper electrode without cycling and with cycling for 50 and 200 times was carried out. It could be obviously observed that before cycling, the radius of the semicircle in high-frequency area for the MnO_2/carbon paper electrode was much larger than the semicircles after cycling, indicating the charge transfer resistance was decreased after cycling. The decrease of the charge transfer resistance was consistent with the above calculation results that MnO_2 would change to a conductor characteristic from a semiconductor characteristic. However, after cycling 200 times

the radius of the semicircle in the high-frequency area became larger than the one of 50 cycles, illustrating the charge transfer resistance increased and further explained the capacity fade after cycling for multiple times. In addition, the slopes of the straight lines of the 50 and 200 cycles were different from the line before cycling, implying that irreversible changes occurred in the structure of the MnO_2/carbon paper electrode.

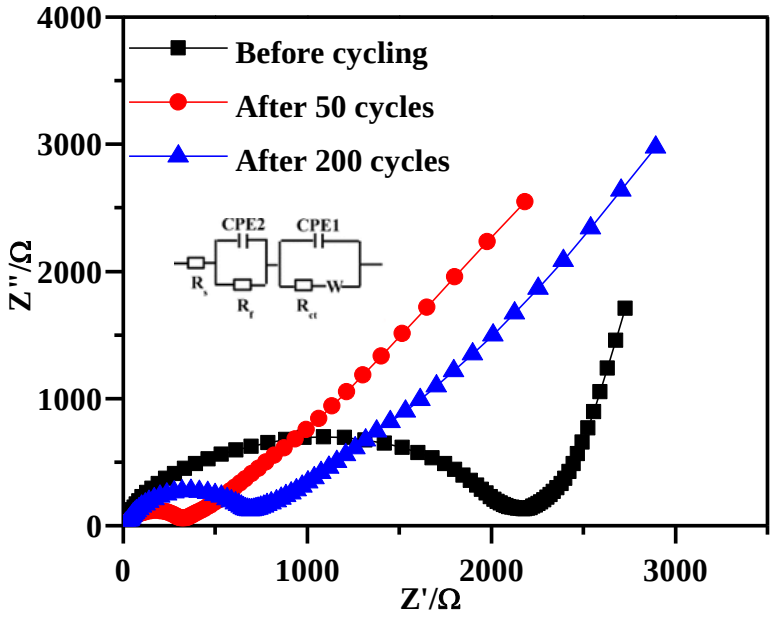

Figure 4-16 EIS plots of the feather-like MnO_2/carbon paper electrode without cycling and with cycling for 50 and 200 times.

The feather-like MnO_2/carbon paper electrode delivered a high specific capacity as well as an excellent stability as the anode for sodium ion batteries, which may be attributed to the advantages of the as-prepared MnO_2/carbon paper electrode as below. First of all, α-MnO_2 materials possess an open tunnel structure, the presence of the vacancies in the tunnels can be beneficial for the insertion of the sodium ions. In addition, by directly employing the MnO_2/carbon paper as an electrode, the combination between the MnO_2 and the current collector was enhanced, further promoting the diffusion of the sodium ions and the electrons. On the other hand, the as-prepared feather-like MnO_2 consists of many ultrathin nanowires with high specific surface areas, which could increase the contact between the electrolyte and the active materials.

The nanosized structure could also shorten the transmission path of the sodium ions. Finally, no binder was added to the electrode, thus, the influence of the binder could be eliminated, which was beneficial to achieving a higher specific capacity. Attributing to these advantages, the as-prepared feather-like MnO_2/carbon paper electrode achieved excellent electrochemical performance as the anode for sodium ion batteries.

4.4 Conclusions

In this chapter, we synthesized in-situ grown feather-like MnO_2 on the carbon paper by a facile hydrothermal method. The formation mechanism of this unique morphology of the MnO_2 was investigated as well. Furthermore, the MnO_2/carbon paper electrode was directly employed as the anode for sodium ion batteries, delivering a high reversible specific capacity and a good rate property. A high discharge capacity of 760.8 mAh g^{-1} was obtained for the 2^{nd} cycle at 0.05 A g^{-1}. Even cycling for 400 times under a current density of 0.1 A g^{-1}, the specific capacity could still retain at ~300 mAh g^{-1}. Therefore, it turned out that the as-prepared feather-like MnO_2 on carbon paper can be a promising anode material for high-performance sodium ion batteries. Moreover, this in-situ growth method on the carbon paper can provide a new fabrication pathway for the binder-free rechargeable secondary battery.

References

[1] J. Liu, X. Xu, R. Hu, L. Yang, M. Zhu. Uniform hierarchical Fe_3O_4@ polypyrrole nanocages for superior lithium ion battery anodes. ***Adv. Energy. Mater.*** 2016, 6(13).

[2] B. H. Hou, Y. Y. Wang, J. Z. Guo, Y. Zhang, Q. L.Ning, Y. Yang, W. H. Li, J. P. Zhang, X. L. Wang and X. L. Wu. A scalable strategy to develop advanced anode for sodium-ion batteries: commercial Fe_3O_4 Derived Fe_3O_4@ FeS with superior full-cell performance. ***ACS Appl. Mater. Interfaces***, 2018, 10 (4), 3581–3589.

[3] L. J. Wang, K. Zhang, Z. Hu, W. C. Duan, F. Y. Cheng, J. Chen. Porous CuO nanowires as the anode of rechargeable Na-ion batteries. ***Nano Res.*** 2014, 7(2): 199–208.

[4] S. Yuan, X. L. Huang, D. L. Ma, H. G. Wang, F. Z. Meng, X. B. Zhang. Engraving copper foil to give large-scale binder-free porous CuO arrays for a high-performance sodium-ion battery anode. ***Adv. Mater.*** 2014, 26, 2273–2279.

[5] Z. S. Hong, M. L. Kang, X. H. Chen, K. Q. Zhou, Z. G. Huang, M. D. Wei. Synthesis of mesoporous Co^{2+}-doped TiO_2 nanodisks derived from metal organic frameworks with improved sodium storage performance. ***ACS Appl. Mater. Interfaces***, 2017, 9 (37), 32071–32079.

[6] H. Li, Z. Zhang, X. Huang, T. B. Lan, M. D. Wei, T. L. Ma. Metal–organic framework derived hierarchical porous TiO_2 nanopills as a super stable anode for Na-ion batteries. ***J. Energy. Chem,*** 2017, 26, 667–672.

[7] M. Zhou, Y. Xu, C. L. Wang, Q. W. Li, J. X. Xiang, L. Y. Liang, M. H. Wu, H. P. Zhao, Y. Lei. Amorphous TiO_2 inverse opal anode for high-rate sodium ion batteries. ***Nano Energy***, 2017, 31: 514-524.

[8] J. F. Ni, S. D. Fu, C. Wu, J. Maier, Y. Yu, L. Li. Self‐supported nanotube arrays of sulfur‐doped TiO_2 enabling ultrastable and robust sodium storage. ***Adv. Mater.*** 2016, 28, 2259–2265.

[9] X. Q. Zhang, Y. C. Zhao, C. G. Wang, X. Li, J. D. Liu, G. H. Yue, Z. D. Zhou. Facile synthesis of hollow urchin-like $NiCo_2O_4$ microspheres for high-performance sodium-ion batteries. ***J. Mater. Sci.***, 2016, 51:9296–9305.

[10] A. K. Mondal, D. W. Su, S. Q. Chen, S. Q. Chen, K. Kretschmer, X. Q. Xie, H. Ahn, G. X. Wang. A microwave synthesis of mesoporous $NiCo_2O_4$ nanosheets as electrode materials for lithium-ion batteries and supercapacitors. ***ChemPhysChem***, 2015, 16:169-175.

[11] M. M. Thackeray. Manganese oxides for lithium batteries. ***Prog. Solid State Chem.***, 1997, 25, 1−71.

[12] A. R. Armstrong, M. Holzapfel, P. Novak, C. S. Johnson, S. H. Kang, M. M. Thackeray, P. G. Bruce. Demonstrating oxygen loss and associated structural reorganization in the lithium battery cathode $Li[Ni_{0.2}Li_{0.2}Mn_{0.6}]O_2$. ***J. Am. Chem. Soc.***, 2006, 128, 8694−8698.

[13] D. A. Tompsett, M. S. Islam. Electrochemistry of hollandite α-MnO_2: Li-ion and Na-ion insertion and Li_2O incorporation. ***Chem. Mater.***, 2013, 25, 2515−2526.

[14] M. S. Wu and P. C. Chiang. Electrochemically deposited nanowires of manganese oxide as an anode material for lithium-ion batteries. ***Electrochem. Commun.***, 2006, 8, 383.

[15] B. X. Li, G. X. Rong, Y. Xie, L. F. Huang and C. Q. Feng. Low-temperature synthesis of α-MnO_2 hollow urchins and their application in rechargeable Li^+ batteries. ***Inorg. Chem.***, 2006, 45, 6404.

[16] M. S. Wu and P. C. Chiang. Synthesis of manganese oxide electrodes with interconnected nanowire structure as an anode material for rechargeable lithium ion batteries. ***J. Phys. Chem. B***, 2005, 109, 23279.

[17] X. P. Han, F. Y. Cheng, C. C. Chen, Y. X. Hu, J. Chen. Uniform MnO_2 nanostructures supported on hierarchically porous carbon as efficient electrocatalysts for rechargeable Li-O_2 batteries. ***Nano Research***, 2015, 8(1), 156-164.

[18] H. H. Xu, X. L. Hu, H. L. Yang, Y. M. Sun, C. C. Hu, Y. H. Huang. Flexible asymmetric micro-supercapacitors based on Bi_2O_3 and MnO_2 nanoflowers: larger areal mass promises higher energy density. ***Adv. Energy. Mater.*** 2015, 5(6).

[19] L. Han, C. X. Shao, B. Liang, A.H. Liu. Genetically engineered phage-templated MnO_2 nanowires: synthesis and their application in electrochemical glucose biosensor operated at neutral pH condition. ***ACS Appl. Mater. Interfaces*** 2016, 8, 22, 13768-13776.

[20] H. Lai, J. Li, Z. Chen, Z. Huang. Carbon nanohorns as a high-performance carrier for MnO_2 anode in lithium-ion batteries. ***ACS Appl. Mater. Interfaces***, 2012, 4, 2325.

[21] L. Li, A. O. Raji, J. M. Tour. Graphene-wrapped MnO_2-graphene nanoribbons as anode materials for high-performance lithium ion batteries. ***Adv. Mater.*** 2013, 25, 6298–6302.

[22] H. Xia, M. O. Lai, L. Lu. Nanoflaky MnO_2/carbon nanotube nanocomposites as anode materials for lithium-ion batteries. ***J. Mater. Chem.***, 2010, 20, 6896-6902.

[23] S. Q. Zheng, F. F. Yang, S. L. Chen, L. Liu, Q. Xiong, T. Yu, F. Zhao, U. Schroder, H. Q. Hou. Binder-free carbon black/stainless steel mesh composite electrode for high-performance anode in microbial fuel cells. ***J. Power Sources*** 2015, 284, 252-257.

[24] A. Sivanantham, P. Ganesan, S. Shanmugam. Hierarchical $NiCo_2S_4$ nanowire arrays supported on Ni foam: an efficient and durable bifunctional electrocatalyst for oxygen and hydrogen evolution reactions. ***Adv. Funct. Mater.*** 2016, 26, 4661–4672.

[25] S. Y. Wang, R. A. Dryfe. Graphene oxide-assisted deposition of carbon nanotubes on carbon cloth as advanced binder-free electrodes for flexible supercapacitors. ***J. Mater. Chem. A*** 2013, 1, 5279-5283.

[26] X. Zhang, J. S. Luo, P. Y. Tang, X. L. Ye, X. X. Peng, H. L. Tang, S. G. Sun, J. Fransaer. A universal strategy for metal oxide anchored and binder-free carbon matrix electrode: A supercapacitor case with superior rate performance and high mass loading. ***Nano Energy*** 2017, 31, 311-321.

[27] H. Li, H. L. Fei, X. Liu, J. Yang, M. D. Wei. In situ synthesis of $Na_2Ti_7O_{15}$ nanotubes on a Ti net substrate as a high performance anode for Na-ion batteries. ***Chem. Commun.*** 2015, 51(45), 9298-9300.

[28] T. L. Gu, Z. Y. Cao, B. Q. Wei. All-manganese-based binder-free stretchable lithium-ion batteries. ***Adv. Energy Mater.*** 2017, 7(18).

[29] Y. Q. Jin, H. C. Yuan, J. L. Lan, Y. H. Yu, Y. H. Lin, X. P. Yang. Bio-inspired spider-web-like membranes with a hierarchical structure for high performance lithium/sodium ion battery electrodes: the case of 3D freestanding and binder-free bismuth/CNF anodes. ***Nanoscale*** 2017, 9(35), 13298-13304.

[30] V. Subramanian, H. W. Zhu, R. Vajtai, P. M. Ajayan, B. Q. Wei. Hydrothermal synthesis and pseudocapacitance properties of MnO_2 nanostructures. ***J. Phys. Chem. B*** 2005, 109, 20207-20214.

[31] J. Yan, Z. J. Fan, T. Wei, W. Z. Qian, M. L. Zhang, F. Wei. Fast and reversible surface redox reaction of graphene-MnO_2 composites as supercapacitor electrodes. ***Carbon*** 2010, 48(13), 3825-3833.

[32] D. C. Chen, D. Ding, X. X. Li, G. H. Walter, X. H. Xiong, M. S. El-Sayed, M. L. Liu. Probing the charge storage mechanism of a pseudocapacitive MnO_2 electrode using in operando Raman spectroscopy. ***Chem. Mater.*** 2015, 27, 6608-6619.

[33] C. Reitz, C. Suchomski, D. Wang, H. Hahn, T. Brezesinski. In situ tuning of magnetization via topotactic lithium insertion in ordered mesoporous lithium ferrite thin films. ***J. Mater. Chem. C*** 2016, 4, 8889-8896.

Chapter 5 Synthesis and application of 2D titanium carbide Ti_3C_2 and its composite for sodium-ion battery

5.1 Introduction

In recent years, two-dimensional (2D) layer structure materials have attracted great attention for energy storage systems due to their open structure and high surface area. For the application in rechargeable secondary batteries, a typical representative of the 2D layer structure materials is graphene, which is of high conductivity and power density. [1-3] However, despite of these advantages, the expensive price of the graphene has limited the further large-scale application. Thus, some graphene-like structural materials have been gradually developed as alternatives, such as transition metal sulfides, transition metal oxides, transition metal hydroxides, etc. Among them, transition metal carbide or nitride (MXene), a relatively new member of the 2D material family, has gradually become a hot research material for the rechargeable secondary batteries in recent years, attributing to their high conductivity and excellent chemical reactivity. [4]

Ti_3C_2 has already been widely studied as an anode material for the LIBs for its relatively high specific capacity and controllable morphology. [5-8] Afterwards, the application of the Ti_3C_2in the SIB has gradually emerged as well. It was reported Ti_3C_2 powder only exhibited a discharge capacity of 100 mAh g^{-1} at a current density of 20 mA g^{-1}. [9] Compared with other anode materials, Ti_3C_2 as the electrode material possess a good stability while the specific capacity still has space to be improved. An effective method for the improvement of the specific capacity is to composite with other materials that have high theoretical specific capacity or conductivity. In fact, some researchers have already composited Ti_3C_2 with materials such as MoS_2 and Sb_2O_3, which delivered high discharge capacity than Ti_3C_2 materials. [10, 11]

On the other hand, black phosphorous (BP) with an extremely high theoretical specific capacity of 2596 mAh g^{-1} have also been regarded as a promising candidate for sodium ion batteries. As calculated by Yuan et al, BP could form an Ohmic contact with the MXene ($Zr_{n+1}C_nT_2$, n= 1, 2) in the vertical direction based on the work functional group on the surface of the MXene. [12]

Therefore, we suppose that the BP may also be able to form an Ohmic contact with other MXene materials.

In this chapter, we prepared a BP/Ti_3C_2 composite by composting BP nanoparticles and Ti_3C_2. Furthermore, the BP/Ti_3C_2 composite was investigated as the anode materials for sodium ion batteries. In addition, the sodium ion storage mechanism for the BP/Ti_3C_2 composite electrode was also discussed in this work.

5.2. Experimental section

5.2.1 Preparation of BP nanoparticles

The bulk BP was synthesized by a ball-milling method. 1 g of red phosphorous after grind milling for 1 h was added into a stainless steel container with 50 g of zirconium beads and ball-milled for 24 h under an Ar atmosphere. To prepare BP nanoparticles, 100 mg of as-prepared BP powder was ball-milled again in 10 mL N, N-Dimethylformamide (DMF) solution for 12 h. Then the obtained mixed solution was transferred into a 100 mL vial with 90 mL DMF solvent and sonicated for 12 h under Ar protection. The suspension after centrifugation at 3500 rpm was sequentially collected (~ 1 mg mL^{-1}).

5.2.2 Exfoliation of Ti_3C_2

Firstly, the Ti_3C_2 powder was obtained by etching Ti_3AlC_2 with HF at room temperature for 30 h. To prepare exfoliated Ti_3C_2, 300 mg of Ti_3C_2 powder was dispersed into 10 mL dimethyl sulfoxide (DMSO) and stirred for 18 h. After centrifuged at 10000 rpm, the obtained powder was added into 100 mL deionized water and sonicated for 2 h. Finally, the dispersed solution was centrifuged at 3500 rpm and the supernatant was collected (~ 1 mg mL^{-1}).

5.2.3 Preparation of BP/Ti_3C_2 composite

For the preparation of the BP/Ti_3C_2 composite, 10 mL BP/DMF solution was mixed with 50 mL Ti_3C_2/DI water dispersion in an autoclave. After magnetically stirred for 24 h and sonicated for 1 h, the mixture was filtered through a polytetrafluoroethylene (PTFE) separator membrane with a diameter of 21 mm. Then the obtained product was dried in a vacuum oven at room temperature overnight.

5.2.4 Characterization and electrochemical measurements

The testing conditions for the physical characterizations were shown in Chapter 2.

The as-prepared BP/Ti_3C_2 composite was mixed with acetylene black additives and PVDF binder in a mass ratio of 7:2:1. By using NMP as the solvent, the mixed slurry was coated onto the Cu foil disc and then dried at 110^{o}C for 12 h. The mass loading for each disc was ca. 2 mg cm^{-2}. The obtained BP/Ti_3C_2 composite electrode was employed as the anode electrode. The half-cells were assembled in a glove box using sodium metal as the counter electrode and 1M $NaClO_4$ in the PC and EC (volume ratio 1:1) mixed solvent as the electrolyte. As a comparison, the BP and Ti_3C_2 electrode were also prepared by the same method, respectively.

The Cyclic Voltammetry was measured in a CHI660C electrochemical workstation. The cycling performance and the charge-discharge profiles of the as-prepared samples were obtained in a Land CT2001A battery tester device. Both the voltage ranges for the Ti_3C_2 and the BP/Ti_3C_2 composite electrode were from 0.01 V to 3 V, while the voltage range for BP electrode was 0.01-2 V.

5.3 Results and discussion

5.3.1 XRD analysis

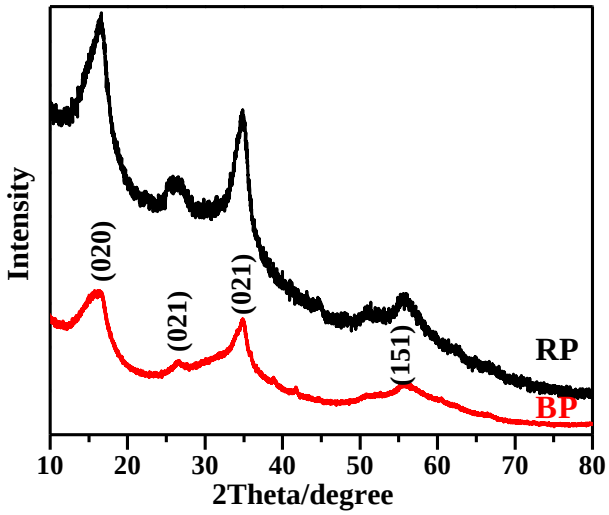

Figure 5-1 XRD patterns for RP and as-prepared BP after ball milling.

Figure 5-1 shows the XRD patterns for the RP and the as-prepared products after ball milling. It could be observed the RP raw material was amorphous with no obvious characteristic peak. After ball-milling for 24 h, the diffraction peaks could be assigned to the standard PDF card of BP (PDF card No. 01-076-1958, Cmca), indicating that the RP raw material had already been successfully converted to the BP.

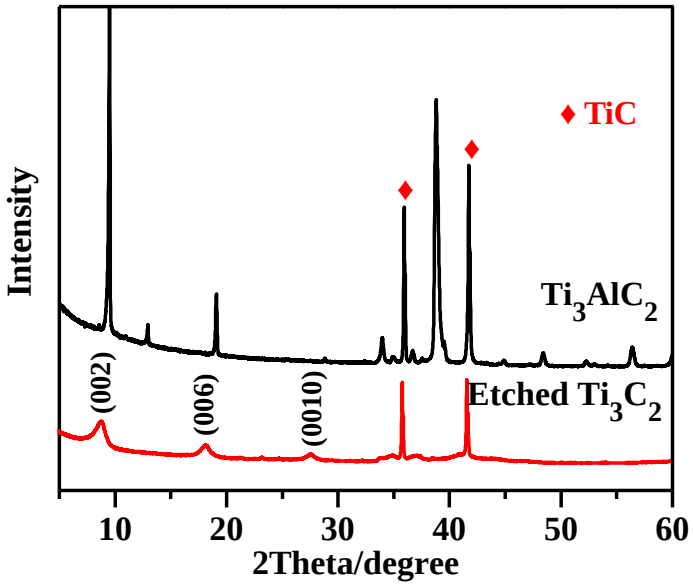

Figure 5-2 XRD patterns for Ti_3AlC_2 and products after etching.

The XRD patterns for the Ti_3AlC_2 and the product after etching were displayed in Figure 5-2. After etching, the characteristic peak at 10° shifted to 8.9°, indicating the removal of the Al metal layer. Three diffraction peaks at 8.9°, 18.31° and 27.7° were assigned to the (002), (006) and (0010) planes, which was consistent with the previously reported results. [9] No peak of Ti_3AlC_2 existed after the etching process. However, two strong peaks at 35.4° and 42.1° belonged to the peaks of TiC in the Ti_3AlC_2 raw material, which was difficult to be removed.

The XRD pattern for the obtained composite was shown in Figure 5-3. Two characteristic peaks of BP at 35.47° and 42.58° could be assigned to the peaks of the BP, while other diffraction peaks belong to the Ti_3C_2. The XRD results indicated that the BP/Ti_3C_2 composite was successfully prepared while BP did not insert into the interlayer of the Ti_3C_2 crystal structure.

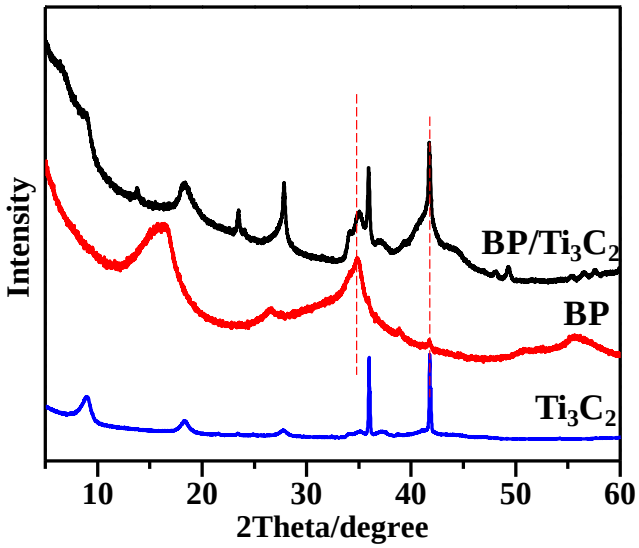

Figure 5-3 XRD patterns for as-prepared BP, Ti_3C_2 and the obtained composite.

5.3.2 SEM analysis

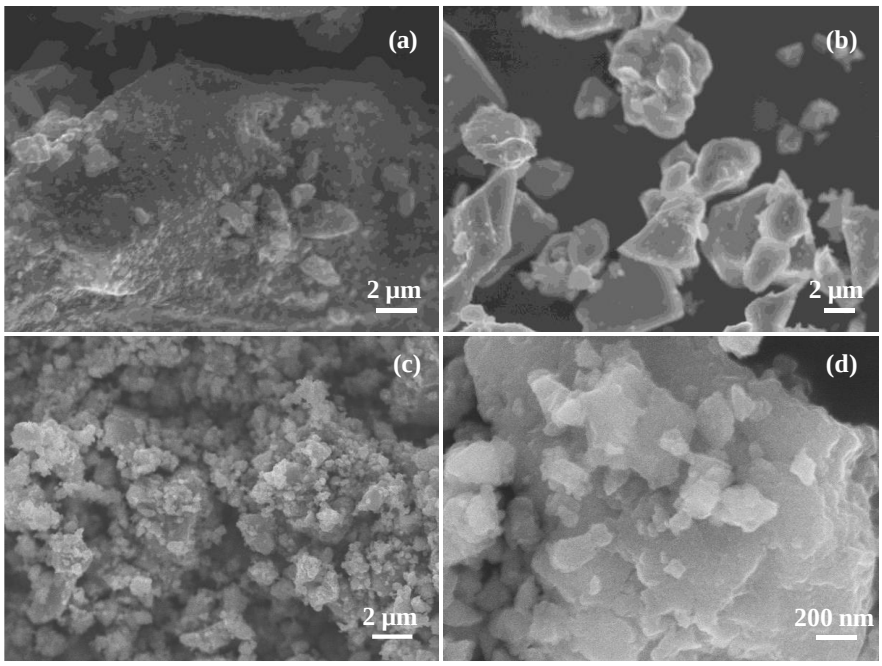

Figure 5-4 SEM images of the RP raw materials (a), RP after grind milling (b) and BP after ball milling (c-d).

As shown in Figure 5-4a and 5-4b, the purchased RP consisted of extremely large bulks over 10 μm in size while after grinding the particle size of the RP was significantly reduced to an average of 3-4 μm. The SEM images of the BP after ball milling was displayed in Figure 5-4c and 4d. After ball milling, the obtained BP showed an average particle size of smaller than 2 μm. In addition, it could be observed from Figure 5-4d that the as-prepared BP possessed layer structures.

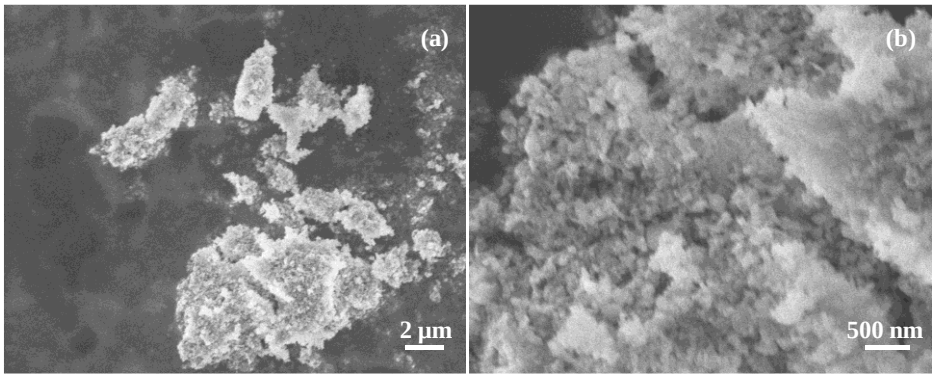

Figure 5-5 SEM images of BP after sonicating in DMF solution.

In order to observe the morphology of the BP after sonicating, the small BP particles in the DMF solution were filtered and collected for the SEM observation. Figure 5-5 shows the SEM images of the BP after sonicating in the DMF solution. Different from the large bulk structure of the BP obtained by ball milling, the BP in the DMF solution displayed the morphology of small nanoparticles. The uniform BP nanoparticles possess an average particle size of ca. 20~30 nm.

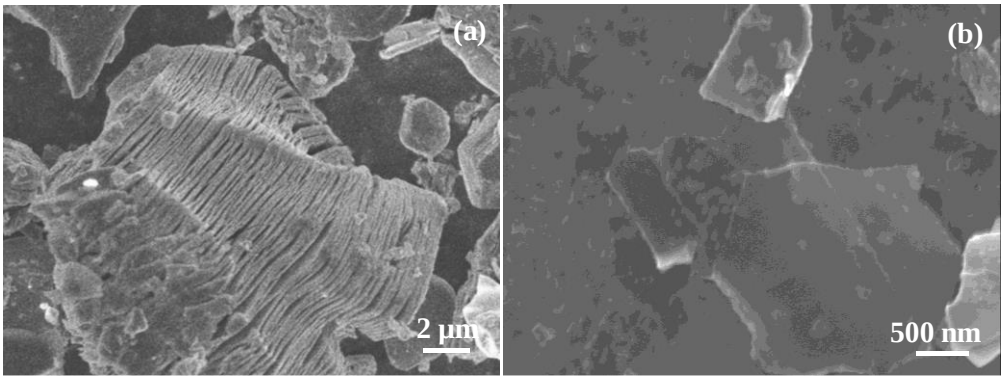

Figure 5-6 SEM images of bulk Ti_3C_2 (a) and exfoliated Ti_3C_2 in deionized water (b).

Figure 5-6 shows the SEM images of the bulk Ti_3C_2 and the exfoliated Ti_3C_2 in deionized water. From the SEM image of the etched Ti_3C_2, an accordion-like layer structure could be observed. Most layers separated from each other, which was due to the removal of the Al layers. The thickness for each layer was ca. 50 nm. The Ti_3C_2 after the exfoliation process was shown in Figure 5-6b. Ultrathin nanoflakes larger than 1.5 μm could be observed, illustrating the Ti_3C_2 was successfully exfoliated.

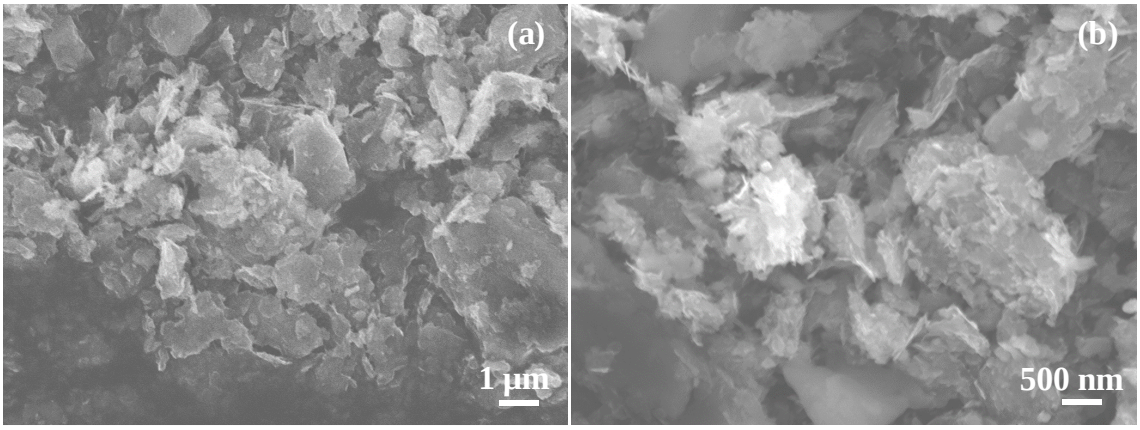

Figure 5-7 SEM images of the BP/ Ti_3C_2 composite.

In the SEM images of the BP/ Ti_3C_2 composite (Figure 5-7), the densely restacked Ti_3C_2 nanoflakes could be observed. However, the BP nanoparticles could not be clearly found from the SEM images, since BP nanoparticles might be wrapped by the densely restacked Ti_3C_2 nanoflakes.

5.3.3 Electrochemical performance

In order to compare the difference between the electrochemical reaction mechanisms of the Ti_3C_2 and the BP/Ti_3C_2 composite electrode, the CV curves for the 2nd cycle of the two electrodes were displayed in Figure 5-8. In the CV curves of the Ti_3C_2 electrode, it was found that the 1st cycle exhibited the same curves with the subsequent cycles, illustrating nearly no side reaction occurring for the initial cycle for this material. In addition, the four cycles nearly coincided with each other, indicating the excellent stability of the Ti_3C_2 electrode. Furthermore, a pair of reduction peak at ~1.75 V and oxidation peak at ~2 V was observed, which could be

assigned to the redox process of the Ti^{4+}/Ti^{3+}. Meanwhile, the BP/Ti_3C_2 composite exhibited a set of completely different CV curves from the pure Ti_3C_2, as shown in Figure 5-8a. A reduction peak appeared at ~0.75 V during the first discharging process, while in the following cycles this reduction peak disappeared. Thus, this peak might correspond to the side reactions of the BP in this composite. In the subsequent cycles, a sharp reduction peak appeared at 0.25 V, which may be due to the sodium ion insertion into the structure of BP. Meanwhile, a sharp oxidation peak at 0.7 V could be found for each cycle, while a weaker oxidation peak at 2 V could be observed for the first 2 cycles but disappeared from the 3rd cycle. Compared with the CV curves of the Ti_3C_2 electrode, the oxidation peak at 2 V belongs to the sodium ion desertion process from the Ti_3C_2, and the reduction peak for Ti_3C_2 was not found. On the contrary, a pair of peaks was found in lower voltage, indicating the sodium ion inserted into the structure of both the BP and the Ti_3C_2, while the insertion process into Ti_3C_2 structure was more irreversible.

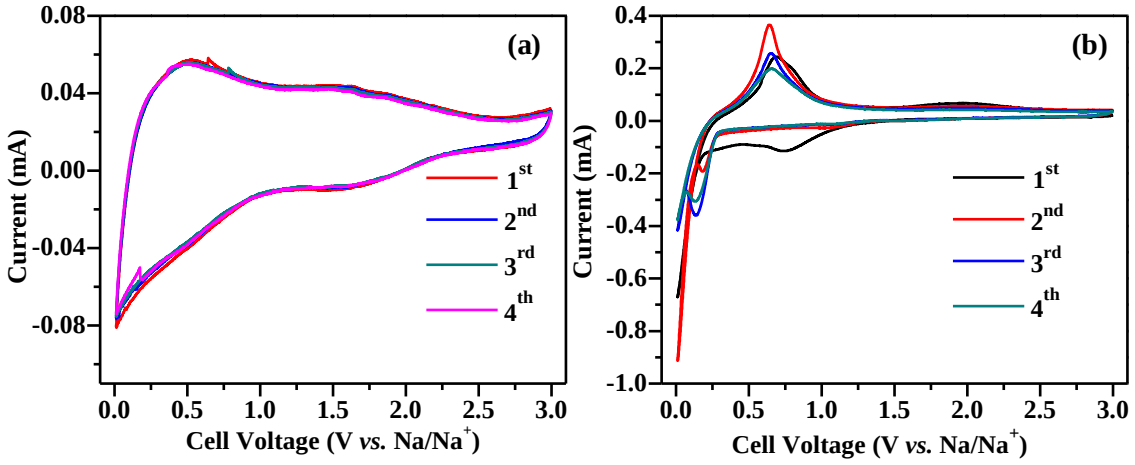

Figure 5-8 CV curves for the initial four cycles at a scan rate of 0.5 mV s^{-1} of Ti_3C_2 (a) and BP/ Ti_3C_2 (b) electrode.

The charge-discharge curves for the 10th cycle of the BP, the Ti_3C_2 and the BP/ Ti_3C_2 composite electrodes under a current density of 0.1 A g^{-1} were displayed in Figure 5-9a. Obviously, the BP/Ti_3C_2 composite exhibited an improved discharge specific capacity of 331.9 mAh g^{-1} than that of the BP and the Ti_3C_2 electrodes, which were 146.1 and 98.5 mAh g^{-1}, respectively. It was worth noting that both the voltage plateaus for the BP and the Ti_3C_2 electrodes were difficult to observe. After compositing, a discharge voltage plateau at ~0.25 V can be found clearly, which

made a great contribution to the obtained specific capacity. Thus, the BP/Ti_3C_2 composite electrode achieved a higher specific capacity than that of the BP and the Ti_3C_2 electrodes. Moreover, this low voltage plateau was also beneficial to matching with other cathode materials. The charge-discharge profiles of the 1st, 2nd and 10th cycles for the BP/Ti_3C_2 composite electrode at a current density of 0.1 A g^{-1} was shown in Figure 5-9b. For the initial cycle, high discharge and charge capacity of 1280 and 661.9 mAh g^{-1} was delivered, respectively, indicating the formation of an SEI film and some side reactions also occurred for the BP/Ti_3C_2 composite electrode. Subsequently, the BP/Ti_3C_2 composite electrode could retain relatively high discharge specific capacity of 774.4 and 331.9 mAh g^{-1} for the 2nd and 10th cycles, respectively, revealing the electrode stability of the BP/Ti_3C_2 composite. Moreover, the increased Columbic efficiency also indicated a good reversibility of the sodium ion insertion/desertion process.

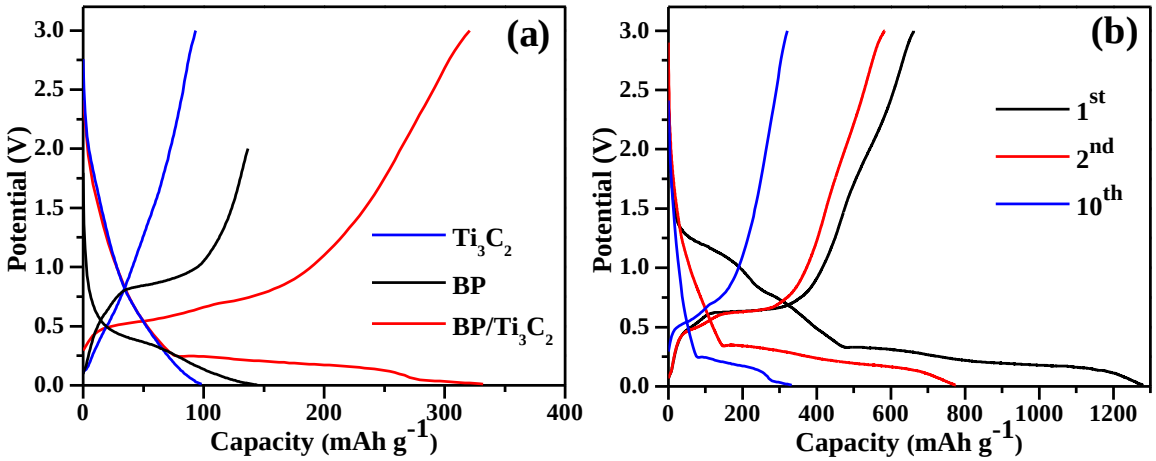

Figure 5-9 charge-discharge profiles of the BP, the Ti_3C_2 and the BP/Ti_3C_2 composite electrode at the 10th cycle (a) and the BP/Ti_3C_2 composite electrode for the 1st, 2nd and 10th cycles (b) at a current density of 0.1 A g^{-1}.

In addition, the charge-discharge profiles for the BP and the Ti_3C_2 electrodes under the same current rate were displayed in Figure 5-10. Since the BP was reported to possess a relatively narrow voltage window, the as-prepared BP electrode was measured at a voltage range of 0.1-2 V. [13, 14] As displayed in Figure 5-10a, the BP electrode can deliver an extremely high initial discharge capacity of 1687.8 mAh g^{-1}, while in the 2nd and 5th cycles the discharge capacity

decreased to 691.4 and 241.4 mAh g^{-1}, illustrating the irreversibility of the BP electrode. In addition, despite of the high initial Columbic efficiency, the Ti_3C_2 electrode exhibited a relatively lower discharge capacity of 286.1, 148.6 and 98.5 mAh g^{-1} for the 1st, 2nd and 10th cycles, respectively.

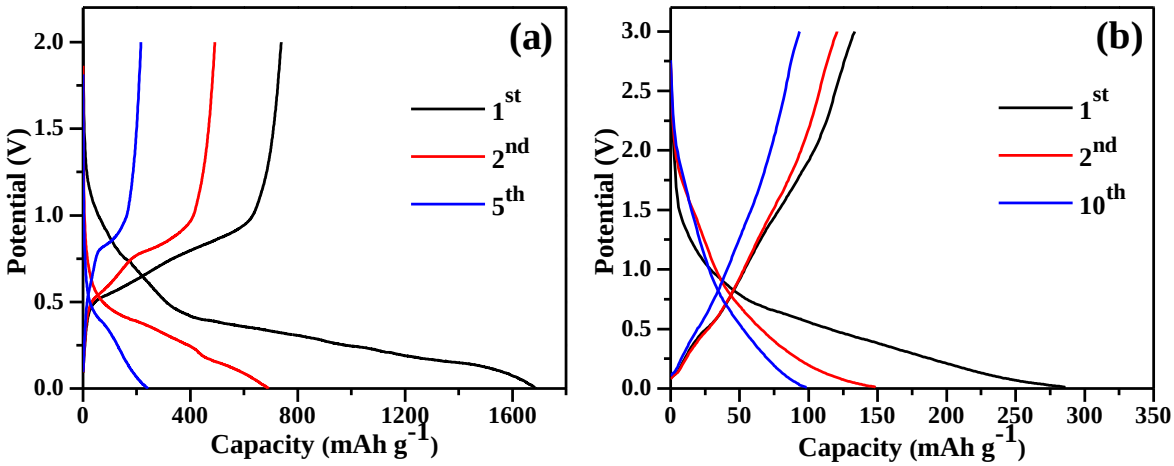

Figure 5-10 Charge-discharge profiles for the 1st, 2nd and 5th cycles of the BP electrode from 0.1 V to 2 V (a) and the 1st, 2nd and 10th cycles for the Ti_3C_2 electrode from 0.01 V to 3 V at a current density of 0.1 A g^{-1}.

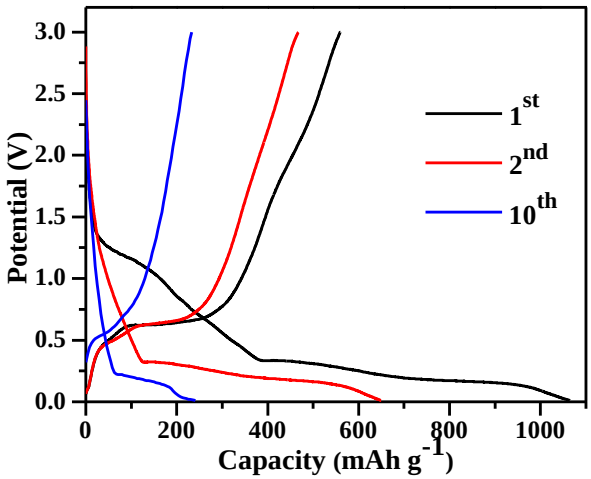

Figure 5-11 Charge-discharge profiles for the 1st, 2nd and 10th cycles of the BP/Ti_3C_2 electrode from 0.01 V to 3 V at a current density of 0.5 A g^{-1}.

In addition, the charge-discharge profiles for the 1st, 2nd and 10th cycles of the BP/Ti_3C_2 composite electrode at a current density of 0.5 A g^{-1} were also displayed in Figure 5-11. The BP/Ti_3C_2 composite electrode also delivered a high but irreversible initial discharge and charge specific capacities of 1064 and 559.5 mAh g^{-1}. In the 2nd and 10th cycles, discharge capacities of 649.0 and 240.8 mAh g^{-1} could be achieved, respectively, indicating a good reversibility with a high current rate.

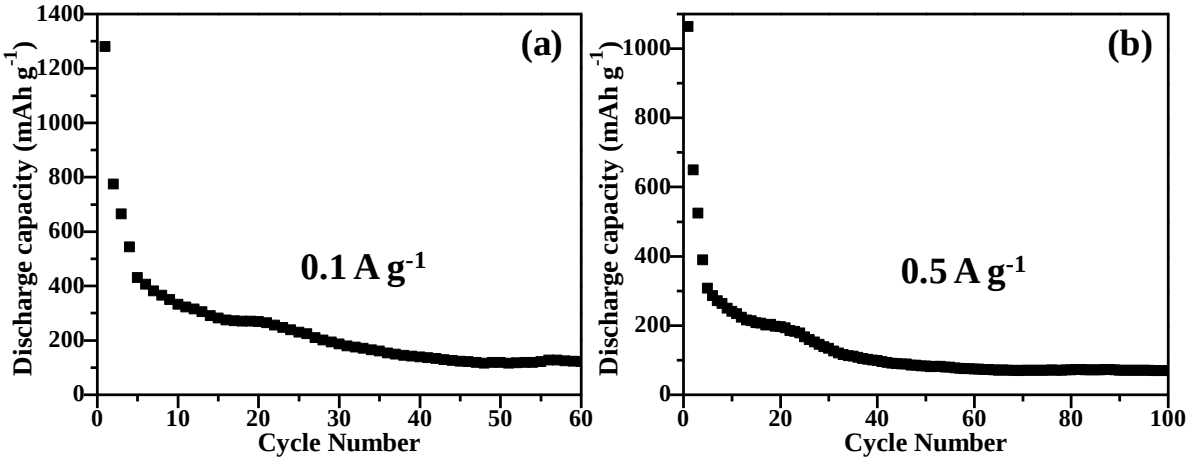

Figure 5-12 Cycling performance of the BP/Ti_3C_2 composite at a current density of 0.1 A g^{-1} (a) and 0.5 A g^{-1} (b).

Figure 5-12a shows the cycling performance of the BP/Ti_3C_2 composite electrode at a current density of 0.1 A g^{-1}. Although the specific capacity faded with the increasing cycling times, a discharge capacity of about 121.1 mAh g^{-1} was remained after 60 cycles. In addition, the BP/Ti_3C_2 composite electrode remained a specific capacity of 80 mAh g^{-1} after cycling for 100 times in a much higher current density of 0.5 A g^{-1}, as depicted in Figure 5-12b. It could be observed that both at a current density of 0.1 and 0.5 A g^{-1} the discharge capacity could remain over 200 mAh g^{-1} for the first 20 cycles. Afterward, the specific capacity gradually faded with the increased cycles. Thus, we supposed that the layer structure of the BP or the Ti_3C_2 in the composite might landslide after repeating the insertion/desertion process of the sodium ions for multiple times.

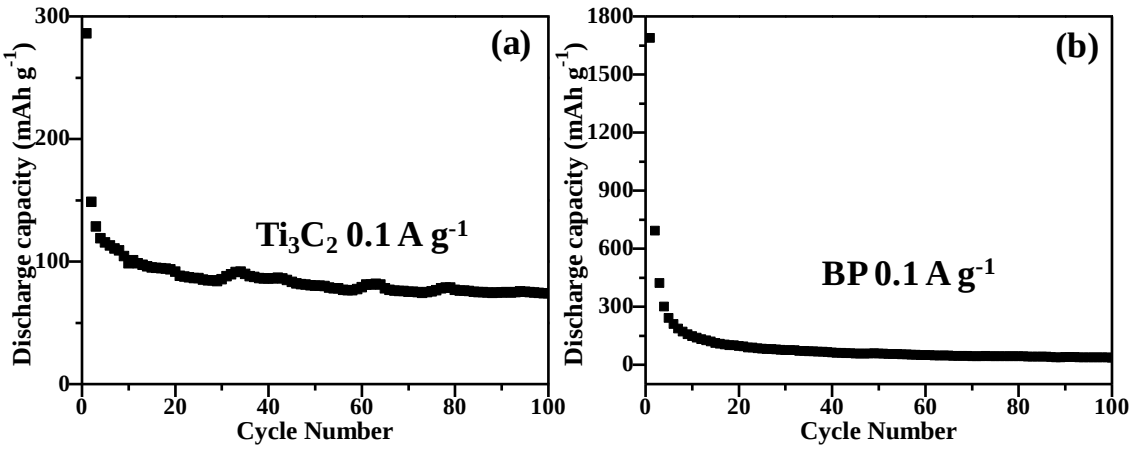

Figure 5-13 Cycling performance of the BP electrode (a) and Ti_3C_2 electrode (b) at a current density of 0.1 A g^{-1}.

In addition, we also measured the cycling performance of the BP and the Ti_3C_2 electrodes at a current density of 0.1 A g^{-1} as a comparison. The Ti_3C_2 electrode showed a discharge capacity of 74 mAh g^{-1} after 100 cycles with relatively better stability, as depicted in Figure 5-13a. On the other hand, the BP electrode delivered a high initial specific capacity, but faded quickly during the following cycles. After cycling for 100 times, a discharge capacity of only 36 mAh g^{-1} was maintained for the BP electrode. It could be concluded that the BP/Ti_3C_2 composite showed a better discharge capacity than the other two electrodes after cycling for multiple times under the same current density, and a centered stability among these three electrodes.

Figure 5-14 shows the rate performance of the BP/Ti_3C_2 composite electrode with current density range from 0.05 to 1 A g^{-1}. An initial irreversible discharge capacity of 1400 mAh g^{-1} was achieved at a current rate of 0.05 A g^{-1}. After cycling for 10 times at 0.05 A g^{-1}, a high discharge capacity of nearly 300 mAh g^{-1} could be remained. Afterward, when the current density was increased to 0.1, 0.2 and 0.5 A g^{-1}, the specific capacities were remained at 172.1, 119, 88.7 mAh g^{-1}, respectively. Even at a high current density of 1 A g^{-1}, the BP/Ti_3C_2 composite electrode could remain a specific capacity of 67.3 mAh g^{-1}, indicating good rate capability of this composite electrode. After cycling under different current rates for 50 cycles, when the current density returned to 0.1 A g^{-1} the BP/Ti_3C_2 composite electrode could still exhibit a discharge capacity of 132 mAh g^{-1}. In addition, after continuing to cycling under the current density of 0.1

A g^{-1}, the BP/Ti_3C_2 composite electrode maintained a specific capacity of ~100 mAh g^{-1} even after 200 cycles, illustrating a good reversibility of the BP/Ti_3C_2 composite electrode.

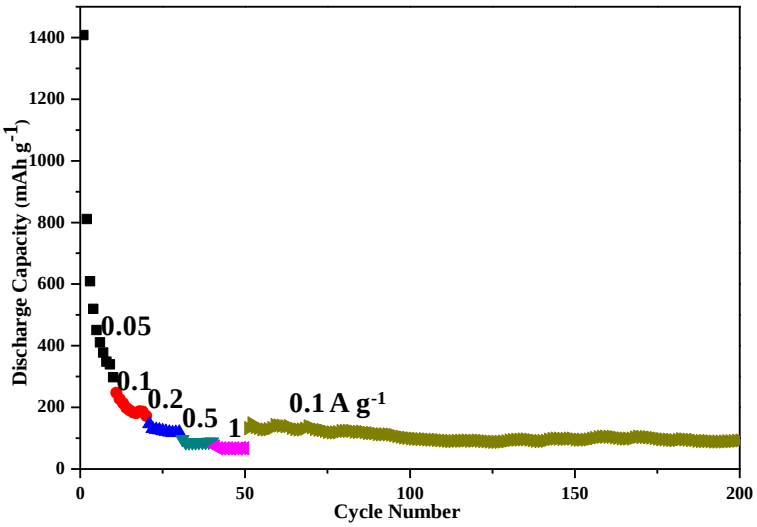

Figure 5-14 Rate performance of the BP/Ti_3C_2 composite from 0.05 to 1 A g^{-1}.

The BP/Ti_3C_2 composite electrode exhibited a better electrochemical performance than the BP and the T_3C_2 electrodes as the anode for the sodium-ion batteries, which might be attributed to the following reasons: Firstly, both the BP and the Ti_3C_2 possess 2D layer structures, which could permit the insertion of the sodium ions into the interlayer space. Furthermore, the layer structure also provides a large specific surface area for the storage capability of the sodium ions. In addition, by compositing small BP nanoparticles on the surface of the exfoliated Ti_3C_2, the specific surface area as well as the active sites on the Ti_3C_2 layer were further improved, which was beneficial to the storage of the sodium ions and the electrolyte. In addition, the nanostructure also contributes to shortening the diffusion pathways of the sodium ions and the electrons.

5.4 Conclusions

In this chapter, we prepared a BP/Ti_3C_2 composite by compositing small BP nanoparticles with exfoliated Ti_3C_2 layers. When applied as an anode for the sodium ion batteries, the composite electrode exhibited an improved electrochemical performance than the Ti_3C_2 electrode. A high discharge capacity of 774.4 mAh g^{-1} was achieved in the 2nd cycle at a current density of

0.1 A g^{-1}. Even for the 2nd cycle at a high current density of 0.5 A g^{-1}, the composite electrode displayed a specific capacity of 649.0 mAh g^{-1}, indicating a good rate capability of the BP/Ti_3C_2 composite electrode. This method of compositing with BP to improve capacity also provides a new direction for the further application of the MXene materials.

References

[1] Denis Y W, Prikhodchenko P V, Mason C W, et al. High-capacity antimony sulphide nanoparticle-decorated graphene composite as anode for sodium-ion batteries. ***Nature Commun.*** 2013, 4: 2922.

[2] Yan Y, Yin Y X, Guo Y G, et al. A Sandwich-Like Hierarchically porous carbon/graphene composite as a high-performance anode material for sodium-ion batteries. ***Adv. Energy Mater.***, 2014, 4(8).

[3] Kheirabadi N, Shafiekhani A. Graphene/Li-ion battery. ***J. Appl. Phys.***, 2012, 112(12): 124323.

[4] Gupta A, Sakthivel T, Seal S. Recent development in 2D materials beyond graphene. ***Prog. Mater. Sci.***, 2015, 73: 44-126.

[5] Ren C E, Zhao M Q, Makaryan T, et al. Porous two-dimensional transition metal carbide (MXene) flakes for high-performance Li-ion storage. ***ChemElectroChem***, 2016, 3(5): 689-693.

[6] Luo J, Tao X, Zhang J, et al. Sn4+ ion decorated highly conductive Ti_3C_2 MXene: promising lithium-ion anodes with enhanced volumetric capacity and cyclic performance. ***ACS Nano***, 2016, 10(2): 2491-2499.

[7] Zou G, Zhang Z, Guo J, et al. Synthesis of MXene/Ag composites for extraordinary long cycle lifetime lithium storage at high rates. ***ACS Appl. Mater. Interfaces***, 2016, 8(34): 22280-22286.

[8] Ahmed B, Anjum D H, Gogotsi Y, et al. Atomic layer deposition of SnO_2 on MXene for Li-ion battery anodes. ***Nano Energy***, 2017, 34: 249-256.

[9] Kajiyama S, Szabova L, Sodeyama K, et al. Sodium-ion intercalation mechanism in MXene nanosheets. ***ACS Nano***, 2016, 10(3): 3334-3341.

[10] Wu Y, Nie P, Jiang J, et al. MoS_2-nanosheet-decorated 2D titanium carbide (MXene) as high-performance anodes for sodium-ion batteries. ***ChemElectroChem***, 2017, 4(6): 1560-1565.

[11] Guo X, Xie X, Choi S, et al. Sb_2O_3/MXene ($Ti_3C_2T_x$) hybrid anode materials with enhanced performance for sodium-ion batteries. ***J. Mater. Chem. A***, 2017, 5(24): 12445-12452.

[12] Yuan H, Li Z. Interfacial properties of black phosphorus/transition metal carbide van der Waals heterostructures. ***Front. Phys.***, 2018, 13(3): 138103.

[13] Sun L Q, Li M J, Sun K, et al. Electrochemical activity of black phosphorus as an anode material for lithium-ion batteries. ***J. Phys. Chem. C***, 2012, 116(28): 14772-14779.

[14] Park C M, Sohn H J. Black phosphorus and its composite for lithium rechargeable batteries. ***Adv. Mater.***, 2007, 19(18): 2465-2468.

Chapter 6 Synthesis and application of a novel Mo, Nb-based double transition metal carbide for Na-ion battery

6.1 Introduction

In recent years, transition metal carbides or nitrides (MXene) have been widely studied in various energy storage systems, benefiting from its 2D graphene-like structure and high metallic conductivity. As far as we know, only several kinds of MXene have been investigated for the application on rechargeable batteries, including Ti_3C_2, Nb_2C and V_2C. [1-4] In addition, the development of double transition metal carbides are also attractive due to its flexible combination and application. As predicted by Barsoum's group, over 20 double transition metal carbides were suggested to exist by computational prediction. With a chemical formula of $M_2M'C_2$ or $M_2M'_2C_3$, the two transition metals can be any elements among Ti, V, Nb, Cr, Mo or Ta. [5] To date, only Mo, Ti-based and Mo, Sc-based ordered double transition metal carbides have already been synthesized, while Mo_2TiC_2 delivered a specific capacity of 175 mAh g^{-1} at a current rate of 1C in the lithium ion batteries. [5, 6] Therefore, developing new double transition metal carbides would make a great contribution to expanding the MXene family and their further applications. Since Mo_2C and Nb_2C both exhibited good electrochemical performance for the rechargeable batteries, we propose that Mo, Nb-based double transition metal carbides would also be a promising candidate for the sodium ion batteries.

In fact, MXene was derived from MAX phases, which have the general formula of $M_{n+1}AX_n$ (n=1, 2, or 3; A: IIIA or IVA group element). Thus, in order to prepare MXene materials, it is necessary to obtain the corresponding MAX phase materials first. On the other hand, most MAX materials were reported to be obtained by using Al as the A layer material and sintering at an extremely high temperature, while it was also be reported that using Tin as the A layer could synthesize MAX at a relatively low temperature. [7-9]

In this chapter, we attempted to synthesize a novel Mo, Nb-based MM'AX by using element raw materials via a low-temperature calcination method. The relationship between the reaction conditions (heating time, the molar ratio of raw materials) and the composition of the products

was investigated in detail. According to the investigated results, the optimized synthesis parameters were proposed and employed to prepare a sample with fewer impurities. Furthermore, the electrochemical performance of this Mo, Nb-based MM'AX product was investigated as an anode material for the sodium ion batteries.

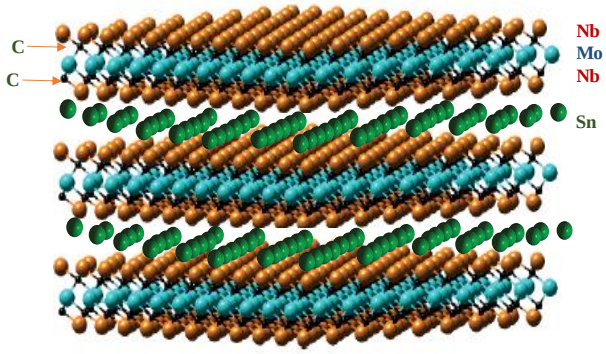

Scheme 1 Schematic of the new $MoNb_2SnC_2$ structure.

6.2 Experimental section

6.2.1 Preparation of Mo, Nb-based MM'AX with different reaction time

Mo, Nb-based MM'AX was synthesized by sintering the mixture of Mo, Nb, Sn and graphite powder under Ar protection. In a typical process, Mo, Nb, Sn and graphite powder were fully mixed by grind milling for 1 h with a molar ratio of 1: 2: 1.2: 2. Then the obtained mixture was transferred into an aluminum crucible and heated at 1000 ^{o}C with a heating rate of 5 ^{o}C/min in a tube furnace under Ar flowing with different time. After cooling to the room temperature, the obtained products were washed by 12 M HCl for 24 h under stirring to remove the residue raw materials and then washed with deionized water for several times until the PH was ~7. Finally, the products were dried in an oven at 60 ^{o}C for 12 h. In this section, we prepared Mo, Nb-based MM'AX with heating time of 6 h, 10 h, 18 h and 24 h, respectively.

6.2.2 Preparation of Mo, Nb-based MM'AX with different masses of Tin (metal A layer)

Mo, Nb, Sn and graphite powder were fully mixed by grind milling for 1 h with two different molar ratios of 1: 2: 1.2: 1, 1: 1: 2: 2 and 1: 2: 4: 2. The obtained mixtures were transferred into an aluminum crucible and heated at 1000 ^{o}C for 10 h with a heating rate of 5 ^{o}C/min in a tube

furnace under Ar flow. After cooling to the room temperature, the obtained products were washed by 12 M HCl for 24 h under stirring to remove the residue raw materials and then washed with deionized water for several times until the PH was ~7. The final products were obtained by drying in an oven at 60 ^{o}C for 12 h.

6.2.3 Preparation of Mo, Nb-based MM'AX with different molar ratios of Mo, Nb and graphite raw materials

Mo, Nb, Sn and graphite powder were fully mixed by grind milling for 1 h with different molar ratios of 1: 1: 1.2: 1, 2: 1: 1.2: 2 and 1: 2: 1.2: 2. The obtained mixtures were transferred into an aluminum crucible and heated at 1000 ^{o}C for 10 h with a heating rate of 5 ^{o}C/min in a tube furnace under Ar flow. After cooling to temperature, the obtained products were washed by 12 M HCl for 24 h under stirring to remove the residue raw materials and then washed with deionized water for several times until the PH was ~7. Finally, the products were dried in an oven at 60 ^{o}C for 12 h.

6.2.4 Characterization and electrochemical measurements

The testing conditions for the physical characterization were shown in Chapter 2.

The obtained products, acetylene black and PVDF were mixed with a mass ratio of 7:2:1. By using NMP as the solvent, the mixed slurry was coated onto the Cu foil disk and dried at 110 ^{o}C for 12 h. The mass loading on each disc was about 2 mg cm^{-2}. The obtained electrode was employed as the negative electrode. The half-cells were assembled in a glove box using sodium metal as the counter electrode and 1M $NaClO_4$ in the PC and EC mixed solvent as the electrolyte.

6.3 Results and discussion

6.3.1 XRD and SEM analysis of the products with different heating time

Figure 6-1 shows the XRD patterns of the as-prepared samples with different heating time. Similar diffraction peaks were observed from the four XRD patterns, indicating that reaction time was not a key factor for the composition of the as-prepared products. However, the sample with 10 h heating time displayed sharper diffraction peaks than the other three samples. Therefore, we further analyzed the XRD pattern of the product with 10 h heating time.

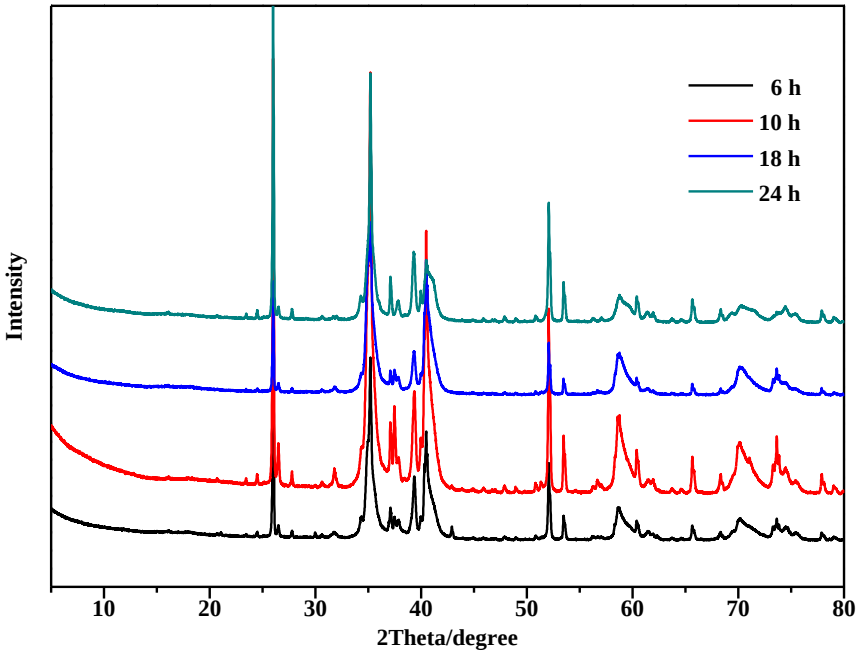

Figure 6-1 XRD patterns of as-prepared samples with different heating time.

Since there was no report about the Mo, Nb-based MM'AX, we compute a simulated XRD pattern of the $MoNb_2SnC_2$ by theoretical calculations and matched the simulated pattern with the as-prepared sample with 10 h heating time. As shown in Figure 6-2, most diffraction peaks of the sample match with the simulated XRD pattern, indicating that the $MoNb_2SnC_2$ was successfully obtained. However, the strongest characteristic peaks corresponded to the peaks of Nb_4C_3 and Nb_6C_5, illustrating the existence of impurities. Moreover, these strong peaks of impurities might also be the reason why the layered characteristic peak before 10^o was not found.

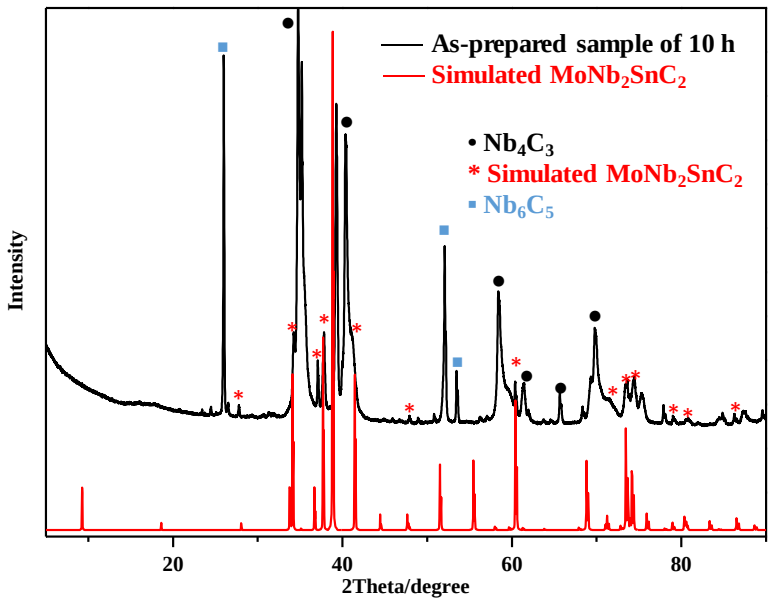

Figure 6-2 XRD patterns of the sample obtained by heating for 10 h and the simulated $MoNb_2SnC_2$ by calculation.

The morphology of these four samples was observed by the SEM. Figure 6-3 displays the SEM images of the sample heated for 6 h. It could be found that the sample consists of agglomerated particles, indicating the reaction time was not enough to form a layer-like structure. When the heating time was prolonged to 10 h, the stacked layer structure could be clearly observed from the SEM images in Figure 6-4. The thickness for each layer was about 10-20 nm. When further prolonging the heating time to 18 h, although the stacked layer structure could still be found, the surface of the layer structure was surrounded by small particles, which might be the impurities. After heating for 24 h, the layer structure became more difficult to observe, indicating that the impurities might continue to grow or gather on the surface of the layer structure. Therefore, 10 h was supposed to be the appropriate heating time for the preparation of the layered $MoNb_2SnC_2$.

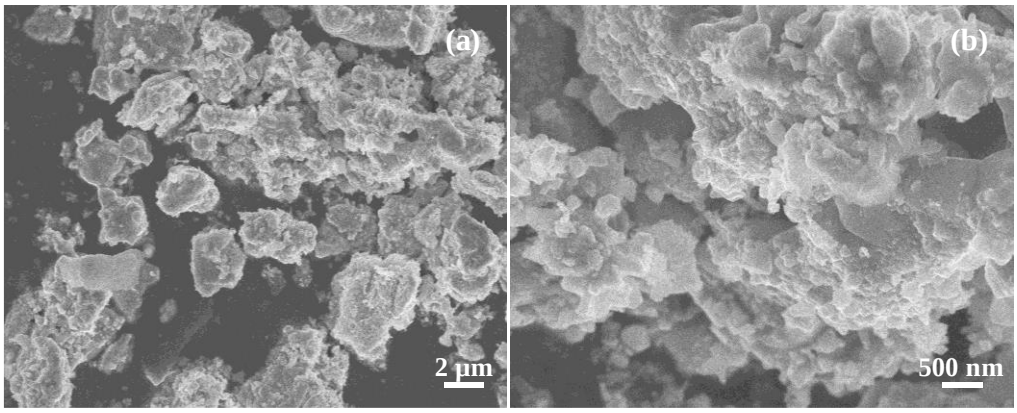

Figure 6-3 SEM images of the sample obtained by heating for 6 h.

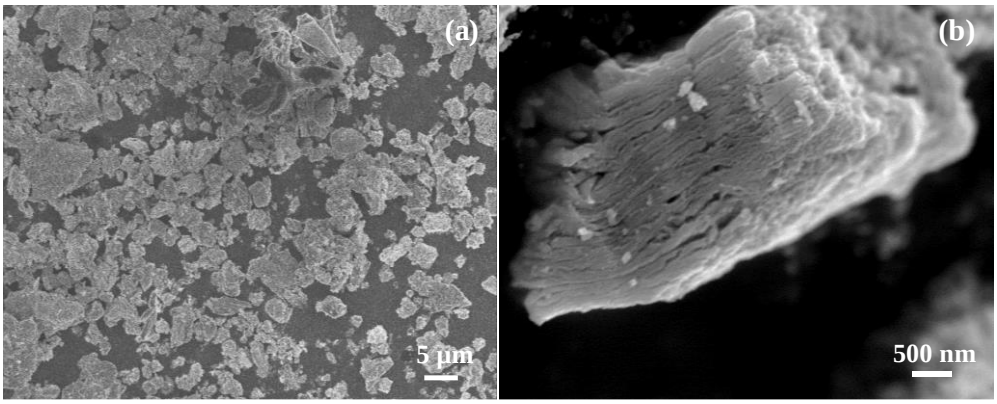

Figure 6-4 SEM images of the sample obtained by heating for 10 h.

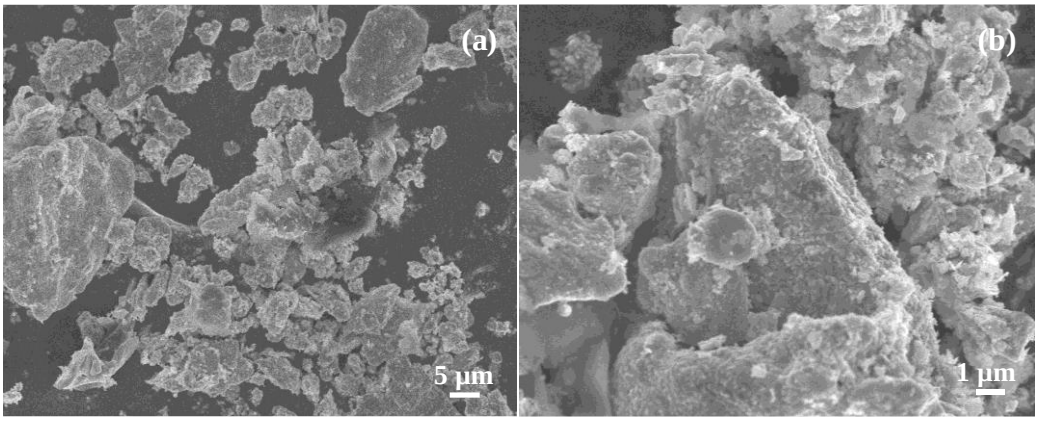

Figure 6-5 SEM images of the sample obtained by heating for 18 h.

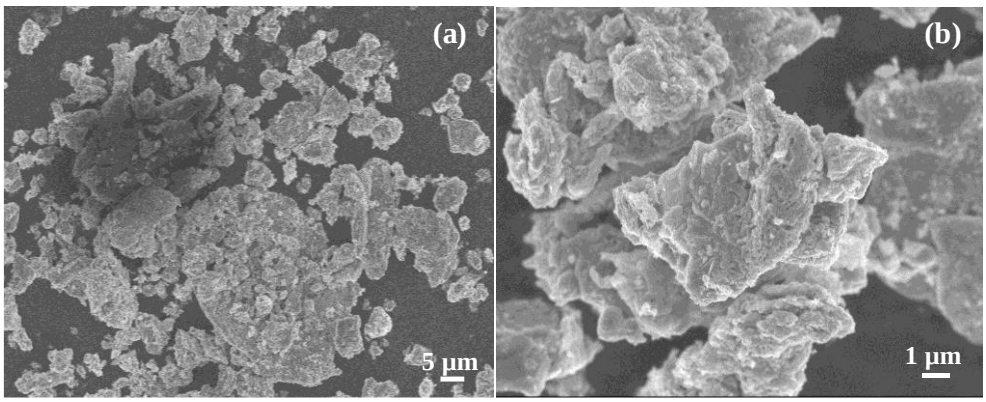

Figure 6-6 SEM images of the sample obtained by heating for 24 h.

6.3.2 XRD and SEM analysis of the products with different molar ratios of Tin raw materials

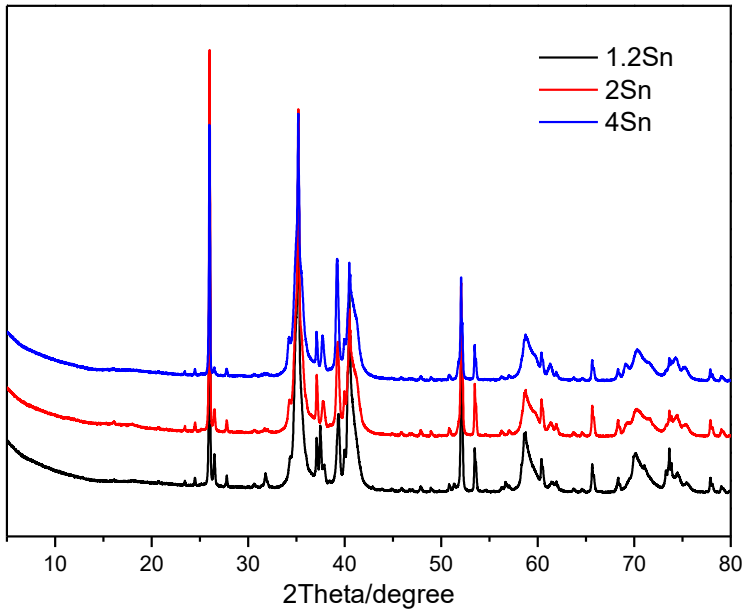

Figure 6-7 XRD patterns of samples with different mass of Tin (metal A layer).

The investigations of the heating time proved that the most appropriate reaction time was 10 h. On this basis, we investigated the influence of Tin on the composition of as-prepared products.

When the Tin mass was increased to 2 times and 4 times of the original amount, nearly no change was observed from the XRD patterns, indicating that increasing Tin amount would not increase the content of the MAX phase.

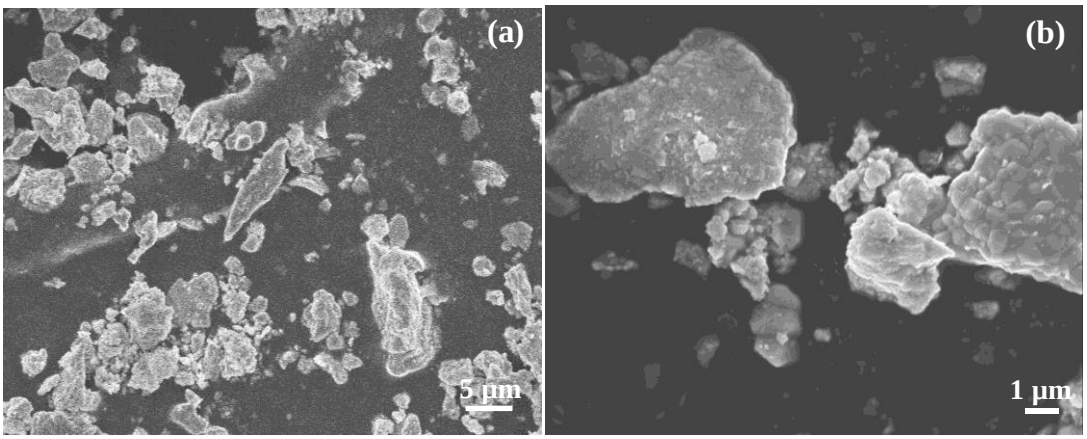

Figure 6-8 SEM images of the sample obtained by 2Sn raw materials.

The SEM images of the sample obtained by 2 times Sn raw materials were shown in Figure 6-8. When the molar ratio of Tin was increased to 2 times, some large bulk structure made of small particles could be observed. These gathered particles might be directly grown on the surface of the stacked layer structure. When further increasing the Tin mass to 4 times, the impurities on the surface of the layer structure became more and larger, as displayed in Figure 6-9. Therefore, the increasing mass of Tin might promote the growth of the impurities, and a molar ratio of 1.2 times was the most appropriate ratio for the preparation.

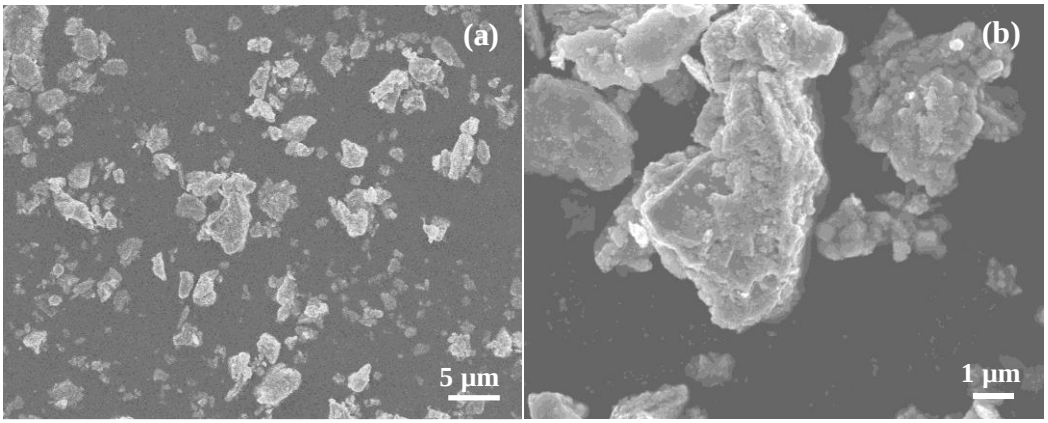

Figure 6-9 SEM images of the sample obtained by 4Sn raw materials.

6.3.3 XRD and SEM analysis of the products with different molar ratios of Mo, Nb and graphite raw materials

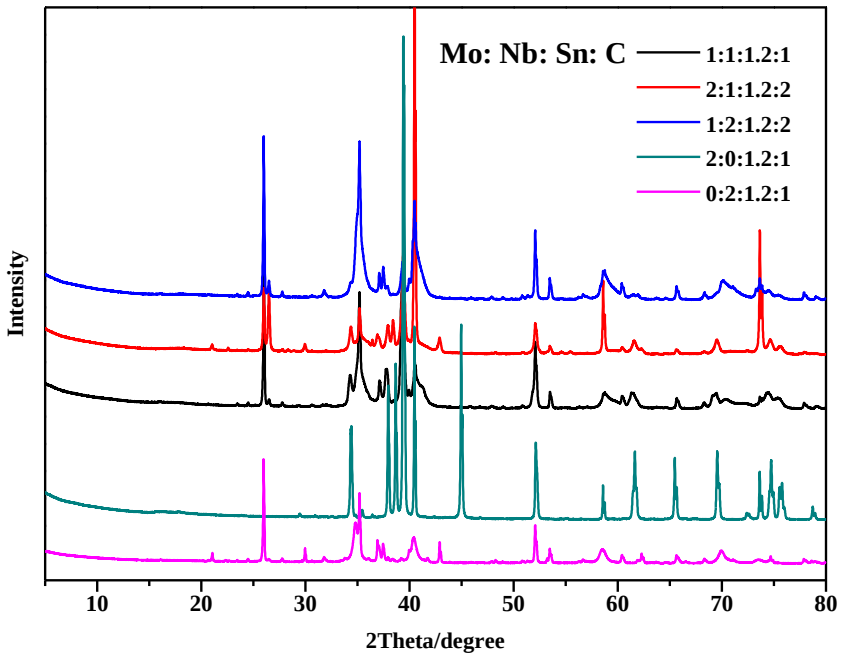

Figure 6-10 XRD patterns of samples with different molar ratios of Mo, Nb and graphite raw materials.

On the basis of the confirmed reaction time and Tin mass, we investigated the influence of the molar ratio of Mo, Nb and graphite raw materials on the MAX phase. The XRD patterns of the samples with different molar ratios of Mo, Nb and graphite raw materials were shown in Figure 6-10. As a comparison, the samples without Nb or Mo raw materials were also prepared. Under the same conditions, the XRD pattern for the sample without Mo was consistent with the reported XRD patterns of Nb_2SnC. However, the sample without Nb turned out to be Mo_2C, while the Sn could not react with Mo and the graphite. When the molar ratio of Mo, Nb and graphite was 1: 1: 1, the sample showed similar XRD pattern with Nb_2SnC while some peaks of Mo_2C could also be found. The strongest peaks belong to the peaks of the Nb_2SnC, illustrating Nb reacted first with Tin and graphite with the molar ratio of 1: 1: 1. When the molar ratio of Mo, Nb and graphite was 2: 1: 2, most diffraction peaks were indexed to the Mo_2C, while some peaks of Mo_2C could also be found. In addition, the strongest characteristic peaks belong to the peaks

of the Mo_2C. However, compared with these two samples, the XRD pattern of the as-prepared sample with the molar ratio of 1: 2: 2 was a little different. Some broad diffraction peaks could be observed from the XRD pattern.

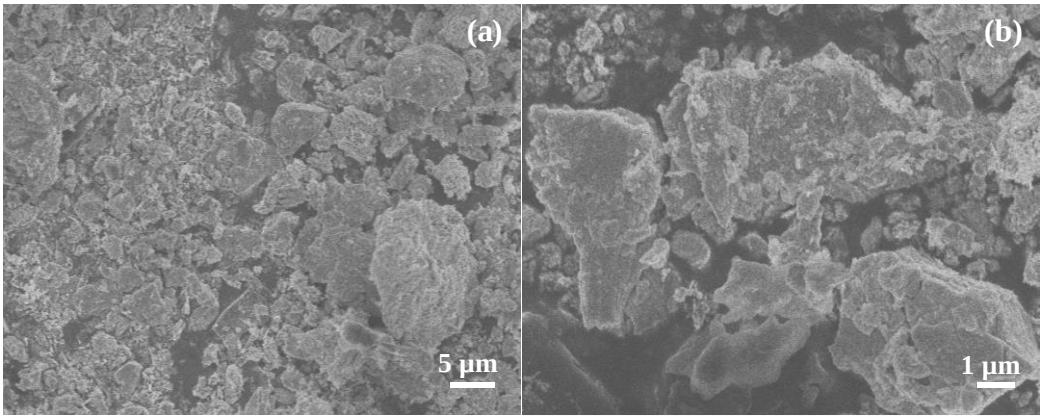

Figure 6-11 SEM images of the sample with molar ratio of 1: 1: 1.

Figure 6-11 shows the SEM images of the as-prepared product with the molar ratio of 1: 1: 1. Obviously, a lot of stacked layer structure could be found in this sample. However, according to the XRD results, the layer structure in this sample more likely to belongs to the Nb_2SnC, which also possesses layer structure.

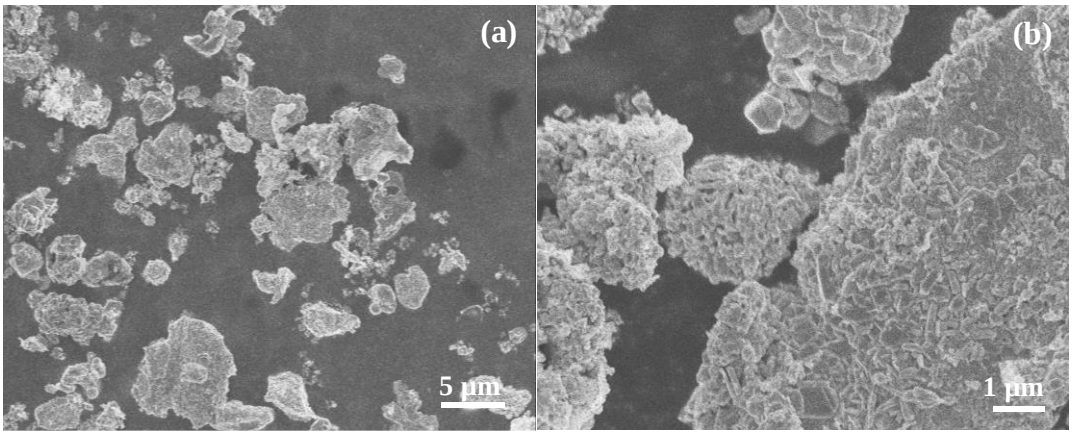

Figure 6-12 SEM images of the sample with a molar ratio of 2: 1: 2.

The SEM images of the as-prepared product with a raw material molar ratio of 2: 1: 2 was displayed in Figure 6-12. Completely different from the other two samples, no layer structure could be observed from the SEM images. Thus, we proposed that overdose Mo raw materials might inhibit the formation of the layer structure morphology.

According to the above investigations of the reaction conditions, it was concluded that heating for 10 h with a molar ratio of 1: 2: 1.2: 2 for the Mo, Nb, Sn and graphite raw materials was the most appropriate reaction conditions to prepare a sample containing the most $MoNb_2SnC_2$ MAX phases, as depicted in Scheme 2.

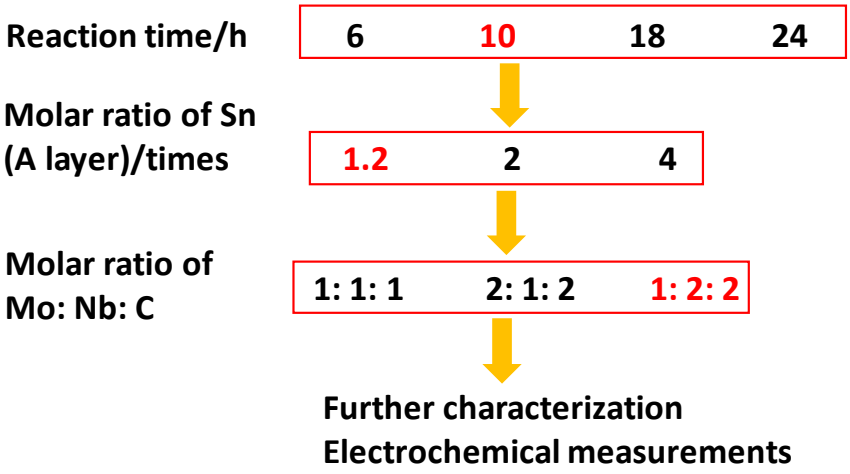

Scheme 2 Investigation process about the reaction condition.

Furthermore, the element mapping was also carried out to confirm the ingredient of the obtained sample. As displayed in Figure 6-13, the Mo and Nb elements exhibited nearly the same distribution, especially for the layer structure in the SEM images. Therefore, we confirmed the layered structure in the as-prepared sample belongs to the $MoNb_2SnC_2$ MAX.

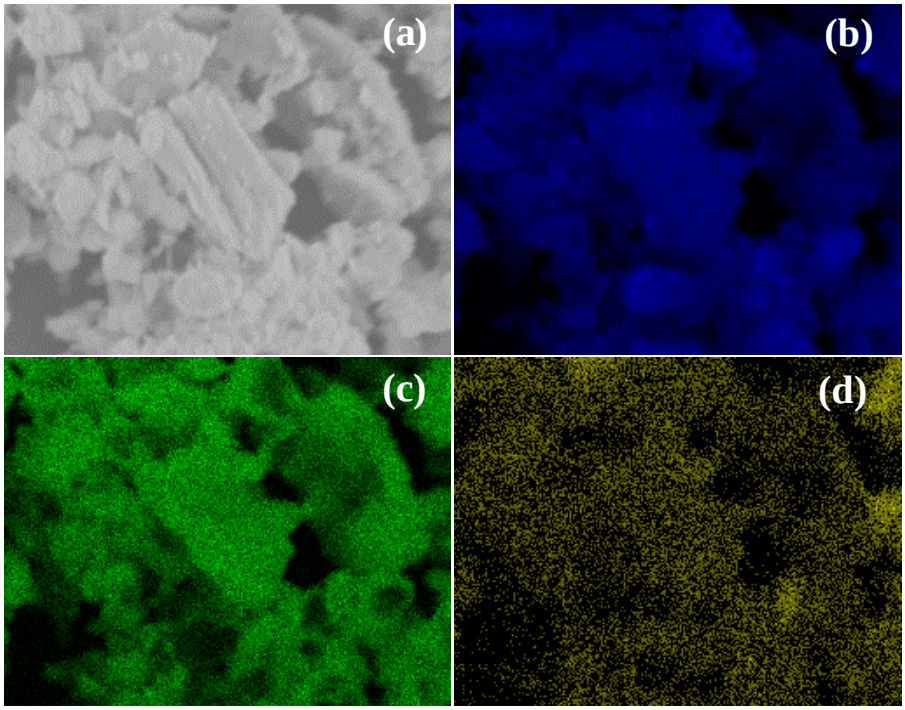

Figure 6-13 (a) SEM image of the as-prepared sample and corresponding element maps of Mo element (b), Nb element (c) and Tin element (d).

6.3.4 Electrochemical performance

The electrochemical performance of the as-prepared sample by optimized reaction conditions was initially investigated as the anode for the sodium ion batteries. Figure 6-14 shows the CV curves for the initial four cycles of the as-prepared sample with a voltage range from 0.01 to 3.0 V. The CV curve of the initial cycles was a little different from the subsequent cycles, which could be also attributed to the electrode activation process and some side reactions. A reduction peak at ~1.5 V could be observed from the initial cycle, while three oxidation peaks appeared at 1.63, 1.9 and 2.2 V, respectively. These peaks might be assigned to the insertion/desertion process of the sodium ions into the layer of the $MoNb_2SnC_2$. In addition, the CV curves from the 2^{nd} cycle exhibited nearly no change, illustrating a good reversibility of this electrode.

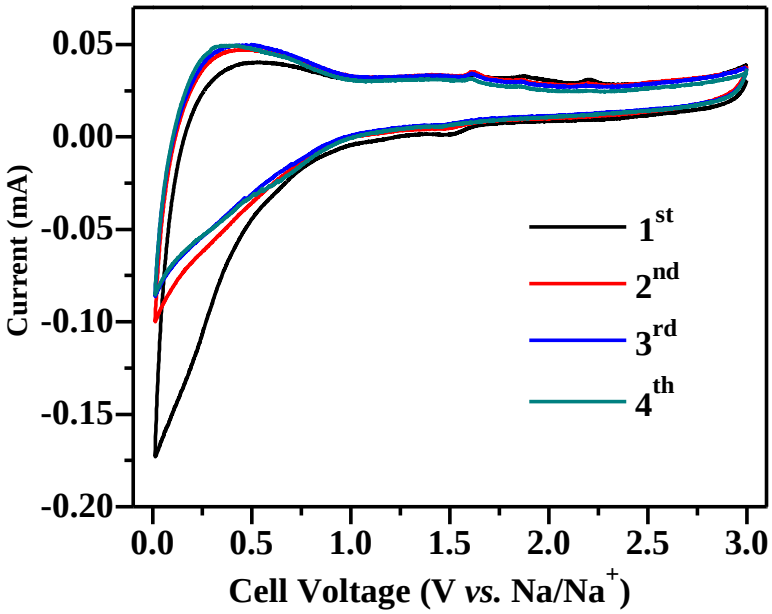

Figure 6-14 CV curves for the initial four cycles of the sample at a scan rate of 0.5 mV s^{-1}.

The charge-discharge profiles of the as-prepared electrode for the 1st, 2nd and 5th cycles at a current density of 0.1 A g^{-1} was shown in Figure 6-15a. Initial discharge and charge capacity of 242.7 and 118.1 mAh g^{-1} were achieved, indicating the occurrence of some side reactions in the initial cycling process. In the 2nd and 5th cycles, the electrode exhibited a discharge capacity of 152.6 and 102.8 mAh g^{-1}. In addition, the Columbic efficiency was obviously enhanced with the increasing cycling times, indicating the good reversibility of this material.

We also carried out the long cycling performance measurements for this material. Figure 6-15b shows the cycling performance at the current density of 0.1 A g^{-1}. For the initial 10 cycles, the specific capacity gradually faded during the cycling process. After cycling for 10 times, a discharge capacity of 62.7 mAh g^{-1} was remained. In the subsequent cycles, the capacity fade became much slower. After cycling for 120 times, the discharge capacity remained 59.8 mAh g^{-1}, indicating the good electrode stability.

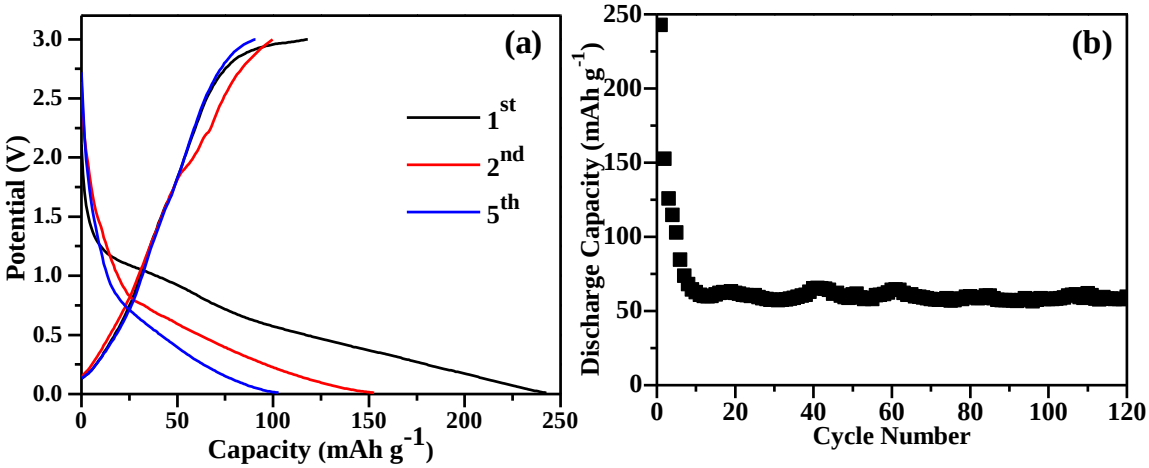

Figure 6-15 Charge-discharge profiles for the 1st, 2nd and 5th cycles (a) and long cycling performance of the sample at a current density of 0.1 A g^{-1}.

6.4 Conclusions

In summary, we synthesized a new 2D layer structure Mo, Nb-based carbides by the relatively low-temperature method. By investigating the reaction condition including heating time and a molar ration of the raw materials, the molar ratio of Mo, Nb raw materials was proved to be one of the key factors for preparing the Mo, Nb-based MAX phase materials. The optimized reaction condition was proposed and used to prepare the final product, which contained a high ratio of the $MoNb_2SnC_2$ MAX phase. Furthermore, the obtained product was applied as an anode for the sodium ion batteries and exhibited good reversibility as well as fine cycling stability. An initial specific capacity of 242.7 mAh g^{-1} was achieved at a current density of 0.1 A g^{-1}. In addition, a high capacity retention of 95.4% could be remained after 120 cycles as compared to the 10th cycle. Our future work would focus on the further optimization of the reaction conditions and investigation of the etching process to derive Mo, Nb-based MXene. This low-temperature method to prepare double transition metal carbides provides a new direction for developing other new MXene materials.

References

[1] Er D, Li J, Naguib M, et al. Ti_3C_2 MXene as a high capacity electrode material for metal (Li, Na, K, Ca) ion batteries. ***ACS Appl. Mater. Interfaces***, 2014, 6(14): 11173-11179.

[2] Naguib M, Halim J, Lu J, et al. New two-dimensional niobium and vanadium carbides as promising materials for Li-ion batteries. ***J. Am. Chem. Soc.***, 2013, 135(43): 15966-15969.

[3] Mashtalir O, Lukatskaya M R, Zhao M Q, et al. Amine-assisted delamination of Nb_2C MXene for Li-ion energy storage devices. ***Adv. Mater.***, 2015, 27(23): 3501-3506.

[4] Yu Y X. Prediction of mobility, enhanced storage capacity, and volume change during sodiation on interlayer-expanded functionalized Ti_3C_2 MXene anode materials for sodium-ion batteries. ***J. Phys. Chem. C***, 2016, 120(10): 5288-5296.

[5] Anasori B, Xie Y, Beidaghi M, et al. Two-dimensional, ordered, double transition metals carbides (MXenes). ***ACS Nano***, 2015, 9(10): 9507-9516.

[6] Meshkian R, Tao Q, Dahlqvist M, et al. Theoretical stability and materials synthesis of a chemically ordered MAX phase, Mo_2ScAlC_2, and its two-dimensional derivate Mo_2ScC_2 MXene. ***Acta Mater.***, 2017, 125: 476-480.

[7] Lei J C, Zhang X, Zhou Z. Recent advances in MXene: preparation, properties, and applications. ***Front. Phys.***, 2015, 10(3): 276-286.

[8] Zhang X, Xu J, Wang H, et al. Ultrathin nanosheets of MAX phases with enhanced thermal and mechanical properties in polymeric compositions: $Ti_3Si_{0.75}Al_{0.25}C_2$. ***Angew. Chem. Int. Ed.***, 2013, 52(16): 4361-4365.

[9] Kanoun M, Goumri-Said S, Reshak A. Theoretical study of mechanical, electronic, chemical bonding and optical properties of Ti_2SnC, Zr_2SnC, Hf_2SnC and Nb_2SnC. ***Comp. Mater. Sci.***, 2009, 47(2): 91-500.

General conclusions and future prospects

This thesis focused on the development of nanostructured anode materials for high-performance sodium ion batteries. The four different kinds of nanostructured materials with high theoretical specific capacity and/or structural stability were prepared by different methods. The relationships between the reaction condition and the structure, morphology of obtained products were studied and analyzed. Furthermore, these four materials were used as anode materials for sodium ion batteries, and the relationship between the intrinsic characters of materials and the electrochemical properties were investigated, respectively.

1. In Chapter 3, the porous TiO_2 nanopills were derived from a Ti-based metal-organic framework (MIL-125) by a two-step method. When measured as anode material for the sodium ion batteries, the TiO_2 nanopills exhibited good specific capacity and excellent electrode stability. The high discharge capacity of 196.4 and 110 mAh g^{-1} were achieved for the 2^{nd} cycles at current densities of 0.1 and 0.5 A g^{-1}, respectively. Moreover, the specific capacity could be remained after cycling for 3000 times with a high capacity retention of 90%. The good electrochemical performance could be attributed to the porous structure which facilitated the diffusion of sodium ions and electrolyte, as well as the nanosized particles which shortened the transmission distance of ions.

2. In Chapter 4, the feather-like nanostructured MnO_2 was directly grown on the carbon paper via a simple hydrothermal method. The feather-like MnO_2 on carbon paper exhibited excellent electrochemical performance as anode material for sodium ion batteries. A discharge capacity of 760.8 mAh g^{-1} was delivered at the 2^{nd} cycle under a current density of 0.05 A g^{-1}. In addition, a discharge capacity of ~300 mAh g^{-1} could be maintained for more than 400 cycles at the current density of 0.05 A g^{-1}, indicating the good reversibility and stability. The feather-like nanostructure makes a great contribution to achieving a high performance in sodium ion batteries.

3. In chapter 5, the black phosphorus (BP) nanoparticles with high theoretical capacity were combine to the 2D Ti_3C_2 material to improve the capacity. By compositing the pretreated BP nanoparticles and exfoliated Ti_3C_2 nanoflakes, the BP/Ti_3C_2 composite materials were prepared and applied as anode materials for sodium ion batteries. An improved specific capacity of 774.4

mAh g^{-1} was obtained for the 2nd cycle under a current density of 0.1 A g^{-1}. After cycling for 60 times, a discharge capacity of 121.1 was still retained. Despite that the specific capacity was enhanced, the electrode stability of BP/Ti_3C_2 composite materials still needed to be improved in the future work.

4. In Chapter 6, a novel Mo, Nb-based double transition metal carbides with layer structure was synthesized by a relatively low-temperature calcination method. The optimal reaction condition was investigated and confirmed as heating for 10 h with a molar ratio of 1: 2: 1.2: 2 for Mo, Nb, Tin and graphite raw materials. The optimal product was measured as anode materials for sodium ion batteries, and good stability and an initial specific capacity of 242.7 mAh g^{-1}. The preparation of Mo, Nb-based double transition metal carbides provides a new direction for the development of other new MXene materials.

To date, sodium ion batteries are still at the stage of research and development. To prepare sodium ion batteries with both high specific capacity and stability is a commonly studied topic for the future application. The previous research and our work both indicated nanostructured materials and composites can effectively improve the capacity and reversibility of the electrode. Meanwhile, 2D layer nanostructured materials with good conductivity and controllable morphology have also been regarded as a potential candidate for sodium ion batteries. We believe that further investigations about the sodium ion storage mechanism of nanostructured materials are emerging as a new direction for developing electrode materials with high performance for practical sodium ion batteries.

Achievements

Publications

1. **Huan Li,** Zhiguo Zhang, Xiao Huang, Tongbin Lan, Mingdeng Wei, Tingli Ma, "Metal–organic framework derived hierarchical porous TiO_2 nanopills as a super stable anode for Na-ion batteries." *Journal of Energy Chemistry*, 2017, 26(4): 667-672.
2. **Huan Li,** Anmin Liu, Shuai Zhao, Zhanglin Guo, Nannan Wang, Tingli Ma, "In-situ growth of a feather-like MnO_2 nanostructure on carbon paper for high performance rechargeable sodium-ion batteries ." Under review.
3. **Huan Li**, Zhanglin Guo, Nannan Wang, Shuzi Hayase and Tingli Ma, "Synthesis of a novel Mo, Nb-based double transition metal carbide and its application for sodium ion battery." In preparation.
4. Nannan Wang, Yanqiang Li, Zhanglin Guo, **Huan Li,** Shuzi Hayase, Tingli Ma, "Minute quantities of hexagonal nanoplates PtFe alloy with facile operating conditions enhanced electrocatalytic activity and durability for oxygen reduction reaction." *Journal of Alloys and Compounds*, 2018, 752, 23-31.
5. Jingjing Wang, Tingting Xu, Xiao Huang, **Huan Li,** Tingli Ma, "Recent progress of silicon composites as anode materials for secondary batteries." *RSC Advances*, 2016, 6(90), 87778-87790.
6. Zhiguo Zhang, Xiao Huang, **Huan Li,** Yingyuan Zhao, Tingli Ma, "3-D honeycomb $NiCo_2S_4$ with high electrochemical performance used for supercapacitor electrodes." Applied Surface Science, 2017, 400, 238-244.
7. Zhiguo Zhang, Xiao Huang, **Huan Li,** Hongxia Wang, Tingli Ma, "All-solid-state flexible asymmetric supercapacitors with high energy and power densities based on NiCo2S4@MnS and active carbon." *Journal of Energy Chemistry*, 2017, 26(6), 1260-1266.
8. Xiao Huang, Zhiguo Zhang, **Huan Li,** Yingyuan Zhao, Tingli Ma, "Novel fabrication of Ni_3S_2/MnS composite as high performance supercapacitor electrode." *Journal of Alloys and Compounds*, 2017, 722, 662-668.

9. Xiao Huang, Zhiguo Zhang, **Huan Li,** Hongxia Wang, Tingli Ma, "In-situ growth of nanowire $WO_{2.72}$ on carbon cloth as a binder-free electrode for flexible asymmetric supercapacitors with high performance." *Journal of Energy Chemistry*, 2018.

Conferences

1. **Huan Li,** Zhiguo Zhang, Xiao Huang, Tingli Ma, "Metal–organic framework derived hierarchical porous TiO_2 nanopills as a super stable anode for Na-ion batteries", Japan-China Workshop on "Nanomaterials and their applications in new energy devices", Fukuoka, Japan, October, 2017.
2. **Huan Li,** Zhanglin Guo, Nannan Wang, Tingli Ma, "In-situ growth of feather-like MnO_2 on carbon paper for high performance sodium-ion battery", 5th International Conference on Nanomechanics and Nanocomposites (ICNN5), Fukuoka, Japan, Aug. 22-25, 2018.

Acknowledgments

Firstly, I would like to express my deepest gratitude to Professor Tingli Ma, my supervisor, for her instructive advice, constant encouragement and guidance. During my Ph.D. study, Professor Ma gives me countless advice to my research and life. Without her consistent and illuminating instruction, this thesis could not have reached its present form.

I am also greatly indebted to Prof. Shuzi Hayase and Prof. Shyam S. Pandey, who have instructed and helped me a lot in the past three years.

Meanwhile, I would like to thank all the members in Hayase, Pandey & Ma Lab. They gave me many suggestions and encouragement during my stay in Japan.

Last my thanks would go to my beloved family for their loving considerations and great confidence in me all through these years.